Quantitative 3D Structure Studies of Supported Catalysts at the Nanoscale

TECHNISCHE UNIVERSITÄT DARMSTADT

Dissertation approved by the department of
Materials and Earth Sciences
in fulfilment of the requirements for the degree of
Doctor-Engineer
(Dr.-Ing.)

by

Wu Wang
M.E. in Materials Processing Engineering, Shanghai University, China
Born on September 25, 1988 at Shaodong, Hunan, China

Referee: Prof. Dr.-Ing. Horst Hahn
Co-referee: Prof. Dr. Christian Kübel
Date of submission: 01.03.2019
Date of oral exam: 29.03.2019

Darmstadt 2019
D19

Erklärung zur Dissertation

Hiermit versichere ich, dass ich meine Dissertation selbständig und nur mit den angegebenen Quellen und Hilfsmitteln angefertigt habe. Die Arbeit wurde bisher keiner anderen Prüfungsbehörde vorgelegt und noch nicht veröffentlicht.

Darmstadt, 01.03.2019

Wu Wang

Acknowledgements

I would like to express my sincere gratitude to many people for their support and encouragement during my PhD research and my thesis would not have been possible without their help.

Firstly, I would like to thank my research supervisor Prof. Horst Hahn for offering me the opportunity to pursue the doctorate. I sincerely appreciate his generous support and encouragement during my research.

I would like to express my sincere gratitude and appreciation to my direct research supervisor Dr. Christian Kübel for his countless support, guidance, beneficial discussions and patient towards the completion of this work. With his support and encouragement, I had chances to attend national and international conferences to communicate with professional scientists in the world and thereby updated my knowledge in the field of electron microscopy and nanomaterials. I also express my sincere appreciation and thanks to my daily research supervisor Dr. Di Wang for his diligent, meticulous guidance and support in every stage of my research. The discussions with him have improved my understanding about the principle of electron microscopy and inspired me in the entire process of my PhD research.

I also express my sincere thanks to Dr. Alberto Villa for his enormous contributions in catalyst synthesis and catalytic testing as well as scientific discussions, which were greatly helpful for me to understand the processing of catalysis and the structure-property relationship of nanocatalysts. My thanks also extend to Prof. Jan-Dierk Grunwaldt, Florian Maurer and Arik Beck for their kind cooperation and scientific discussions. Moreover, I would like to thank Prof. Ulrich Tallarek and Artur Svidrytski for their contributions in diffusion simulation in my research work and valuable discussions.

I want to express my sincere thanks to Dr. Xiaoke Mu, Dr. Sabine Schlabach and Dr. Torsten Scherer for their valuable suggestions and advice for my research work. My thanks also extend to Krishna Kanth Neelisetty, Gorji Mohammad Saleh, Suya Liu, Shyam Chethala Neelakandhan, Dr. D. Vinga Szabo and all other electron microscopy & spectroscopy group (EMSG) members for their friendly support in my research and help in my daily life as well.

In addition, I greatly acknowledge the financial support of the China Scholarship Council (CSC) for my research in Germany.

Last but most sincerely, I am so grateful to my parents and my young brother and I would like to thank my girlfriend Li Tan who worked as a PhD student in Potsdam. The four-year research life with her was sunny, happiness and full of vitality.

Abstract

Heterogeneous catalysis, where a solid catalyst facilitates a gas- or liquid-phase reaction, plays an irreplaceable role in chemical and fuel production as well as environmental control. The catalytic performance (activity, selectivity and stability) depends strongly on the details of the structure of the active sites and the morphology of the support. Understanding the structure-property relationship in catalysts and exploiting it for the development of highly selective and efficient catalysts require detailed and high-resolution characterizations of their structure, both in 2D and in 3D. In this thesis, advanced electron microscopy techniques with a focus on electron tomography and image analysis are applied to gain a deeper understanding of the distribution of the active particles and the morphology of the support for different catalysts to correlate the structural aspects with differences in catalytic performance. In particular, electron tomography is not only used as a qualitative tool to visualize nanostructures, but also pushed to provide quantitative 3D structural information at the nanoscale.

As one aspect, looking into the role of the support material in catalysis, the morphology and diffusion properties of a disordered mesoporous carbon material have been quantified based on electron tomographic reconstructions. The quantitative analysis strongly depends on the fidelity of the reconstruction and the segmentation, which are affected by pore size variations, the missing wedge during tomography acquisition and the reconstruction approach. The pore structure is described in terms of geometric and topological parameters based on both SIRT and DART reconstructions. The effect of the tomography acquisition, reconstruction and segmentation approach on the pore structure description is evaluated quantitatively in order to estimate the reliability of the description. Pore variations introduced in the reconstruction and segmentation process are mainly present in a few voxel wide boundary region of the pores, slightly altering the size and connectivity of pore structure. However, the calculated diffusion properties are very sensitive to variations in the pore volume and necking between pores and are therefore noticeably influenced by the anisotropic effects of the missing wedge, which estimated in simulations.

In order to address the role of the local structure of the active centers on the catalytic reaction as a second aspect for catalytic performance, electron tomography is applied to uncover differences in the distribution of Pd nanoparticles supported on mesoporous carbon (CMK-3) prepared by three synthetic methods: incipient wetness impregnation, wet impregnation and sol immobilization methods. The resultant spatial distributions of the Pd nanoparticles in the three Pd/CMK-3 catalysts are significantly different from each other and correlate with the activity and selectivity in liquid phase furfural hydrogenation. Pd nanoparticles located inside pores promote the formation of 2-methyl furan, while the selectivity for furfuryl alcohol and tetrahydrofurfuryl alcohol is suppressed correspondingly. Moreover, recycling tests indicated that leaching depends on the synthesis process and plays an important role with respect to catalytic stability.

Finally, looking into metal oxides as a different type of support and especially the effect of crystallographic faceting on the catalytic performance, electron tomography in combination with

HRTEM and HAADF-STEM imaging continues the 3D characterization of supported catalyst. The exposed surfaces of well faceted ceria particles were accurately determined both in 2D and in 3D. The cube shaped CeO_2 nanoparticles exhibit {100} facets as main surfaces with truncated edges giving rise to some {110} facets. In contrast, the rod shaped CeO_2 nanoparticles mainly exhibit two types of exposed surfaces corresponding to the {111} and {100} planes. The analysis of CO oxidation by Pt nanoparticles deposited on the cube and rod shaped CeO_2 particles revealed a correlation between the oxidation activity at low temperatures and the exposed surfaces of the CeO_2 nanoparticles, which is in agreement with theoretical predictions that oxygen vacancy generation on the oxide surfaces is the rate determining step in the catalytic reaction.

Contents

List of Figures

List of Tables

List of abbreviations

2D	Two-dimensional
3D	Three-dimensional
AAS	Atomic absorption spectroscopy
ADF	Annular dark field
ART	Algebraic reconstruction technique
BET	Brunauer Emmett Teller
BF	Bright field
BF-TEM	Bright field TEM
CCD	Charged coupled device
CNF	Carbon nanofiber
CS	Compressed sensing
CS-ET	Compressive sensing-electron tomography
CTF	Contrast transfer function
DART	Discrete algebraic reconstruction technique
DF-TEM	Dark-field TEM
EDXS	Energy-dispersive X-ray spectroscopy
EELS	Electron energy-loss spectroscopy
EFTEM	Energy filtered TEM
EXAFS	Extended X-ray absorption fine structure
FEG	Field emission gun
FFT	Fast Fourier transform
FTIR	Fourier transform Infrared (spectroscopy)
HAADF	High-angle annular dark-field
HDO	Hydrodeoxygenation
HRTEM	High-resolution transmission electron microscopy
ICP	Inductively coupled plasma
MAE	Mean absolute error
NP	Nanoparticle
RWPT	Random-walk particle-tracking
SIRT	Simultaneous iterative reconstruction technique

SSIM	Structural similarity index measurement
STM	Scanning tunneling microscopy
STEM	Scanning transmission electron microscopy
TEM	Transmission electron microscopy
WBP	Weighted back-projection
XRD	X-ray diffraction
XPS	X-ray photoelectron spectroscopy

1. Introduction

1.1. The structural aspects affecting the performance of heterogeneous catalyst

Heterogeneous catalysis, where a solid catalyst facilitates a gas- or liquid-phase reaction, plays an irreplaceable role in chemical and fuel production as well as environmental control.[1–3] It is estimated that 80% of all industrial chemical processes rely on solid catalysts to achieve high productivity and selectivity.[4] The worldwide sales in heterogeneous catalysis are expected to reach $29.9 billion in 2019.[5] As one important example, Fischer-Tropsch synthesis is critical for the production of gasoline and diesel from coal and natural gas. The development of catalysts for Fischer-Tropsch synthesis has largely improved the yield of high molecular weight linear alkanes and diesel fuels production in last decades.[6,7] Catalysts are also essential for the reduction of air/water pollution and thereby contribute to reduce the emissions of harmful products to human health and the environment.[8–10] Moreover, upcoming fields such as sensors, the sustainable production of fuels/chemicals and energy conversion/storage rely on the use of heterogeneous catalysts.[11] Thereby, the heterogeneous catalysis has become the heart of the modern energy and chemical industries as well as the sustainable energy fields in the future, as illustrated in Figure 1.1.

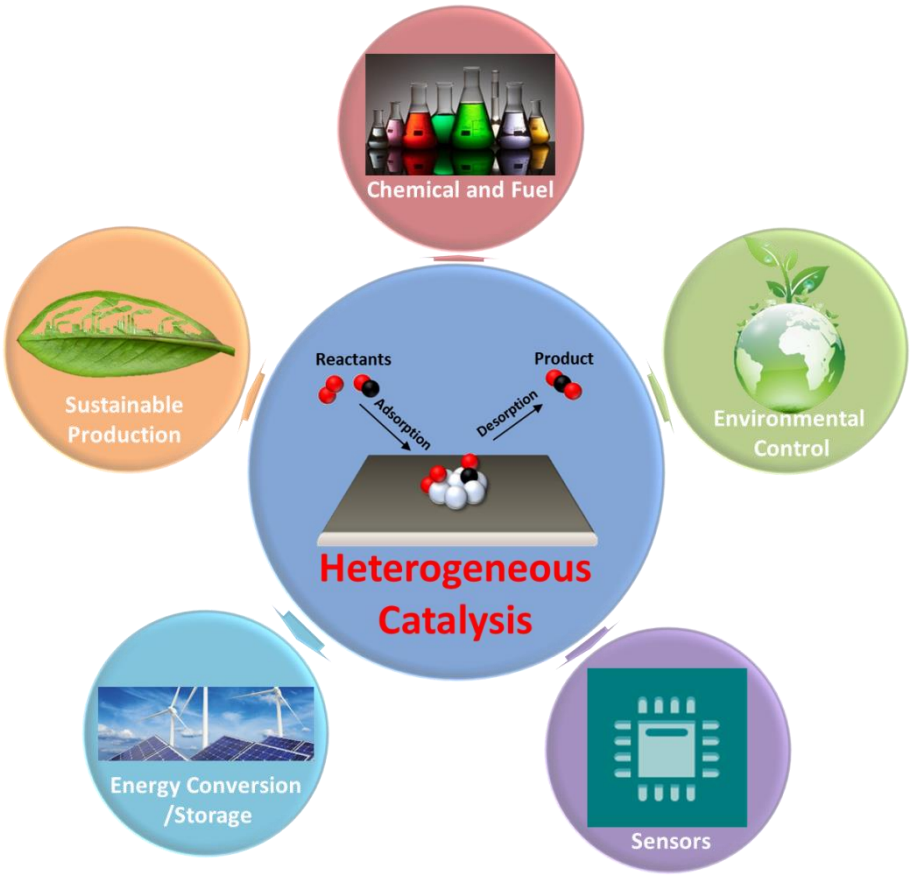

Figure 1.1: An illustration of heterogeneous catalysis in the heart of the modern energy and chemical industries.

The interaction and binding of reactants to a solid catalyst provides a pathway by which chemical reactions can occur, enabling the highly selective formation of desired products at rates that are

commercially viable.[12] In simple terms, reactant molecules are adsorbed on the catalyst surface, the electronic and/or structural changes due to the binding at the surfaces activates them to react to form a product, which then detaches from the catalyst, leaving the catalyst itself unaltered so that it is available for the next reaction cycle. Most heterogeneous catalysts consist of nanometer-sized particles dispersed on a high-surface-area support, such as zeolites, alumina, titania, silica or carbon. While for a long time a trial-and-error method was used to improve the catalytic performance, scientists nowadays are exploring to a molecular-level understanding of the relationships between nanoparticle properties and the catalytic performance and aim at a fundamental knowledge-based design for catalysts. This enables to design and optimize the catalysts to obtain the desired selectivity for reactions and to achieve high conversion as well as long lifetime during reactions. In order to achieve this fundamental knowledge-based design a better understanding of the structure-property correlations in catalysis is indispensable.

In previous research, it has been found that some factors have a particularly significant effect on the performance of heterogeneous catalysts. Particle size has been identified as a key factor for catalytic properties, not only because of the high surface area of the nanoparticles (NPs), but also because the surface structure and electronic properties can change greatly in nanometer range.[12] The changes of the catalytic activity and selectivity as a function of NP size are attributed to different contributions:[13–17] i) excess electronic charge ('extra electron');[18] ii) electronic structure of small metal clusters ('non-metallic behavior');[19] iii) the presence of a higher proportion of low coordinated atoms ('sticky side')[20] especially at edge/corner sites[21] and iv) NP-support interactions ('potent perimeter sites')[22], as illustrated in Figure 1.2. It is believed that it is not a sole, unique but rather, several of the above mentioned factors acting in parallel that influence the catalytic properties of supported NPs.

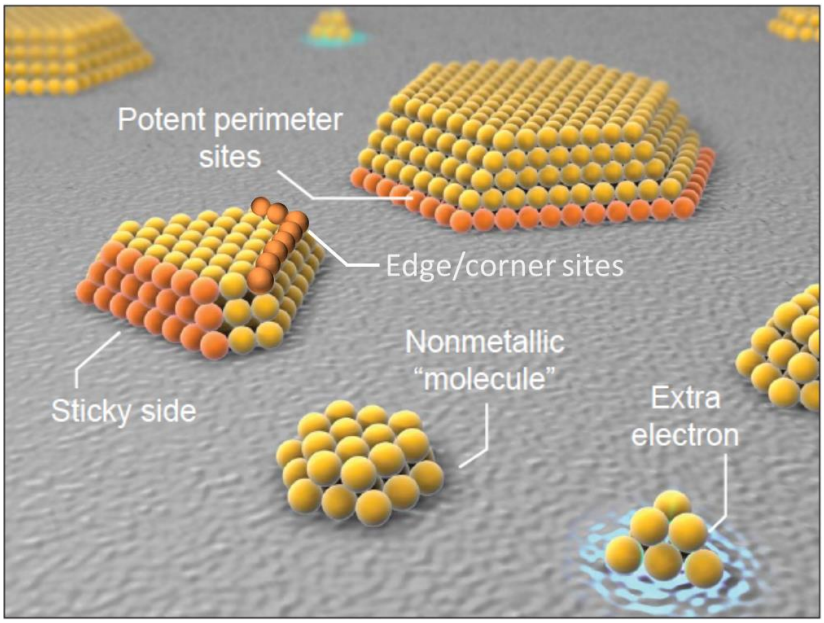

Figure 1.2: Possible active sites responsible for the enhanced reactivity of nanoscale gold.(Adapted from literature [17])

In addition to the size, other parameters including shape, surface geometry, chemical properties and composition of supported NPs affect the properties mentioned in the previous paragraph and thus significantly influence the performance in heterogeneous catalysis.[12,23–27] As an illustration of the critical role of the particle shape in catalysis, Wang et al. showed a shape effect of gold NPs supported on carbon nanofibers (CNFs) in the liquid-phase oxidation of glycerol.[26] Au NPs supported on ordered graphitic layers of CNFs preferably exhibited {111} facets, which resulted in an enhanced selectivity for the C3 products (glycolic and formic acids) compared to Au NPs supported on CNFs with a disordered carbon layer on the surface, which had a more random shape of the NPs and promoted the formation of glyceric acid. Another approach to tune the activity and selectivity in catalysis is the addition of a second element to form bimetallic catalysts by the geometric and electronic effects of the second element and the availability of bi-functional sites.[25,27] For example, Enache et al. reported that adding Au to Pd nanocrystals supported on TiO_2 greatly improved the selectivity for benzaldehyde in the oxidation of benzyl alcohol, where the added Au acts as an electronic promoter for Pd.[27]

The choice of support is another important factor in heterogeneous catalysis because the geometric constraints and the chemical properties of the support affect the state of the supported NPs, the adsorption of reactants, and the mass transfer processes.[28,29] For a long time, meso/macro porous materials have been considered as good catalyst supports because of their high specific surface area, tailorable morphology, chemical inertness, and good mechanical stability.[30,31] Prieto et al. showed that the stability of $CuZnO/SiO_2$ catalysts for methanol synthesis is significantly affected by the supporting porous structure.[32] The growth of the active CuZnO particles was confined during catalytic reaction in ordered cage-like silica (SBA-series) by the 3D pore structure and thus its stability notably improved compared to catalysts deposited in disordered SiO_2 sol-gel porous materials (SG-series) with a highly interconnected 3D pore structure (Figure 1.3).

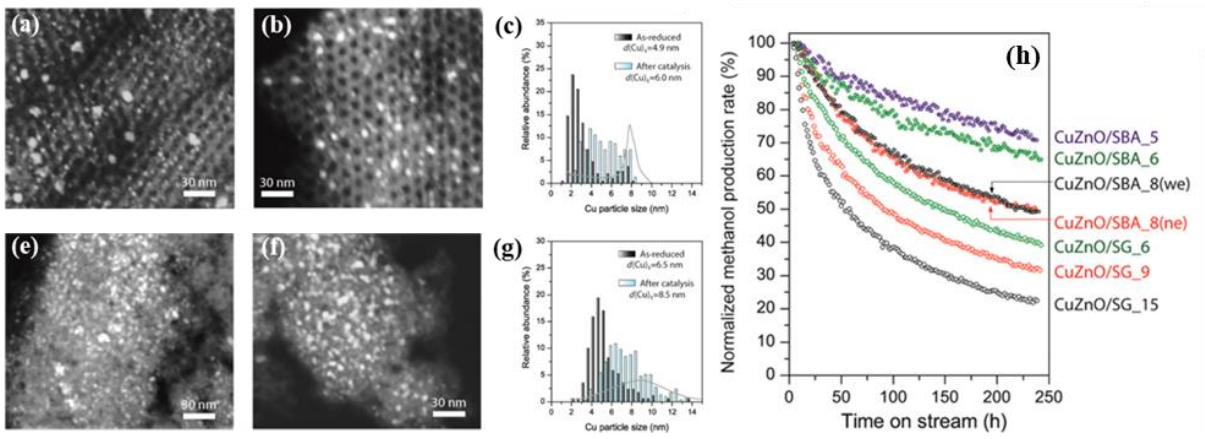

Figure 1.3: Morphology of CuZnO/SBA_8 and CuZnO/SG_9 before (a,e) and after (b,f) catalysis for 240 h and the derived Cu particle size distributions (c,g), The cage/pore size distribution of the support material has been included as a gray line in the corresponding Cu particle size histogram plots. (h) Evolution of the normalized methanol production rate with time on stream of a CuZnO/SBA and a CuZnO/SG catalysts (SBA_*x*(*y*) and SG_ *x*, where *x* denotes the mean cage diameter in nm and *y* is "ne" denoting narrow entrance or "we" denoting wide entrance for materials).[32]

In catalysis, the support not only acts as a framework to hold the active, highly dispersed particles on its large surface area, so that as many as active sites can be accessed by reactant molecules, but also the metal-support interaction modulates the chemical potential, which may positively or negatively influence the activity and stability of the active particles. Moreover, the distribution and location of supported NPs is an important factor for the catalytic performance. Villa et al. showed that the location of gold NPs has a strong effect on their catalytic activity and selectivity in liquid phase polyol oxidation.[33] By means of sol immobilization, Au NPs were deposited exclusively on the external surface of CNFs, whereas incipient wetness impregnation resulted in Au NPs both inside and outside of the CNFs. The catalyst with Au NPs trapped inside CNFs exhibited a significantly enhanced catalytic activity and modified selectivity in the polyol oxidation by promoting stronger oxidized products compared to the catalyst with Au NPs situated only on the external surface of CNFs. Similar phenomena have been reported for Pt–Ru, Pt or Pd NPs located on the outside or inside surfaces of carbon nanotubes.[34–36] Also Ni particles supported in a mesoporous MCM-41 support have demonstrated the importance of the location of the active particles on the selectivity for gasification of biomass[37]. When most of the particles were located inside the mesopores of MCM-41, the catalyst generated more gas, hydrogen and lower oil, compared to another catalyst where most of the particles were located on external surface of the support.

Because of the critical role of the support and NP structure, morphology and chemistry in catalysis, one key aspect in catalysis research is to characterize the nanostructure of supported catalyst to understand their structure-performance relationships and thus enable an improved design and development of catalyst materials. With the wide range of characterization techniques available nowadays, it is possible to characterize catalysts from the macro to the nano scale.[38,39] N_2 physisorption provides specific surface area and pore size distribution[40], while X-ray diffraction (XRD) is used for phase analysis of catalysts and to estimate the average NP size[41] and mesopore size[42]. Raman spectroscopy provides information on molecular bonding and the structure of active sites.[43] Extended X-ray absorption fine structure (EXAFS) and X-ray photoelectron spectroscopy (XPS) can provide highly sensitive surface compositional, chemical state and bonding information of catalyst.[44] Scanning tunneling microscopy (STM) can reveal fine details of the surface structure of supported catalysts from nanometer to atomic range and also provide the information regarding the electronic state of the supported NPs.[45,46] As an extremely versatile approach, advanced transmission electron microscopy is becoming increasing important to characterize supported catalyst far beyond just looking at direct structural information.

1.2. Transmission electron microscopy investigation of heterogeneous catalyst

Transmission electron microscopy (TEM) enables visualization and analysis of the local structure at the nano- and even atomic scale in heterogeneous catalysts (Figure 1.4),[23,47–50] directly imaging morphology, chemical/elemental distribution and atomic structure of catalysts as well as providing their crystallography and electronic structures. All of these information are needed to explore the

structure–property relationship and to understand the reaction mechanism of heterogeneous catalysts. Increasingly, all of the observation can also be done under dynamic conditions approaching the ones used for the catalytic reaction. This enables a much more direct analysis of the structure of the supported nanoparticles in the active state and in some cases even enabled direct imaging of the adsorbed species and the structural changes this introduces.

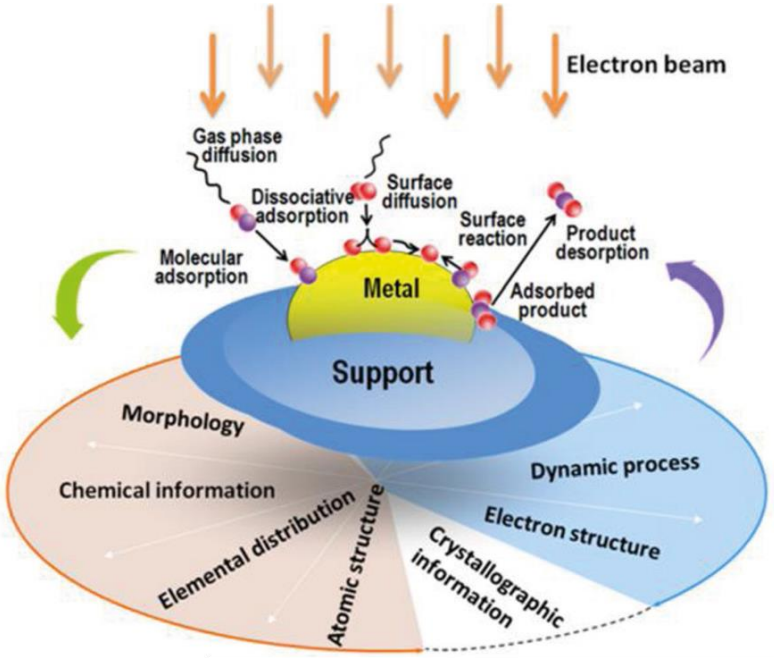

Figure 1.4: Electron microscopy revealing the microstructure of supported catalysts and its contribution to exploring the structure-function relationship.[50]

High-resolution transmission electron microscopy (HRTEM) and high angle annular dark field (HAADF) scanning transmission electron microscopy (STEM) can routinely reveal ultra-small particles, clusters, and even single atoms in a modern transmission electron microscope equipped with field emission gun (FEG) and spherical aberration corrector.[51–53] The determination of the particle size distribution of supported NPs is one of the most important applications of TEM for catalysis. With the particle size accurately determined for HRTEM or HADDF-STEM images, the dispersion of active sites (the percentage of atoms on the surface) and the specific surface area of active sites can be calculated, which is crucial towards a full understanding of the performance of supported catalysts. Moreover, HRTEM and HAADF-STEM can help to identify the active sites at the atomic level. As shown in Figure 1.5, the catalytic gold species for the CO oxidation in the iron oxide–supported catalyst samples have been identified by aberration-corrected HAADF-STEM.[54] This study indicated that individual Au atoms or planar monolayer gold clusters of 3-4 atoms are inactive species while the presence of bilayer clusters that are ~0.5 nm in diameter and contain only ~10 gold atoms significantly enhance the activity of CO oxidation. Moreover, the atomic structure of individual particle can be obtained by HRTEM and HAADF-STEM as well. For instance, high-resolution HAADF-STEM revealed the atomic structure of an Au/TiO_2 catalyst calcined at different temperatures.[55] As illustrated in Figure 1.6, Au NPs with cube-octahedral, singly twinned, and multiply twinned

morphologies were found in Au/TiO_2 catalyst dried at 120°C, whereas when calcined at high temperature (400°C) supported Au NPs show a tendency to form flatter and more extended interface structures. The evolution of the atomic structure of the Au NPs observed by STEM was correlated with the changes of the activity and selectivity for glycerol oxidation. To understand the metal-support interaction and its effect on catalytic activity and selectivity, HRTEM and HAADF-STEM have been widely used to explore the atomic configuration at the metal support interface.[56–60] As shown in Figure 1.7, the interfaces between ceria and Pd in Pd/CeO_2 catalysts with different Pd particle sizes were investigated by HRTEM and the resulting physical models were used to quantify the fraction of interfacial sites (corner and perimeter sites at the interface with support).[60] These findings contributed to establish the relationship between the interfaces of ceria-Pd and the activity for CO oxidation.

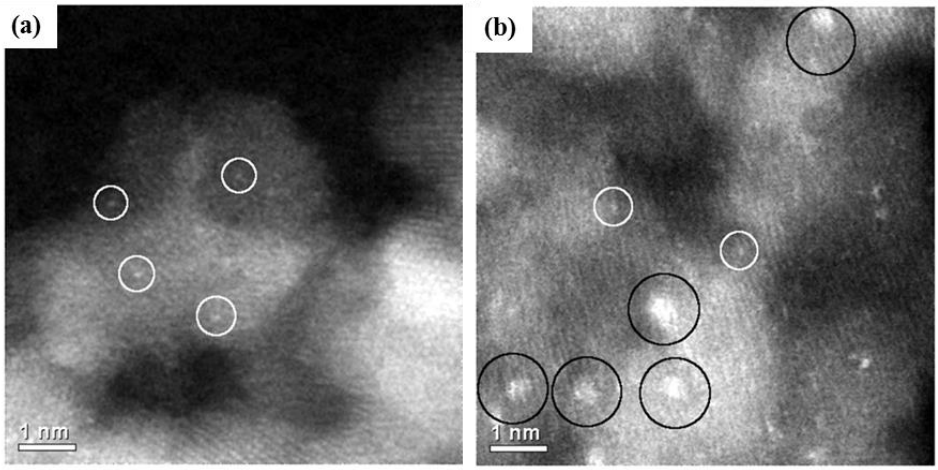

Figure 1.5: Aberration-corrected HAADF-STEM images of inactive (a) and active (b) Au/FeO_x catalysts. Individual Au atoms are indicated with white circles, whereas subnanometer Au clusters consisting of only a few atoms are marked by black circles.[54]

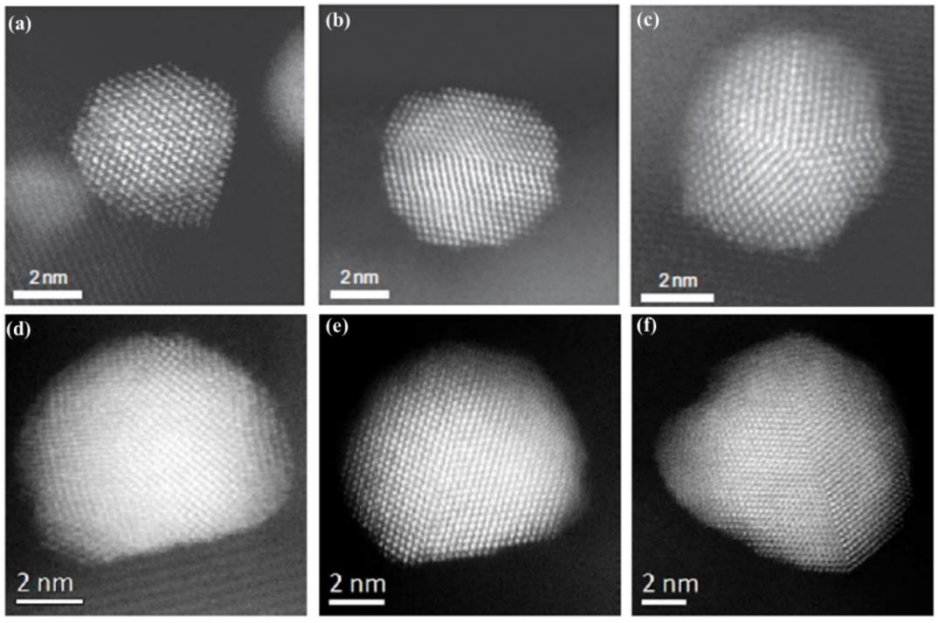

Figure 1.6: Representative HAADF-STEM images of the immobilized sol Au-PVA NPs on TiO_2 dried at 120°C (a-c) and calcined at 400°C (d-e).[55]

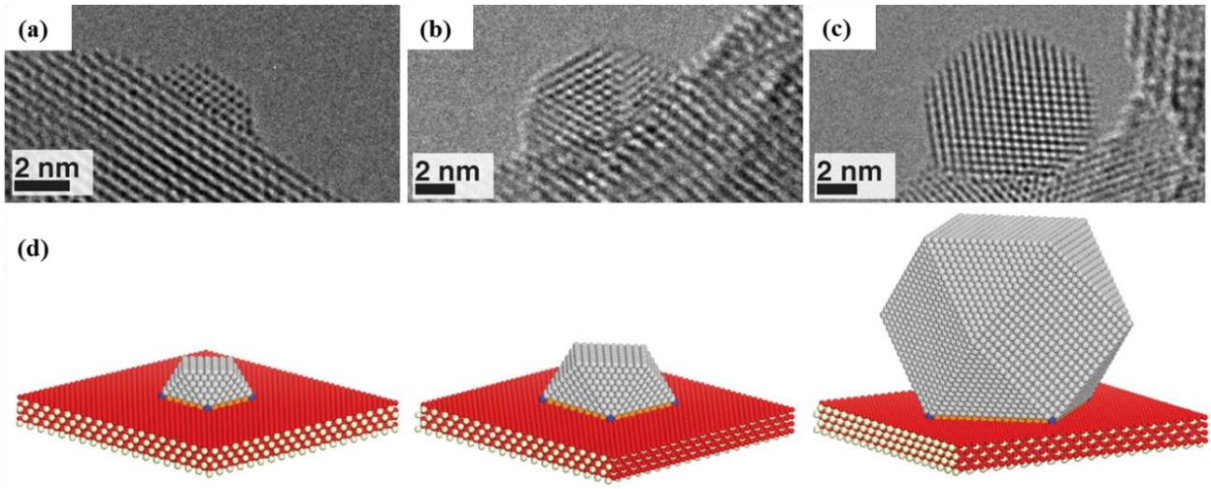

Figure 1.7: HRTEM images of Pd/CeO_2 catalysts with (a) small, (b) medium and (c) large Pd particle. (d) Physical models prepared to describe the corresponding particles. Blue, orange, and gray colors indicate corner, perimeter, and surface atoms, respectively; red and white are oxygen and cerium atoms of the ceria support.[60]

In addition to HRTEM/HRSTEM imaging, element-specific techniques including energy filtered TEM (EFTEM), electron energy-loss spectroscopy (EELS) and energy-dispersive X-ray spectroscopy (EDXS), are powerful tools available in electron microscopy for clarifying chemical composition and elemental distribution of supported multi-component NPs.[61–64] In bimetallic catalysts, identifying element distributions within supported NPs is crucial for exploring their unique catalytic properties. By atomic-scale STEM-EELS compositional analysis, Cui et al. have revealed an unexpected compositional segregation on the {111} facets of octahedral PtNi NPs (Figure 1.8), exhibiting a high activity for oxygen reduction.[65] Using STEM-EELS, compositional, morphological and surface structural evolution of the PtNi NPs were precisely monitored during lifecycle testing. This yielded a deep insight into the pristine structure, the activation and degradation of these PtNi catalysts for oxygen reduction.

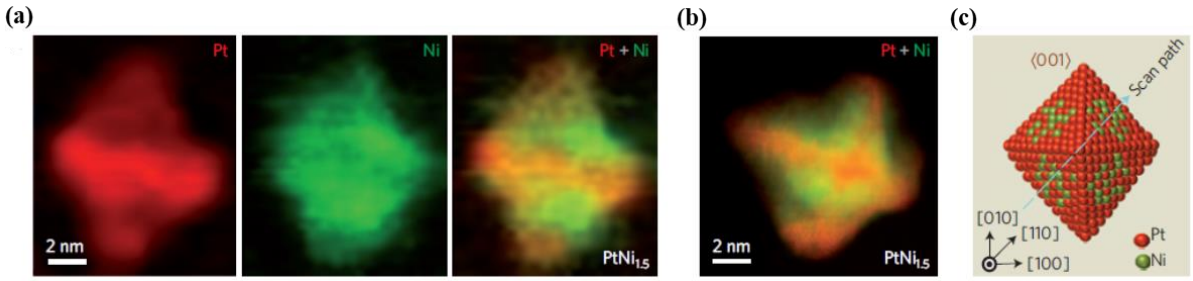

Figure 1.8: Atomic-scale composition profile analysis of $PtNi_{1.5}$ NP by STEM-EELS: (a) colored EELS mapping of $PtNi_{1.5}$ showing the segregated distribution of Pt (red) and Ni (green) taken along the [110] direction, (b) the composite image of Pt and Ni EELS mapping taken along the [100] zone axis, (c) the structure model showing Pt-rich frame and Ni-rich faces.[65]

1.3. Recent advances in the application of electron tomography to heterogeneous catalyst

While the (analytical) (S)TEM examples shown above have been successfully used to improve our understanding in catalysis, standard (S)TEM techniques only provide two-dimensional (2D) projections of the three-dimensional (3D) objects. However, 3D information to understand, e.g. the exact shape and distribution of supported NPs, cannot be accurately determined from single 2D images. Recent developments in electron tomography have overcome this limitation and extended the capabilities of TEM by providing full 3D reconstructions of nanomaterials.

Already in the 1960s, efforts to 'retrieve' 3D information from 2D TEM projections have been pioneered by De Rosier et al.,[14] Hart et al.[15] and Hoppe et al.[66] in structural biology. Starting in 2000, electron tomography has been applied to materials science and catalysis.[67–72] Nowadays, state-of-the-art electron tomography has become a versatile tool to study the complex morphology and chemical composition of nanostructures in 3D, moving from a simple 3D visualization towards quantitative measurements.[67,73,74] This provides new capabilities for understanding catalysis, in particular the 3D structure of supports, the 3D distribution of supported metal NPs and 3D chemical information for individual NPs.

1.3.1. 3D structure of support materials

The morphology of support materials, such as shape, exposed surfaces and porosity, are of great importance for catalysis to control the metal particle dispersion and to tune the catalytic properties. To understand the structure of supports, bulk characterization techniques like N_2/Ar physisorption or XRD are commonly used to provide an averaged evaluation of the support structure in terms of specific surface area and pore size.[40,41] However, for a detailed analysis, those techniques require models with assumptions on the pore shape and connectivity. They are not sufficient to fully describe the complex structure of porous supports. On the other hand, electron tomography in combination with image analysis have been demonstrated to provide 3D structural and morphological information at high spatial resolution without assuming any model for a wide range of catalyst supports,[75,76] like metal-oxides, silica and zeolites. For example, nanometer sized cerium oxide (CeO_2) particles are an interesting material for heterogeneous catalysis due to their redox properties, their ability to create oxygen vacancies on the surface. Therefore, their catalytic activity of CeO_2 strongly depends on their surface properties.[77] When CeO_2 is used as catalyst support for metal NPs, the metal-support interaction strongly depends on the exposed facets of CeO_2.[78] A detailed morphological and structural analysis of CeO_2 NPs with various well-defined morphologies: cubes, octahedra, and nanorods, has been performed using electron tomography in HAADF-STEM mode (Figure 1.9).[79] By combining 3D structural and HRTEM analysis, the types of exposed surfaces of cubic and octahedral-shaped CeO_2 NPs were determined. Moreover, in CeO_2 nanorods a porous network was directly evident. The 3D

characterizations greatly helped to establish a direct correlation between synthesis conditions and structures of these CeO_2 NPs and, in turn, to design the desired CeO_2-based catalyst.

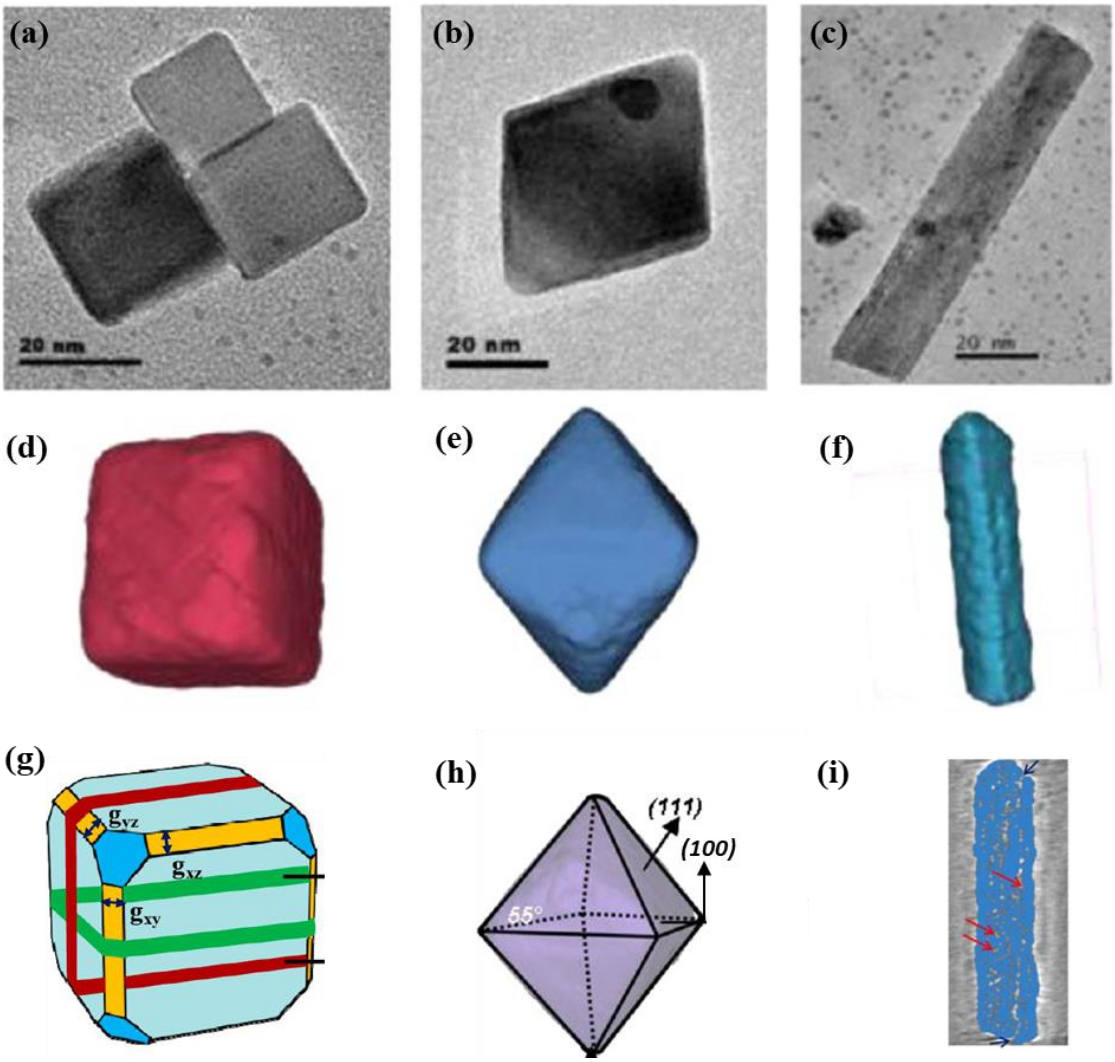

Figure 1.9: (a-c) Representative TEM images of CeO_2 NPs: cubes, octahedrons and nanorods; (d-f) 3D surface-rendering of the reconstructed CeO_2 NPs: cubes, octahedrons and nanorods; (g) schematic 3D representation of the CeO_2 cube NP: light blue facets represent main exposed surfaces, yellow facets indicate edges and blue facets are related to corners; (h) idealized 3D representation of an CeO_2 octahedral crystal: eight facets of {111} type are visible, with a (100) basal plane and the angle between the facets and the basal plane is 55°; (i) a longitudinal section extracted from the reconstruction of CeO_2 nanorod: the arrows indicate the presence of some pores within the nanorod.[79]

Porous materials with high surface area and diverse pore structures are one of the most important supports used in heterogeneous catalysis. The diffusion of the reactants and products during catalytic reactions, as a key factor for the activity, is related to the porosity of the support. To understand the complex 3D structure of various porous supports, an accurate 3D characterization of the pore architectures is needed. For the most part, the structure of porous supports including their crystallography, pore size, pore connectivity and tortuosity have been studied for well-ordered support materials. The 3D crystallography of the mesoporous silica MCM-48 has been directly determined by

means of electron tomography, which clearly revealed the 3D internal structure of this material.[80] For the ordered cage-like mesoporous FDU-12 silica, electron tomography has proven the intergrowth of cubic and hexagonal close-packed structures, and a direct visualization of these stacking faults has also been realized.[81] The SBA-15 silica with monodisperse, hexagonally arranged mesoporous channels is used widely,[82–84] including the development of catalysts and adsorbent materials.[25,85,86] Using electron tomography and image analysis, the local properties of the complex nanostructure in SBA-15 have been quantitatively accessed,[83] as shown in Figure 1.10. Qualitatively, the 2D hexagonal ordering of the silica has been shown (Figure 1.10a-c). Moreover, it was found that the radius and center of pores are variable along their axis and resulted in a corrugation of the surface (Figure 1.10d/e), which was quantitatively determined by image analysis. The calculated distribution of the pore diameter shown in Figure 1.10f fits well to the pore size measured by N_2 physisorption. Apart from the ordered channels of SBA-15, the interconnects between main pores, and the locally disordered merged pores have also been revealed in other electron tomography works.[68,84]

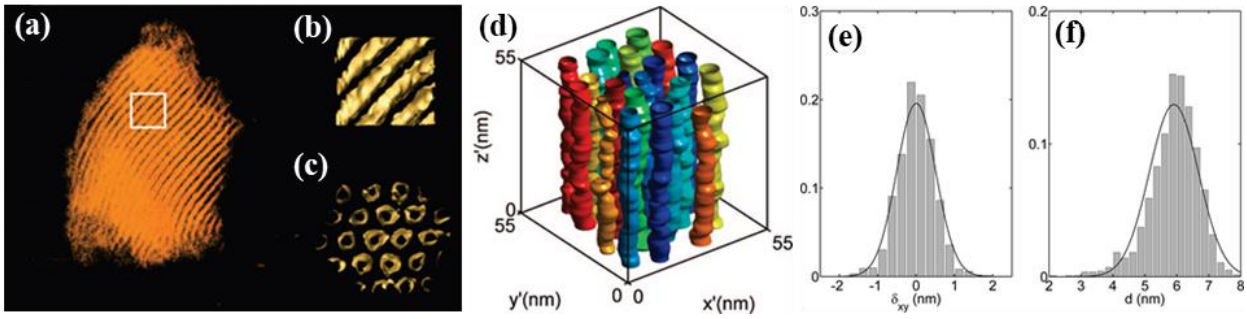

Figure 1.10: (a) The reconstructed intensity map of SBA-15 and (c,d) the extrapolated silica surface of the volume displayed in (a); (d) a description of the tomogram in terms of pores with varying centers and radii; Distributions of (e) the deviation between pore centers and points of the hexagonal lattice δ_{xy} and (f) the local pore diameter d of the pore volume in (d).[83]

Zeolites are another important type of ordered catalyst support because they exhibit two types of pores: microporous (pore diameter <2 nm) and mesopores (2-50 nm in diameter). The latter pore system commonly introduced by post-synthesis treatments such as steaming, acid or base leaching is crucial for the catalyst activity, selectivity and stability.[87–89] Krijn de Jong's group has made a lot of efforts to characterize the 3D structure of zeolites by electron tomography.[75,90,91] Quantitative information on the mesoporous network in a commercial zeolite Y sample have been obtained by electron tomography.[75] The fraction of mesopores connected to the external surface was measured. The constricted mesopores that cannot be detected by physisorption techniques were also visualized and quantified. The tortuosity of the pores, which is particularly important for the mass transfer efficiency of molecules within the mesopore network, was determined.

However, it should be noted that so far there is not much work reported on the investigation of the 3D structures of porous carbon materials, even though porous carbon has been considered a good catalyst support for a long time because of their high specific surface area, controllable chemical properties of the surface and diverse porous structure. Especially, the 3D structure of disordered porous

materials commonly used as supports has not been strongly investigated by electron tomography compared to ordered porous materials with well-defined pore structures.

1.3.2. 3D distribution and location of supported NPs

It has been demonstrated that the distribution and location of NPs supported on porous supports has a significant effect on catalytic performance,[12,92,93] usually due to factors such as confinement effects, transport properties, and interaction with the support surface.[94–96] For example, Serp et al. indicated that PtRu NPs inside carbon nanotubes are more active than the ones deposited on the external surface in cinnamaldehyde hydrogenation.[97] It was also found that the selectivity of Ni/MCM-41 catalysts during pyrolysis for catalytic gasification is strongly affected by the distribution of NPs.[37] The distribution and location of NPs on/in the support can be evaluated by electron tomography. For instance, using HAADF-STEM electron tomography, 3D structural features of a heterogeneous catalyst consisting of gold NPs supported on titanium dioxide have been revealed (Figure 1.11).[98] It was found that most of the Au NPs are located at the titania grain boundaries and vertices, with only few Au particles located on the flat facets. The 3D location of particles is assumed to be related to the stability of the NPs, which can contribute to design the catalyst with a longer durability. In another study, HAADF-STEM tomography provided morphological information on bimetallic Ru-Pt NPs supported on and within disordered mesoporous silica by exploring the location of catalyst particles as a function of the local surface curvature of the support (Figure 1.12).[99] It was shown that NPs situated in the interior of the support preferred to anchor on anticlastic (saddle-shaped) locations, whereas this shifted more towards concave (cuplike) regions for NPs situated on the exterior surfaces.

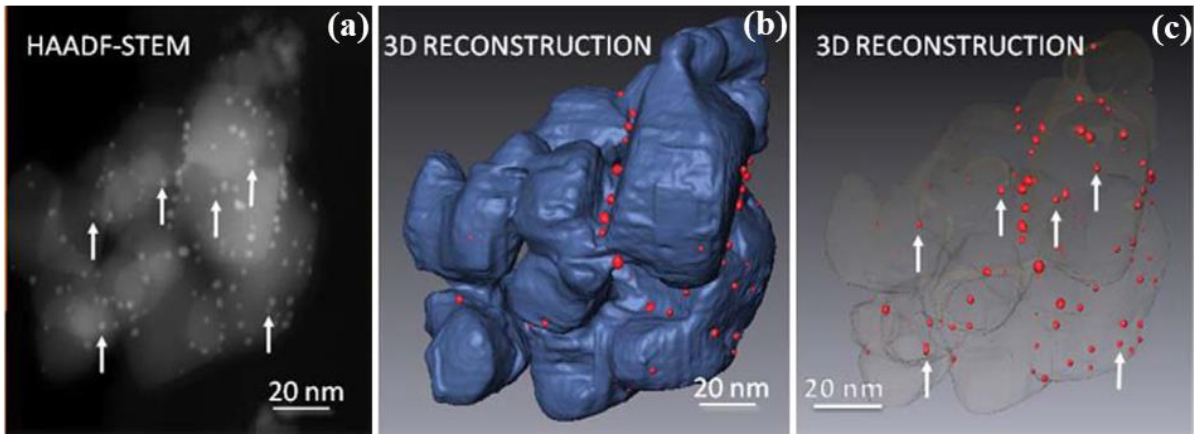

Figure 1.11: (a) 2D HAADF-STEM image from the tilt series acquired for the tomographic reconstruction; (b) Surface-rendered representation of the segmented reconstruction of the Au/TiO_2 catalyst. Note that most of the gold NPs are located near the grain boundaries of the titania support crystallites; (c) Partially transparent surface-rendered reconstruction of the Au/ TiO_2 catalyst: arrows indicated some NPs that lie behind the support crystallites, which not visualized in the center figure.[98]

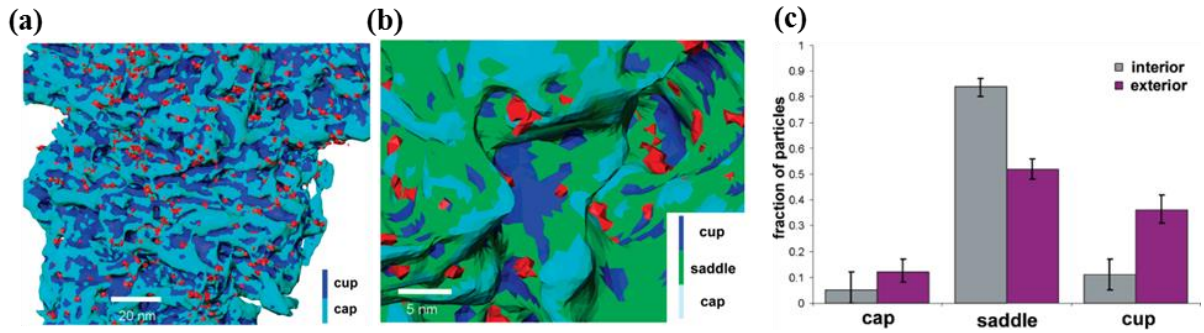

Figure 1.12: (a, b) Region of the exterior silica surface colored according to its local curvature and Ru-Pt NPs shown in red: the metal particles appear to be situated preferentially in positions with saddle to cuplike geometry; (c) The distribution of NP locations in the interior and exterior regions of the support, expressed as a fraction of the total number of particles in each region.[99]

Another important aspect is that the distribution and location of the active particles is closely related to the stability of the catalyst. Loss of active surface area by metal particle growth is a major cause of deactivation for supported catalysts.[100] Strategies to mitigate particle growth comprise alloying with a higher-melting point metal,[101] increasing the interaction with the support,[102] encapsulation of NPs[103,104] and the use of porous support.[30,31] Prieto et al. proposed a novel concept that the metal particle growth, i.e. catalyst stability, can be enhanced by controlling the 3D spatial distribution of supported metal NPs.[73] Electron tomography has become the most important techniques to provide quantitative information on the 3D distribution of NPs (Figure 1.13). By pore-specific manual segmentation, the distance to the nearest and second-nearest neighboring particles was calculated in CuZn/SBA-15 catalysts calcined under a flow of 2% NO/N_2 or a flow of N_2. It was found that the average distances between particles in catalyst calcined in N_2 flow is obviously larger than the one calcined in NO/N_2 flow, which was correlated with a better stability in methanol synthesis.

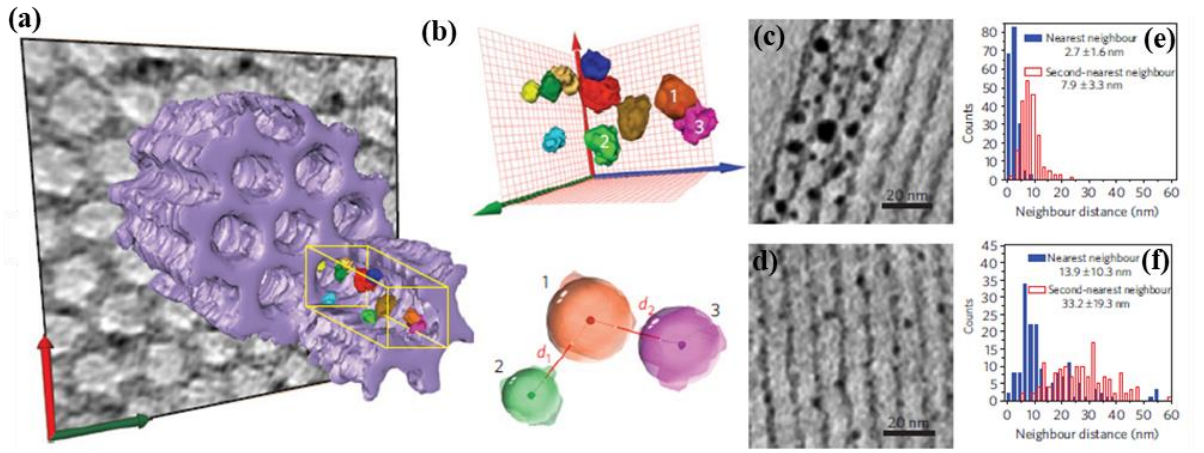

Figure 1.13: (a) 3D-rendered volume obtained by image segmentation showing the hexagonal arrangement of the catalyst mesopores as well as details of the individual Cu NPs; (b) schematic 3D view of the isolated Cu NPs extracted from the volume indicated with a yellow frame in (a) and the derivation of surface-to-surface interparticle distances; Slices through the reconstructed 3D volumes of CuZn/SBA-15 catalyst after NO/N_2 (c) and N_2 (d) calcination, and the corresponding surface-to-surface nearest-neighbor distance histograms (e,f).[73]

1.3.3. Element specific 3D imaging

Besides valuable 3D nanostructure information, direct chemical information with nanometer spatial resolution can be provided by EELS/EFTEM and EDXS in the (S)TEM. Combining EFTEM/EELS/EDXS with tomography has been proven to be a valuable method to obtain both structural and chemical information in 3D with nanometer resolution, which is of great help to fully understand the distribution of elements within complex catalyst structures and correlate it with the catalytic performance.[105–108] For example, tomography in EFTEM mode has been reported to precisely determine the 3D distribution of nitrogen in nitrogen-doped bamboo-type carbon nanotubes.[109] A detailed analysis of the elemental volumes of carbon and nitrogen indicated that the nitrogen is preferentially incorporated inside the transversal bended arches (triangular shape) inside the nanotube, whereas the round arches have relative low nitrogen incorporation. Moreover, this finding also indicated the relationship between nitrogen concentration and morphology along the tube axis: close to the round arches (with less N), the tube is roughly cylindrical, whereas near the transversal ones (with more N), its shape changes to a prism (Figure 1.14).

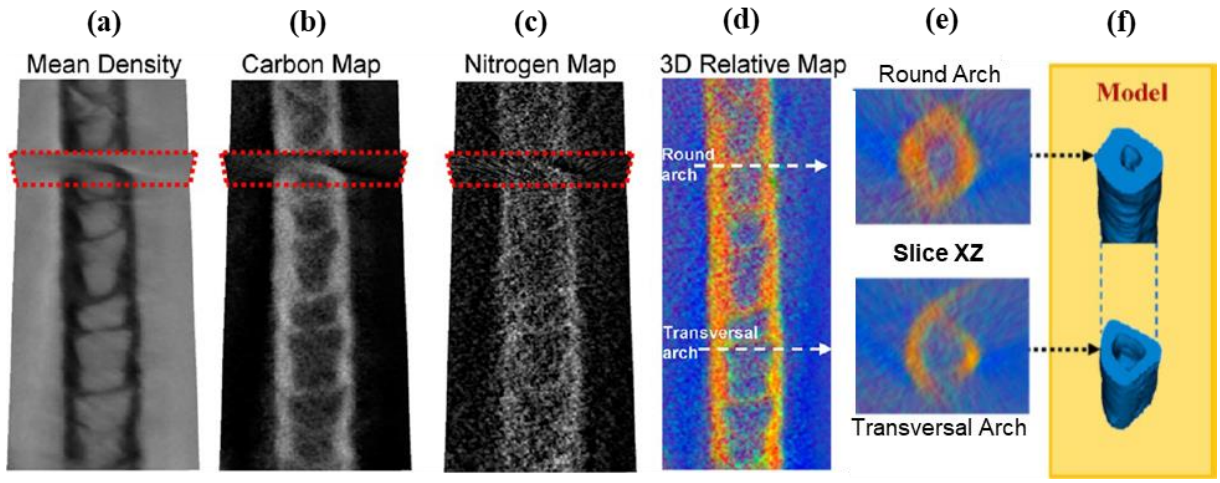

Figure 1.14: (a) Typical longitudinal slices extracted at the same depth and orientation from the EFTEM reconstruction, (b,c) the corresponding carbon and nitrogen 3D elemental maps, and (d) C-to-N 3D relative map (nitrogen in green and carbon in red); (e) cross-sections (XZ slices) of the two types of arches extracted at the positions indicated by the two arrows in (d), and (f) the corresponding 3D model of the analyzed carbon nanotube.[109]

1.4. Motivation and scope of thesis

Understanding the structure-property relationship in catalysts and exploiting it for the development of highly selective and efficient catalysts require detailed insights into their structure, both in 2D and in 3D. The aim of the works presented in this thesis is to gain a deeper understanding of the distribution of the active metal particles and the morphology of the support for different catalysts to correlate the structural aspects with differences in the catalytic performance. The approach employed in thesis mainly relies on advanced electron microscopy techniques with a focus on electron tomography

and image analysis. In particular, in the present work electron tomography is not only used as a qualitative tool to visualize nanostructures, but also pushed to provide quantitative 3D measurements. **Chapter 2** introduces the background and working principles of TEM and also addresses fundamentals and practical aspects of electron tomography, development of advanced reconstruction algorithms, segmentation and quantitative analysis as the fundamental methods used in my thesis. In order to understand the fidelity of the segmented 3D reconstruction and its effect on the morphology and measured/calculated properties of the support materials, **Chapter 3** evaluates the quantification of morphological parameters and diffusion properties of mesoporous carbons from 3D reconstructions by different approaches using both experimental data and realistic phantoms. To understand the effect of different NP deposition methods on their 3D distribution, and their role in the catalytic performance, **Chapter 4** applies electron tomography to uncover the metal dispersion and structural differences of the Pd/CMK-3 catalysts synthesized by incipient wetness impregnation, wet impregnation and sol immobilization methods. Based on the quantitative tomographic analysis, the 3D distribution of the Pd NPs on the mesoporous carbon CMK-3 was systematically investigated for the three catalysts and the observed structures were correlated with their activity and selectivity in liquid phase furfural hydrogenation. **Chapter 5** continues the 3D characterization on metal oxide supported catalyst to investigate the effect of crystallographic faceting on the catalytic performance. Combining HRTEM, HAADF-STEM imaging and electron tomography, the exposed surfaces of regularly shaped ceria (CeO_2) particles were accurately determined both in 2D and in 3D. A correlation between the CO oxidation activity at low temperatures and the exposed surfaces of the CeO_2 NPs was established to gain a more fundamental insight on the mechanism of CO oxidation.

2. Characterization techniques

Identifying the complex nanostructures of catalysts plays an important role for tuning their selectivity, activity and stability, which requires high-resolution structural characterization methods.[49,110] Among the characterization techniques employed for heterogeneous catalysis, TEM is particularly useful for its ultrahigh spatial resolution, which provides details ranging from morphology of the support to particle size & shape, dispersion, crystallographic information and elemental composition.[23,47–50] Moreover, recent developments in electron tomography have further extended the capabilities of TEM enabling 3D reconstructions of samples with nanometer resolution to obtain the full 3D structure of catalysts,[68,74] such as the exact shape and 3D distribution of NPs within or on a support.

To interpret the 2D/3D structures of catalysts observed by TEM and electron tomography, it is essential to understand the image/spectrum formation mechanisms in TEM as well as the acquisition and reconstruction procedures of electron tomography. Therefore, in this chapter a theoretical introduction to imaging/spectroscopy in TEM is provided. Moreover, the fundamentals, practical aspects and state-of-the-art methods in electron tomography are reviewed, along with limitations and challenges.

2.1. Introduction to transmission electron microscopy

The first transmission electron microscope was constructed in 1931 by Max Knoll and Ernst Ruska, who was awarded the Nobel Prize in 1986 for his fundamental work in electron optics and the design of the first electron microscope. During the last decades the TEM capabilities have been significantly improved with the development of spherical aberration correction, various analytic modes and associated modern detectors for X-rays, backscattered electrons, and the energy loss of electrons as shown in Figure 2.1.[74,111–113] These improvements have made TEM from a simple piece of imaging equipment to a comprehensive research toolbox indispensable for many science and technology disciplines. Nowadays, TEM is able to probe three distinct aspects of the structure of complex nanomaterials: in real space (imaging mode), in reciprocal space (diffraction mode), and in energy space (spectroscopic mode).

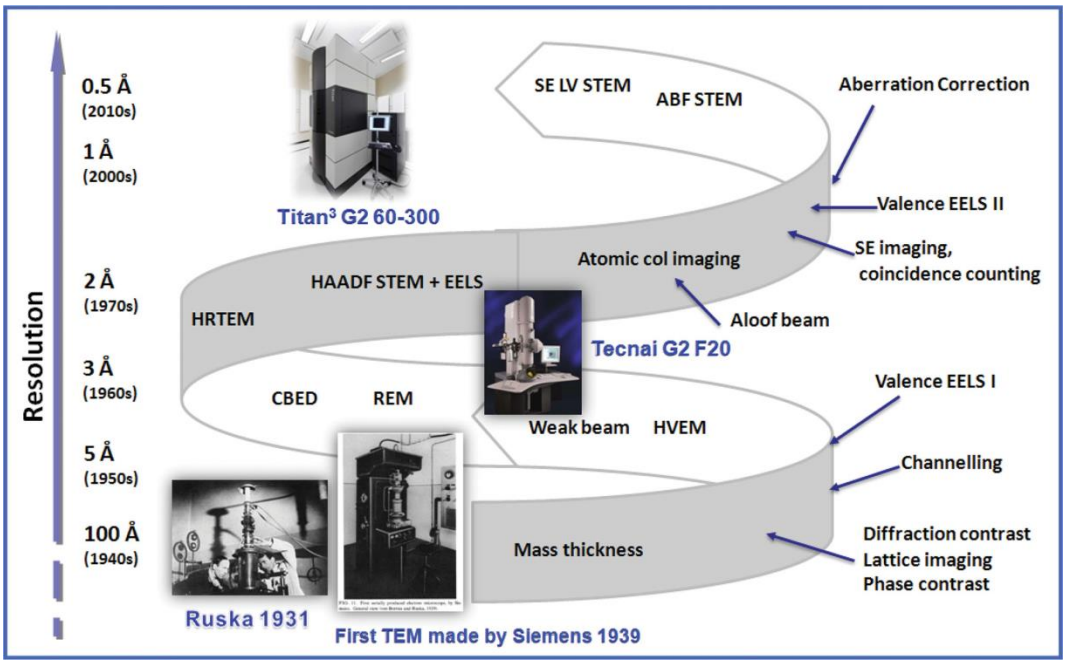

Figure 2.1: Milestones of TEM: the development of TEM from the first one to the modern aberration-corrected TEM with sub-angstrom resolution and the achievable spatial resolution (left side).[112]

The optical setup of a TEM is comparable to an optical microscope. From top to bottom, a TEM consists of an illumination system, a condenser lens system, an objective lens close to the sample, and a projection system as shown in Figure 2.2. The electron-emitter (gun) is the illumination source in a TEM and can be either a thermionic gun or a FEG. FEG emitters are used in high-end electron microscopes because they produce a more coherent and monochromatic electron beam, which can provide a smaller beam with higher brightness. The condenser system consists of two or three electromagnetic lenses and apertures. These lenses are used to control the beam size and convergence to form an electron beam with the desired intensity, size and convergence angle on the specimen. A condenser aperture is inserted to only allow the electrons on a path close to the optical axis to pass through, which is used to reduce the effect of aberrations caused by the lenses. After passing the condenser system, the electrons interact with the specimen mounted on a dedicated TEM holder. The interaction of the electron beam with the sample generates different scattered electrons and various useful signals that will be discussed later. The electrons emerging from the exit surface of the specimen are focused to form a diffraction pattern in the back focal plane of the objective lens. As shown in Figure 2.2c, the diffracted beams recombine and form an enlarged image in the image plane of the objective lens. Furthermore, an objective aperture, located in the back focal plane, can be inserted to select different diffraction spots to enhance the contrast in the final image. A selected area diffraction aperture can be inserted in the imaging plane of the objective lens to choose a specific region of the specimen, from which the diffraction pattern will be extracted. The resulting image, either from the back focal plane (diffraction pattern) or from the image plane (real space image) of the objective lens, can be magnified by the projector system. The final image is viewed on a fluorescent screen or captured using detectors such as charged coupled device (CCD), HAADF detector or spectrometer.

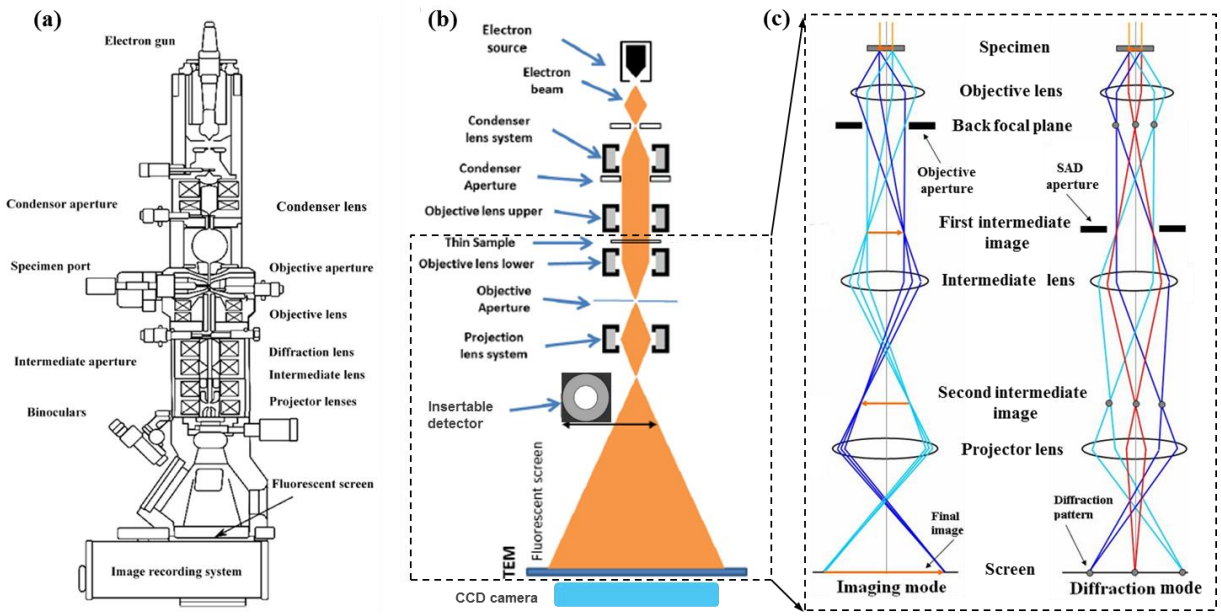

Figure 2.2: (a) Schematic outline of the internal components of a conventional TEM setup[114], (b) the electron-beam from electron source to the record plane (top to bottom) (modified from[115]) and (c) schematic diagram showing the ray path from specimen to screen in imaging and diffraction modes.

2.1.1. Electron beam-specimen interaction

When high-energy electrons pass through a thin specimen, the electrons interact strongly with the matter in the specimen, both with the electrons and with the nuclei of the atoms. A wide variety of signals are generated by this interaction as illustrated in Figure 2.3. The scattered electrons carry structural information of the probed specimen and the electron-specimen interaction is fundamental for understanding imaging and spectroscopy in TEM and the interpretation of results. The electron-scattering processes can be grouped into two types: elastic and inelastic. They correspond to scattering events that result in no energy loss or a measurable energy loss. Elastically scattered electrons are either the result of the incident beam electrons interacting with the negatively charged electron cloud (electron-electron interaction), which results in angular deviations of a few mrads or by interaction with the positive nucleus of an atom (electron-nucleus interaction), which scatters the electrons to much larger angles as shown in Figure 2.4a. The electron-nucleus interaction for the high-angle scattering is called Rutherford scattering and is related to the atomic number (Z) of the element.[115] Moreover, the elastic scattering of incident electrons at the lattice of a crystalline material gives rise to Bragg diffraction, which enables investigation of the crystal structure of the specimen.

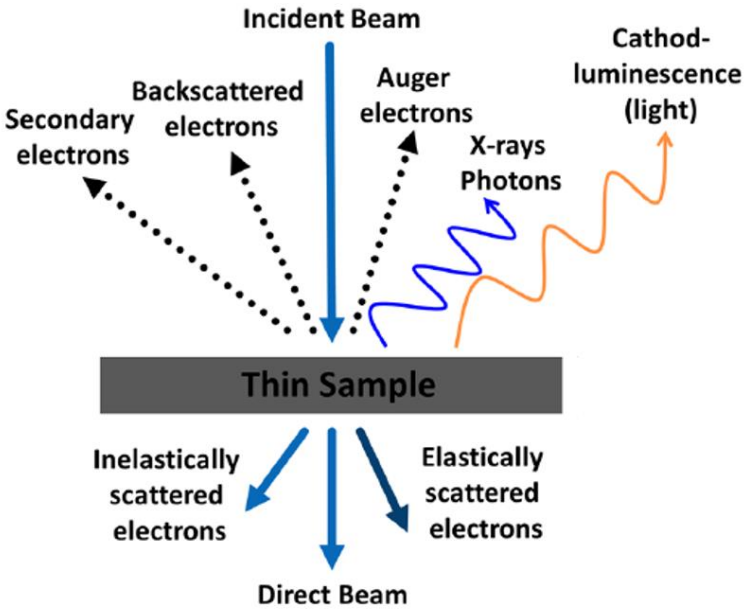

Figure 2.3: Electron beam-specimen interactions and the generated signals (adapted from[115]).

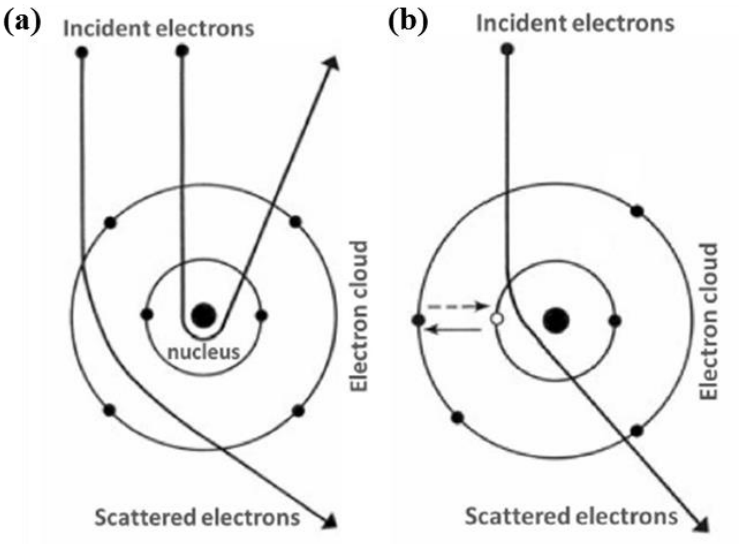

Figure 2.4: A classical (particle) view of electron scattering by a single atom (a) elastic scattering and (b) inelastic scattering (adapted from[116]).

In inelastic interactions, an incident electron transfers a certain amount of energy to an electron or the nucleus of an atom giving rise to electronic or vibronic transitions. In case of an electronic excitation, this results in an excitation from the ground state to an unoccupied orbital at a higher energy state in an outer shell or a complete removal of the electron. During this process and in the following relaxation process, where the ground state is filled again by an electron from a higher energy state, many important signals such as characteristic X-rays, auger electrons, secondary electrons and cathodoluminescence are generated, Moreover, the energy loss of the primary electron, which corresponds to the amount of energy transferred initially, can be analyzed using EELS. These signals generated by the inelastic interaction enable investigation of the chemical composition and electronic state of the specimen.

2.1.2. Imaging techniques in TEM

Bright-field and dark-field TEM

Bright-field TEM (BF-TEM) is one of the most common imaging modes in TEM. The specimen is illuminated by a parallel electron beam. Forward scattered electrons and electrons scattered to small angles mainly contribute to the image formation. The contrast of a BF-TEM image originates from two main mechanisms: mass-thickness contrast and diffraction contrast. The mass-thickness effect depends on the thickness, the atomic number Z and the density of the specimen. Denser regions will appear darker in the image since the electrons scattered to high angle are blocked by an objective aperture. In addition, if the incident electron beam is diffracted by any crystal lattice of the specimen (Bragg diffraction), this leads to scattering outside the objective aperture and thus contributes to diffraction contrast. The mass-thickness contrast is present in all materials, but for crystalline materials diffraction contrast typically dominates the image contrast, where the intensity of BF-TEM image is highly dependent on the orientation of specimen. Similarly, by tilting the primary beam a specific diffracted beam can be centered in the objective aperture for dark field TEM (DF-TEM) imaging. Regions in the specimen that diffract strongly within the selected angular range will be highlighted in the DF-TEM image. The ray diagrams for BF-TEM and DF-TEM imaging are illustrated in Figure 2.5, where either the transmitted beam or some of the forward scattered beams are used to form the final image formation.

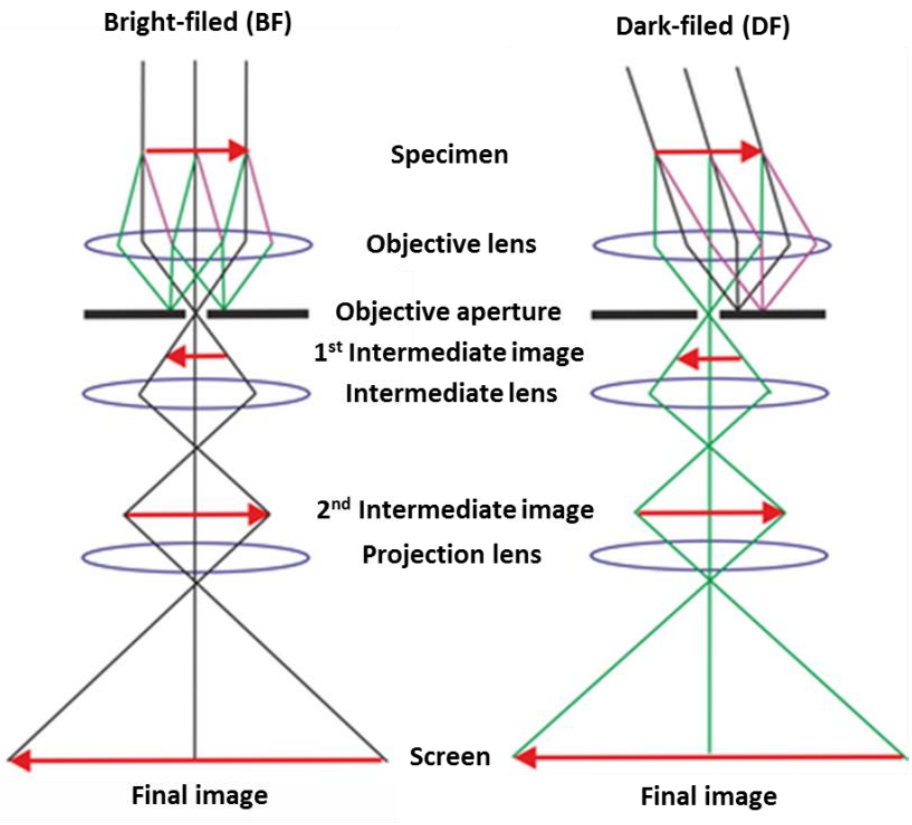

Figure 2.5: Electron ray diagrams of BF- and DF-TEM imaging (adapted from[117]).

High-resolution TEM

If the scattered beams are not blocked by an objective aperture, interference of the primary transmitted beam and the diffracted electron beams will generate an interference pattern, which contains information on the atomic structure of the specimen. To understand the information that can be gained from such a HRTEM image, the image formation process must be considered, taking into account the following three steps: (1) the propagation of the incident wave through the specimen, (2) the transfer of the exit wave by the optical system of the microscope and (3) the image formation on the recording device.[115,109] The incident electron beam can be approximated as a coherent plane wave on the sample surface. When the electron beam interacts with a sufficiently thin specimen, absorption of the electrons can be neglected. Thus, the amplitude of the electron wave is uniform, only the phase is affected by the specimen, which is called the phase object approximation. When the electron passes through this thin specimen, the potential (V_p) of the sample results in a change of the propagation speed of the electrons and thus in a phase shift. After the interaction with the sample, the phase of the electron wave at the exit plane of the sample ψ_{exit} contains structural information based on the potential variation within the sample. For a very thin area, this exit wave function can be further approximated considering only the first order term of the Tayler expansion of the exponential function:

$$\boldsymbol{\psi}_{exit}(\boldsymbol{r}) \approx e^{-i\delta V_p(\boldsymbol{r})} \approx 1 - i\delta V_p(\boldsymbol{r}) \qquad (2\text{-}1)$$

This approximation is called the weak phase object approximation. In this approximation, the imaginary part of the exit wave contains direct information on the projected potential of the sample.

The exit wave is affected by the objective lens, which results in further phase changes as it propagates through the optical system. The wave transferred through the optical system can be described by a convolution of the exit wave with the transfer function $\boldsymbol{T}(\mathrm{r})$ of the microscope:

$$\boldsymbol{\psi}_{image}(\boldsymbol{r}) = \boldsymbol{\psi}_{exit}(\boldsymbol{r}) \otimes \boldsymbol{T}(\boldsymbol{r}) \qquad (2\text{-}2)$$

This convolution in real space, can be expressed as

$$\widetilde{\boldsymbol{\psi}}_{image}(\boldsymbol{u}) = \widetilde{\boldsymbol{\psi}}_{exit}(\boldsymbol{u}) * \widetilde{\boldsymbol{T}}(\boldsymbol{u}) \qquad (2\text{-}3)$$

in reciprocal space ($\boldsymbol{u}$).

Assuming coherent illumination and no higher order aberrations, the transfer function $\boldsymbol{T}$ is given by

$$\widetilde{\boldsymbol{T}}(\boldsymbol{u}) = a(\boldsymbol{u}) exp 2\pi i \chi(\boldsymbol{u}) \qquad (2\text{-}4)$$

with the aberration function χ

$$\chi(\boldsymbol{u}) = \frac{1}{4} C_s \lambda^3 \boldsymbol{u}^4 + \frac{1}{2} \Delta f \lambda \boldsymbol{u}^2 \qquad (2\text{-}5)$$

and the aperture representation $a(\boldsymbol{u})$ of an aperture of size d in the back focal plane of the objective lens ($a(\boldsymbol{u})$ = 1 for $|\boldsymbol{u}|$ < d and 0 for $|\boldsymbol{u}|$ > d). λ is the electron wavelength, Δf is the defocus of the objective lens and C_s is the spherical aberration coefficient of the objective lens. The spherical aberration is due to an inherent limitation of the round electromagnetic lenses used in TEMs. Electrons passing further from the optical axis are focused more strongly compared to electrons on the optical axis. As a result, a point object is imaged as a disk of finite size, which limits the ability to magnify details because the feature is degraded in the imaging process. Alternatively, this can be expressed by the aberration function χ resulting in an additional phase shift of the exit wave.

When the interference pattern of the image wave is recorded, the image intensity can be expressed within the weak phase object approximation as:

$$I_{image}(r) = \left|\boldsymbol{\psi}_{image}\right|^2 \approx 1 + 2\delta V_p \otimes \mathcal{F}^{-1}\left[\sin\left(\frac{1}{2}\pi C_s\lambda^3\boldsymbol{u}^4 + \pi\Delta f\lambda\boldsymbol{u}^2\right)\right] \quad (2\text{-}6)$$

where $\sin\left(\frac{1}{2}\pi C_s\lambda^3\boldsymbol{u}^4 + \pi\Delta f\lambda\boldsymbol{u}^2\right)$ is referred to as the contrast transfer function (CTF), describing the modification of the image intensity by the defocus (Δf) and the spherical aberration coefficient (C_s). From equation (2-1) to (2-6), it can be seen that the phase shift produced by the interaction with the specimen is further modified by the objective system, which leads to a transfer of the imaginary part of the electron wave to intensity variations in the interference image. This is the phase contrast using in HRTEM imaging.

The CTF gives the phase shift introduced by the defocus (Δf) and the spherical aberration (C_s) as a function of spatial frequency (Figure 2.6a). The effect of the oscillations of the CTF was first understood by Scherzer, that the contrast of atoms depends on the interatomic distances and the defocus chosen. As illustrated in Figure 2.6b, the atom columns in HRTEM image can be either a bright or a dark spot when the defocus value changes. With a certain defocus, because of different interatomic spacing (i.e. the spatial frequency), the lattices of an fcc-Au crystal structure exhibit different signs in the CTF (Figure. 2.6a), which will produce different contrast for the lattices in the image plane. In order to intuitively interpret HRTEM images of weak-phase objects, the phase shift should be constant (or at least have the same sign) over a wide range of spatial frequencies. This can be achieved with a particular defocus value, known as 'Scherzer focus' Δf_{Sch}:

$$\Delta f_{Sch} = -\left(\frac{4}{3}C_s\lambda\right)^{1/2} \quad (2\text{-}7)$$

At the Scherzer focus, the HRTEM image of a weak-phase object represents the projected atomic potential up to the first zero transition of the CTF, which defines the point resolution (d_p) of the TEM:

$$d_p = 0.66{C_s}^{1/4}\lambda^{3/4} \quad (2\text{-}8)$$

This point resolution sets the limit for a straightforward interpretation of a HRTEM image of a thin object. In practice, information about the specimen with higher resolution (higher frequencies

transferred) can be obtained from a TEM. This transfer is limited by the coherence of the electron source and electronic instabilities of the microscope. The limited coherence is mainly due to two effects. The limited temporal coherence is due to the effect of the chromatic aberration (C_c) of the objective lens coupled with the energy spread of the beam. When the electron beam is not perfectly monochromatic, the chromatic aberration of the objective lens causes electrons of different wavelength (energy) to be focused at different levels, which results in a focus spread in the image plane. This will not result in noticeable differences for low spatial frequencies, but for high frequencies, where the CTF varies rapidly with defocus, the variations will start to cancel each other out, therefore limiting the information that is transferred to the image. The limited spatial coherence results from the fact that the thin object is illuminated by an electron beam produced from a source with an angular spread. This angular spread will result in a slight phase shift 'smearing' out the smallest features. Mathematically, these two effects can be described by a damping function (E) applied to the CTF, as shown in Figure 2.6a. This partial coherence puts a limit to the information that can be transferred in a TEM, so called the information limit. The information limit is defined as the spatial frequency, where the contrast (the temporal envelope function) falls off to $1/e^2$ (~13.5%) and is a measure for the spatial frequency where interpretable information is transferred in the imaging process.

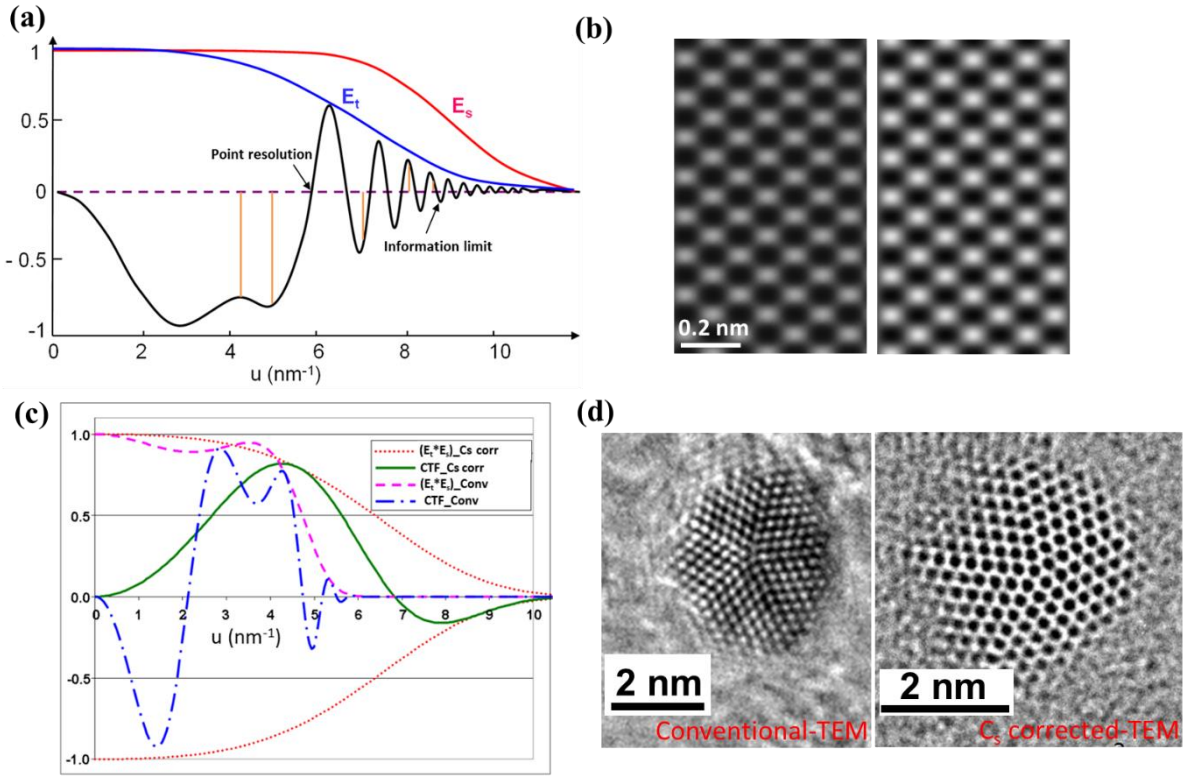

Figure 2.6: The CTF of a Tecnai F20 ST microscope (200kV) at the Scherzer focus with the damping functions for partial temporal coherence (E_t) and partial spatial coherence (E_s), the orange vertical lines in the CTF indicate the phase shift of lattices (111, 200, 220, 113 and 222) of an fcc_Au (modified from[119]), (b) the simulated HRTEM images on the [110] zone axis of fcc-Au structure with different defocus, (c) typical partially coherence CTF for a conventional microscope (blue dash-dot line) and for a C_s corrected microscope (green solid line)[119], (d) HRTEM images of Au NP in the conventional microscope and the C_s corrected microscope.

In practice, the point resolution of HRTEM could be further affected by other aberrations of the objective lens, which introduce additional phase shifts. When the microscope is well aligned, one of the common aberrations is astigmatism, which introduces phase variations and therefore affects the defocus values in different directions. For instance, two-fold astigmatism can result in different defocus along perpendicular directions. Similarly, higher order astigmatism produces directional dependent contrast transfer along more than two axes. Moreover, other aberrations, such as higher order spherical aberration and the star aberration, still introduces additional phase shift when astigmatisms are corrected. As this phase shift induced by n-fold aberration depends on $\boldsymbol{u}^n$, these higher order astigmatism and aberration become increasingly important with increasing resolution. Recently, aberrations of lens including astigmatisms, spherical aberration and high order aberrations have been corrected properly by the rapid development of aberration corrections, which dramatically improved the point resolution of TEMs to more clearly imaging the atomic structures. For example, by using a hexapole spherical aberration corrector, the higher order spherical aberration can be determined and corrected by the means of beam-tilted diffractogram series. As illustrated in Figure 2.6c, the point resolution of a C_s corrector microscope is significantly improved compared to a conventional microscope. A wide range of spatial frequencies in this C_s corrector microscope exhibits the same sign of the phase, whereby the contrast of HRTEM image is more directly interpretable. Moreover, the contrast delocalization, which is the lateral displacement of spatial frequencies in the HRTEM image due to the spherical aberration of the objective lens, is also significantly suppressed in the C_s corrector microscope. As shown in HRTEM images of Au NPs (Figure 2.6d), the typical delocalization effect, where lattice fringes appear to continue well beyond the edge of the specimen into the support film or vacuum, is eliminated by the spherical aberration corrector.

It should be noted that the above discussion of the image formation process was based on the weak phase object approximation for the specimen. However, in practice, the sample thickness never fully fits this assumption. The propagation of the incident electron wave through the specimen is determined by the scattering of atoms in the material, where the Coulomb interaction between atoms and the incident electrons leads to the phase shift of the incident wave. In the propagation through a real specimen, the phase of the incident wave varies more than once due to the multiple scattering of the incident electron by atoms of the specimen. As such, the phase shift of the incident wave undergoes a dynamic process and the final phase of the exit wave highly varies with the thickness. The Bloch wave method and the multi-slice method have been developed to understand the dynamic process and to calculate the exit wave function, therefore investigating the thickness effect on the final contrast (intensity) of HRTEM in the image plane. The above discussion has demonstrated that the interpretation of HRTEM image is not necessarily intuitive and always needs to consider defocus, astigmatism and higher order aberrations of the imaging lenses that introduced additional phase shifts, as well as the thickness of the irradiated area. To better interpret the atomic structure in HRETM, image simulations are needed to match the phase contrast to a real structure model.[120]

Scanning transmission electron microscopy

STEM is another widely used imaging mode in a modern electron microscope. In STEM, the electron beam is converged to a small probe focused on the specimen. This convergent beam is then moved point-by-point across an area of the specimen and the electrons scattered to a certain angular range are collected by a detector for each imaging point, representing the intensity at this point in a STEM image. The probe is formed as illustrated in Figure 2.7a, the condenser lens demagnify the image of the electron source (gun) and the electron beam passed through the condenser aperture is focused to form a convergent probe at the height of the specimen by the pre-field of objective lens. In STEM, two objects with a distance smaller than the size of the forming probe cannot be resolved. As such, the resolution in STEM imaging is fundamentally limited by the probe size. For a given microscope high tension and for a given demagnification of the source, i.e., the electron wavelength and the effective source size are fixed, the remaining parameters for the optimization of the probe are the defocus, aberrations of the probe forming lens and the size of condenser aperture. The influence of defocus on the probe has been demonstrated in Figure 2.7b. The in-focusing shows the highest profile intensity and the smallest probe size compared to the under-focusing and the over-focusing. In experimental, the in-focusing can be nearly achieved by optimizing the contrast (sharpness of features) of an STEM image. As mentioned, the spherical aberration of lens results in a disk of finite size from a point object. Therefore, in STEM the spherical aberration of condenser lens will broaden the formed probe size and significantly degrade the resolution. Other aberrations of condenser lens, such as astigmatism, need be also considered in the formation of the probe. Generally, the aberration effect can be determined in a Ronchigram, which is a convergent beam diffraction pattern of a specimen. For example, astigmatism influences features in the Ronchigram, shown in Figure 2.7c. After astigmatism corrected, the Ronchigram gives rise to an infinitely magnified projection image. To reduce the aberration effects on the probe, the angular aperture is inserted behind the crossover formed by the condenser lens. In practice, this means that only a small fraction of the emitted beam current will end up in the probe. As illustrated in Figure 2.7d, the convergence semi-angle (α), which depends on the size of condenser aperture ($d_{aperture}$), not only affects the size of the probe, but also changes the intensity. In addition, the convergence angle also influence the depth of field. As it is proportional to the inverse square of the convergence angle, the depth of field can be increased by using a small convergence angle at the expense of beam current, the probe size and the image signal. The increased depth of field greatly helps to imaging thick samples for STEM tomography because it reduces the beam spread on the top and bottom surfaces of an imaged point.

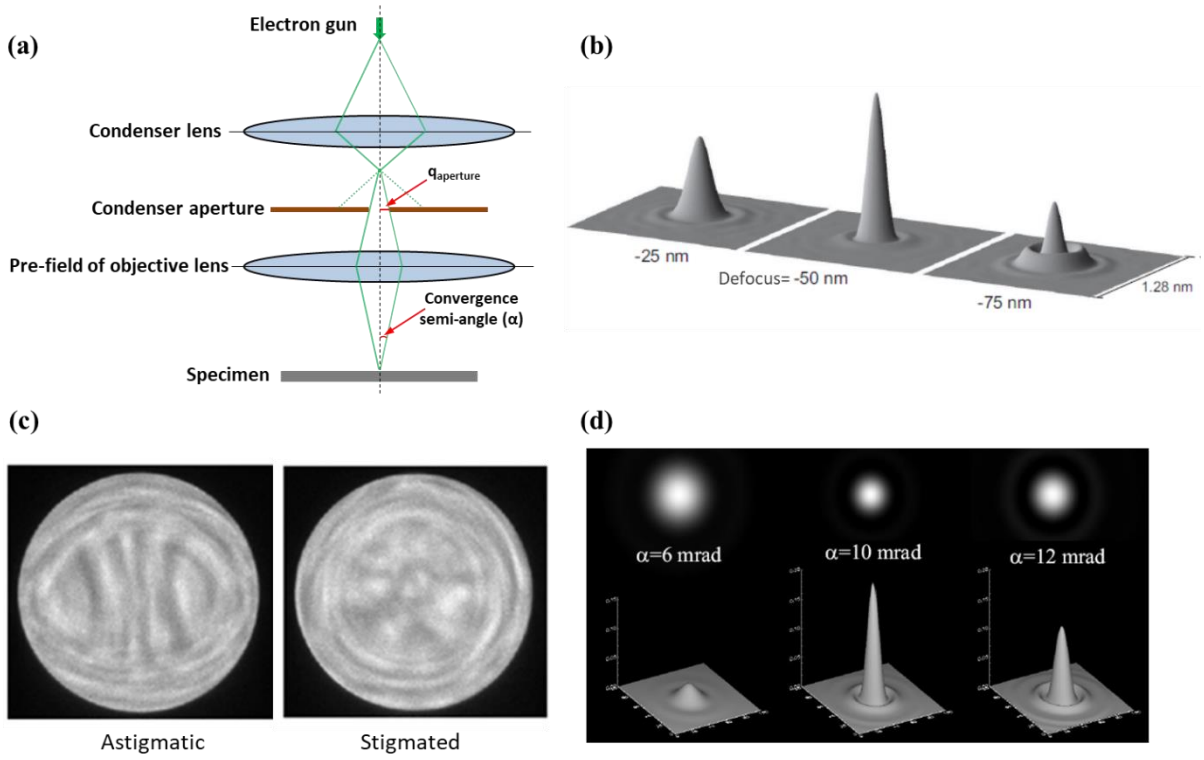

Figure 2.7: (a) The forming of the probe in STEM mode, (b) the probes with a defocus of -25 nm (over-focusing), -50 nm (in-focusing) and -75 nm (under-focusing)[121], (c) Ronchigrams with astigmatism and after astigmatism corrected[122], and (d) the influence of convergence semi-angle (α), i.e. the size of condenser aperture ($d_{aperture}$), on the size and the intensity profile of STEM probe.[123]

In a conventional microscope, the best resolution is achieved with the optimum aperture (the semi-angle α_{opt}), given by:

$$\alpha_{opt} = 1.41\left(\lambda/C_s\right)^{\frac{1}{4}} \qquad (2\text{-}9)$$

with the defocus is chosen to provide an exactly compensating contribution of this optimum aperture and is given by:

$$\Delta f_{opt} = -\sqrt{\lambda C_s} \qquad (2\text{-}10)$$

As the Airy disk describes the best-focused spot with a circular aperture[124], the profile of probe is quite similar to the Airy disk distribution. The STEM resolution (d) of the conventional microscope is thus normally taken as the Rayleigh criterion for a circular aperture, the radius of the first zero, $0.61\ \lambda/\alpha_{opt}$, giving

$$d = 0.43\lambda^{3/4}C_s^{1/4} \qquad (2\text{-}11)$$

This demonstrates that the optimum resolution (d) is limited by the spherical aberration (C_s). Fortunately, the rapid development of aberration correctors greatly compensates aberrations of the probe forming lens, to achieve the small intense probes. So far, the aberration-corrected electron

microscopy has achieved the ultimate resolution of STEM to ~40 pm, which greatly help to investigate the atomic structure of materials.

Depending on the angular range of the collected scattered electrons, there are three main imaging modes used in STEM: bright field (BF), annular dark field (ADF) and HAADF as shown in Figure 2.8. The angular range of the scattered electrons determines the contrast of the STEM image. BF-STEM images are typically formed from both the transmitted electrons and the low angle scattered electrons (<10 mrads), closely related to BF-TEM images following the reciprocity principle between BF-TEM and BF-STEM. The contrast in BF-STEM images is mainly dominated by Brag diffraction. With increasing collection angle, electrons that experienced Rutherford scattering and thermal diffusive scattering are collected by the ADF detector (medium angle) in addition to Bragg scattered electrons, resulting in a complicated contrast for the ADF-STEM image. When further increasing the collection angle, the lower angle scattered electrons are not collected by the HAADF detector and therefore the contrast of HAADF-STEM image is dominated by Rutherford scattering and thermal diffuse scattering.

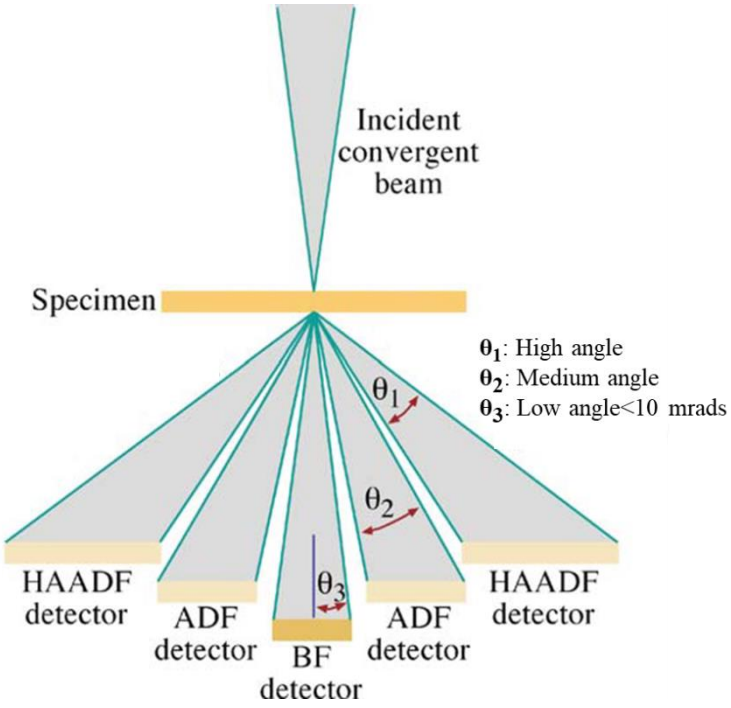

Figure 2.8: Schematic of the BE, ADF and HAADF detectors setup for STEM imaging (adapted from [115]).

Equation 2-12 is describing the differential cross section (δ) for Rutherford scattering by the nucleus alone.

$$\delta = \frac{e^4 Z^2}{16(4\pi\varepsilon_0 E_0)^2} \frac{d\Omega}{\sin^4\frac{\theta}{2}} \qquad (2\text{-}12)$$

where E_o is the beam energy, ε_o is the vacuum permittivity, θ is the scattering angle, e is the charge of an electron and Ω is the total solid angle of scattering. It shows that the scattering probability at high angels is proportional to the square of Z. As the nucleus is partially shielded by the surrounding electrons, the scattering probably is reduced depending on the electron configuration around the

nucleus resulting in a probability of $Z^{1.6}$ to Z^2 in real materials.[125] Furthermore, when consider that the specimen contains N atoms/unit volume with a certain thickness (t), the probability of Rutherford scattering from the specimen is given by:

$$\delta_{total} = N\delta t = \frac{N_0 \delta(\rho t)}{A} \qquad (2\text{-}13)$$

where N_0 is Avogadro's number, A is the atomic weight of the scattering atoms and ρ is the density in the specimen. Here the total probability (δ_{total}) of Rutherford scattering in the specimen corresponds to the product of ρ and t, which is called the mass-thickness. Therefore, high angle scattering in a thick specimen (and/or a high-density part) becomes more compared to a thin specimen (and/or a low-density part).

The above description of Rutherford scattering only considers stationary atomic nuclei. However, in practice, atoms in the specimen vibrate thermally with a typical frequency of 10^{12}–10^{13} Hz, and this atomic vibration is quantized as a phonon. Thermal diffuse scattering is describing the scattering of the incident electrons by vibrated atoms in the specimen. It is helpful to understand this scattering by considering the path of individual electrons on their journey through the sample. For instance, the velocity of electrons in a microscope operated at 200 kV is approximately $2\text{x}10^8$ m/s, so it takes around $1\text{x}10^{-15}$ s to pass through a sample with ~200 nm thickness. Thus, the electron passes through the sample much faster than the time needed for a vibronic oscillation of the nuclei in the sample. This means that the electrons will be scattered from atomic nuclei at random positions within their vibrational trajectory, liking a diffuse manner. With a large number of the electron-nucleus interaction, the thermal diffuse scattering can result in a high angle scattering.

The above discussion of Rutherford scattering and the thermal diffuse scattering has clearly indicated that the intensity of HAADF-STEM image corresponds to the thickness of the specimen and is approximately proportional to the power of the average atomic number in the specimen integrated over the thickness. Therefore, the generated HAADF-STEM images are directly interpretable (at least qualitatively). More importantly, the chemical sensitivity of HAADF-STEM, from the strong dependence of the scattered intensity on atomic number, makes this technique an excellent tool for the investigation of supported catalysts in this thesis. A high contrast of HAADF-STEM image can be generated between the supports (low-Z) and the supported particles (high-Z).

2.1.3. Spectroscopic techniques

Modern electron microscopes can provide chemical and electronic structure information for specimen based on the inelastic scattering processes as mentioned in section 2.1.1. EDXS and EELS are the two most commonly used techniques to obtain these information. The processes for inelastic interaction of an incident electrons and electrons of the specimen are shown in Figure 2.9. A high-energy beam electron interacts with an inner (core)-shell electron or an outer-shell electron of atom,

resulting in a core shell excitation or an outer shell excitation, where the excitations reflect the chemical, electric and magnetic properties of the specimen.

In the core shell excitation, when a sufficient amount of energy is transferred from the incident electron to the inner-shell electron, this inner-shell electron can make an upward transition to an unoccupied orbital at higher energy level or even escape the attractive field of the nucleus. The energy loss of the incident electrons, i.e., the transition energy of this core shell excitation, is typically hundreds or thousands of electron volts and characteristic for each element. This excitation leaves a hole in the inner shell and results in the atom in an excited state or in an ionized atom. This exited state is unstable and an electron from the higher energy shell fills the hole, accompanied by the emission of an X-ray or photon. The energy of the emitted radiation is characteristic for each element as it corresponds to the energy difference between the different orbitals of this element. Moreover, the characteristic set of all transitions for the core shell excitation/de-excitation of an atom should satisfy the quantum mechanical selection rules, as illustrated in Figure 2.9c. Compared to the core shell excitation, the outer shell excitation is derived from the interaction between incident electrons and outer-shell electrons of atoms or valence electrons of specimen. All excitations from the outer most occupied shells are also the element specific transitions. Moreover, plasmon excitation is one of the important outer shell processes. The outer shell electrons are only weakly bound to the atoms, and therefore easily delocalized. The delocalized electrons are correlated with each other through electrostatic forces, forming a valence electron 'cloud' among many atoms of materials (typically metals). When the incident electrons penetrate the specimen, the Coulomb interaction between the incident electrons and the valence electron cloud will result in an oscillation of this cloud, leading to an energy loss of the incident electrons. Beside the plasmon excitation, single-electron excitation is another outer shell excitation. This process usually involves interband transitions of a valence electron from the valence band to the conduction band, with the energy transmitted from incident electrons. Typically, the energy loss of incident electrons in the outer shell excitation is less than 100 eV.

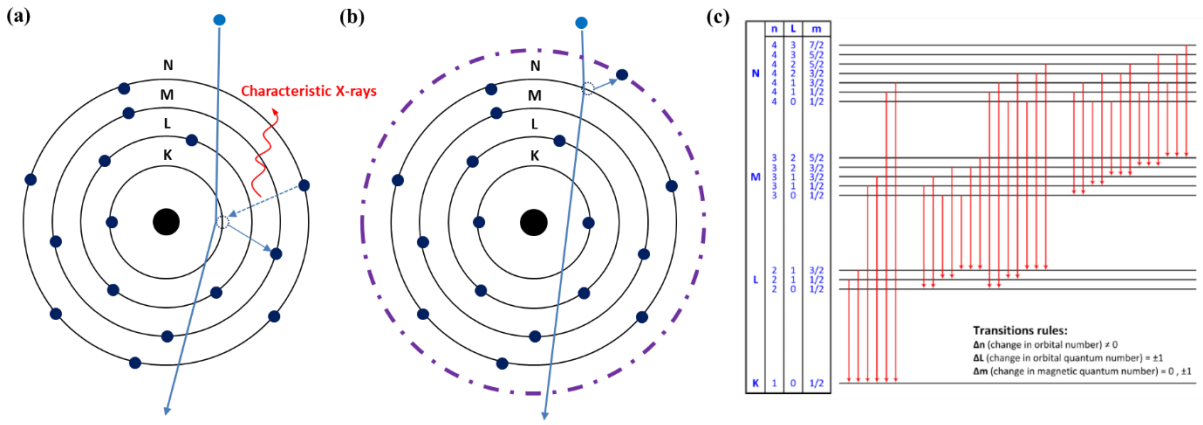

Figure 2.9: Inelastic scattering of (a) core shell excitation and (b) outer shell excitation, (c) all allowed transitions of the core shell excitation between the K, L, M, and N shells of an atom[126].

Energy dispersive X-ray spectroscopy

In EDXS, detection and analysis of the energy of the emitted X-rays is based on the creation of electron-hole pairs in a detection layer by the incoming X-rays. The number of generated pairs is proportional to the energy of the characteristic X-ray. By applying a bias across the detector, the pairs are separated and drift to the electrodes, where a current corresponding to the number of electron-hole pairs can be measured (after amplification). Thus, depending on the current, the energy of each X-ray can be determined. By collecting a sufficient number of measurements, the characteristic X-rays from elements give rise to different peaks in an EDX spectrum, where the peak intensity relates to the number of emitted X-rays.[127] An example of an EDX spectrum is shown in Figure 2.10a. It shows peaks due to characteristic X-rays on a continuum background produced by the Bremsstrahlung. For an accurate quantification, the Bremsstrahlung background has to be subtracted. Moreover, reabsorption of X-rays within the specimen and at the detector entrance have to be considered as well as X-ray fluorescence, where a high-energy X-ray can excite a lower energy X-ray emission in another part of the sample.[128] This fluorescence effect becomes especially relevant for two elements with similar emission/absorption energies. When properly considering the above effects, the composition of the specimen could be quantified from the EDX spectra. Furthermore, in combination with STEM imaging, the EDX spectrum at each pixel can be evaluated and the characteristic X-ray peaks can be selected by an energy window around the characteristic energy to map elements distribution in the specimen.

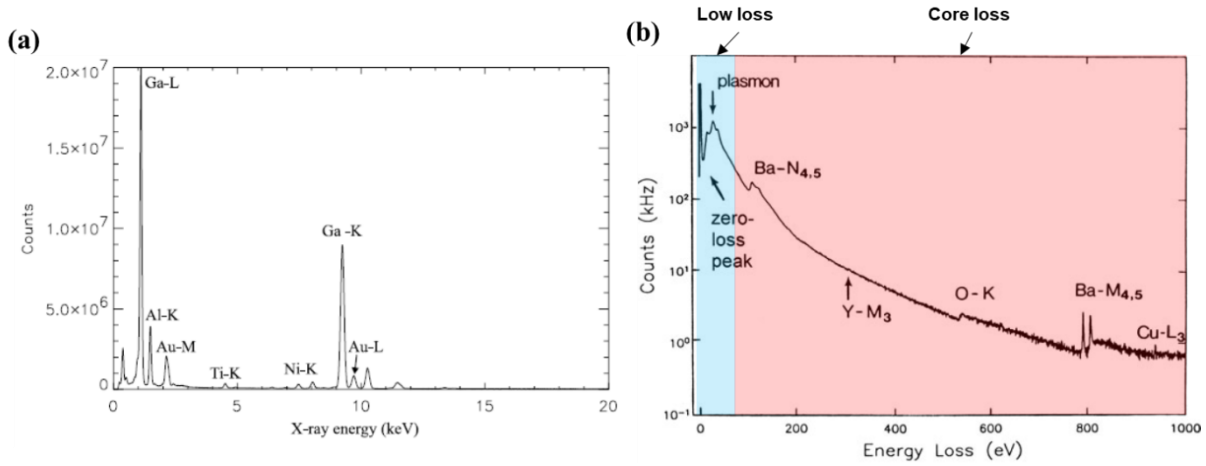

Figure 2.10: (a) An example of EDX spectrum taken from an AlGaN based specimen[129] and an example of EELS spectrum from an $YBa_2Cu_3O_7$ specimen, showing zero-loss and plasmon peaks and ionization edges arising from each element (modified from[116]).

Electron energy loss spectroscopy

In EELS, the energy-loss of inelastically scattered electrons provides not only information on the chemical composition of a specimen, but also a wealth of information such as absolute thickness, valence state, electrical conductivity and band gaps. These information cannot be obtained by EDXS. The EELS measurements are typically performed using a spectrometer, where the main part of the spectrometer is a magnetic prism. When electrons pass through the magnetic prism, they are deflected depending on their energy (due to the Lorentz force) leading to a separation of the electrons depending on the energy

perpendicular to the magnetic field. The formed energy loss spectrum is imaged by a detector on the energy dispersive plane. An example of EELS spectrum is illustrated in Figure 2.10b, showing zero-loss, plasmon peaks and ionization edges arising from elements. Generally, there are two regions to be considered in EELS: the low loss region up to 50 eV and the core loss region. The low loss region consists of a sharp peak (zero-loss peak) that corresponds to the elastically scattered electrons and a number of broad peaks corresponding to plasmon losses, which contain the information of the dielectric function, band gap and the sample thickness.[130] On the other hand, the information about the composition (the edge intensity) as well as the oxidation state/local atomic environment (near edge fine structure) can be provided in the core-loss region with the characteristic inner shell excitation edges. EELS can also be recorded in STEM mode to form element specific imaging similar to EDXS. However, STEM-EDX/EELS mapping is quite time consuming and alternatively, with an energy selecting slit inserted in the dispersion plane, these electrons can be used to from a real space energy filtered (EFTEM) image with a defined energy loss again. This approach is much faster for imaging element distributions, especially for large areas.

2.2. Introduction to electron tomography: a brief history and principles

Classical TEM and STEM imaging techniques only provide 2D projections of a 3D object. To image complex 3D nano-structured materials, electron tomography is essential for a direct, model-independent structure elucidation at nanoscale. In electron tomography, a series of 2D projected images of an object (specimen) at different projection directions is recorded and these projections are combined to reconstruct a 3D representation of the original object, which can be analyzed by advanced technique to develop a description of characteristic features.

2.2.1. Important developments of electron tomography

The mathematical foundation of tomography is based on the work by Radon in 1917. He introduced the so called Radon transform and showed that a 2D object can be uniquely described by an infinite number of 1D projections.[131] By inverting the Radon transform, the 2D object can be fully restored from the projections, if the projections are produced by a strictly monotonic function from the 2D object. The first practical implementation of tomography was achieved by Bracewell to reconstruct 2D radio astronomy data from 1D line integrals in 1956.[132] Interest in tomographic reconstructions from electron micrographs started with the publication of three seminar papers in 1968. De Rosier and Klug determined the structure of a helically symmetric virus by Fourier reconstruction methods that allowed full reconstruction from a single projected electron micrograph.[14] Hoppe and coworkers demonstrated that 3D reconstruction should be possible for asymmetric materials with a sufficient number of projections.[66] The work of Hart and coworkers defined the principles of electron tomography for reconstructing asymmetric 3D objects from a tilt series of 2D TEM projections.[15]

Electron tomography remained in the field of life sciences until the late 1990s. The first electron microscopy work focusing on materials science has been demonstrated in 2000.[133] The application of

STEM-HAADF tomography by Midgley et al.[107,134–136] and Kübel et al.[67,70] has contributed to a rapid uptake of tomographic methods in physical sciences. The fast development was soon fostered by adopting other imaging techniques including EFTEM,[107,137] ADF TEM,[138] and weak-beam dark-field imaging.[139,140] Moreover, electron tomography works from De Jong's group[72,76,141–144] have pioneered 3D characterizations of the structure of nanomaterials, especially in the field of catalysis. Recently, STEM-EDX/EELS tomography has become increasingly popular to characterize 3D nanostructures with chemical sensitivity.[105–108] These great developments of electron tomography have benefited from several significant improvements in last decades[74,111]: Firstly, progress in modern hardware, such as implementation of aberration correctors, computer controlled goniometers, novel tomography holders, and more sensitive electron detectors, has led to an increase in spatial resolution and facilitated data acquisition. Secondly, software and algorithm developments, including automation of microscope control, new reconstruction algorithms and advanced image processing, have made more robust and reliable reconstruction and segmentation for a quantitative analysis possible. Last but not least, there have been major developments in spectroscopic techniques, such as increased sensitivity in EDXS and EELS, which enable high quality mapping to elucidate not merely the morphology but also composition and even the electronic states and other physiochemical parameters in 3D, within reasonable acquisition time and electron dose.

2.2.2. Principles of tomographic image reconstruction

The Radon transform

Radon's theory describes how an object D in real space $f(x,y)$ can be described by line integrals of all possible lines L through that object (Figure 2.11):

$$Rf = \int_L f(x,y)\,\mathrm{d}s \qquad (2\text{-}14)$$

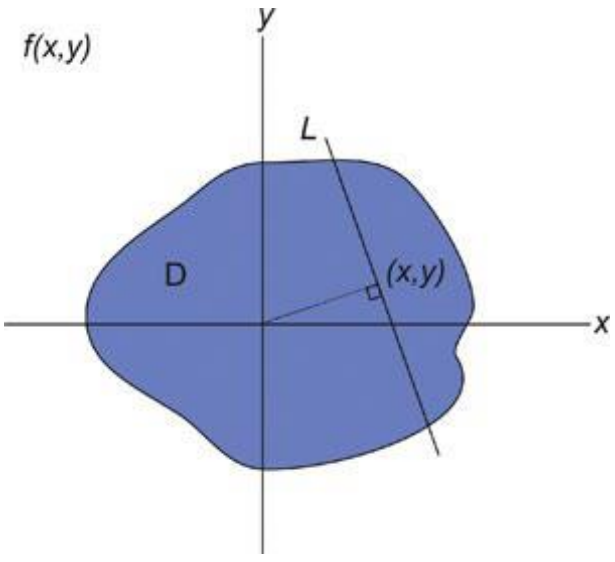

Figure 2.11: The Radon transform defines the projection of an object D in Cartesian space (x,y) through an infinite number of lines (L).[145]

For an explicit definition of the Radon transform (R), a new set of coordinates that are perpendicular (l) and parallel (z) to the projection/transform direction defined by the ray L is defined. The angle (θ) between the horizontal and the line normal of L is usually termed as the projection angle. Figure 2.12a illustrates the geometry of these terms. With the new set of coordinates, a more explicit statement of the Radon transform is achieved:

$$\begin{cases} Rf(l,\theta)=\int_{-\infty}^{\infty} f(\sqrt{l^2+z^2}, \theta+\tan^{-1}(z/l))dz, & l\neq 0 \\ Rf(0,\theta)=\int_{-\infty}^{\infty} f\left(z,\theta+\frac{\pi}{2}\right), & l=0 \end{cases} \quad (2\text{-}15)$$

The Radon transform operation converts the coordinates of an object into Radon space (l, θ), where l is the line perpendicular to the projection direction and θ is the projection angle. As shown in Figure 2.12b, a point (x, y) in real space becomes a line in Radon space (l, θ) through the equation $l = r\cos(\theta - \phi)$. Figure 2.13 illustrates a 2D object of the Radon transformation over a full range of ±180°, where the bright spots are converted into sine curves in the Radon-transformed object. Thus, the Radon space image is often termed as a 'sinogram'.

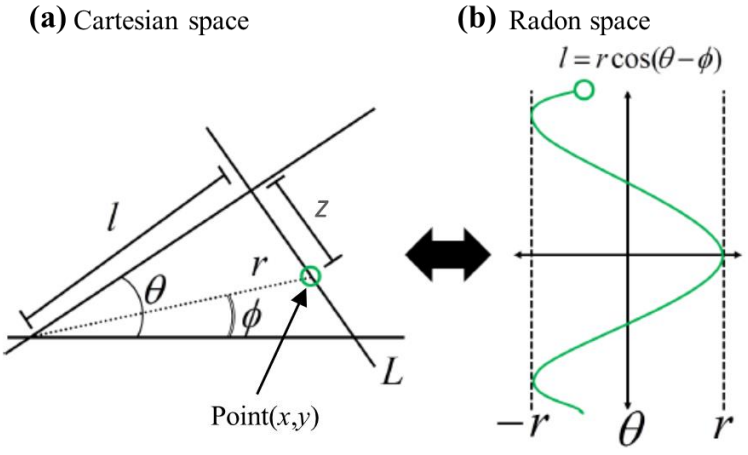

Figure 2.12: The Radon transform converts objects in Cartesian space (a) to Radon space (b), measured in terms of the projection angle (θ) and the distance from the origin (l). A point in real space (x, y) is converted into a line with the equation $l = r\cos(\theta - \phi)$. (adapted from [145])

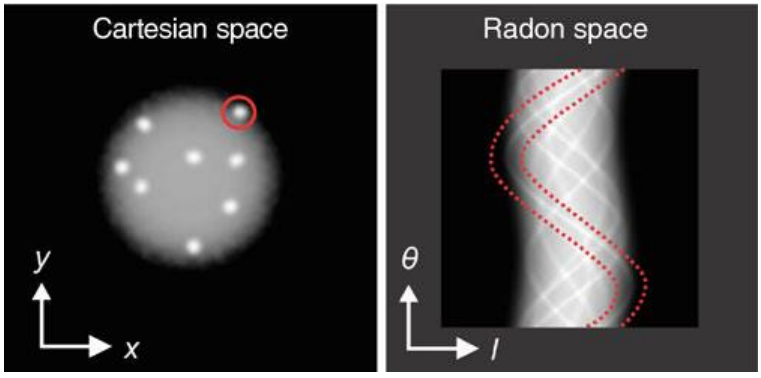

Figure 2.13: The Radon transform applied to a 2D object over a full range of tilt ±180°, where a point object circled in Cartesian space becomes a sinusoidal line (dashed lines) in Radon space.[145]

The relationship between real space and Radon space indicates that a discrete sampling of the Radon transform is geometrically equivalent to the sampling of an object by some form of transmitted signal: a projection. Therefore, a series of projections at different angles provides an increased sampling of Radon space. With an infinite number of projections, a reconstruction of an object can be obtained by finding the inverse Radon transform. In practice, the sampling in Radon space is discrete with a limited numbers of projections. Nevertheless, the 3D structure of the original object can be approximated with a sufficient number of projections.

Direct back-projection: real space reconstruction

The work by Radon has shown the equivalence of an object and all of its projections, an explicit closed description of the Radon transform has not been achieved. However, one approach to reconstruct the original object from a discrete number of projections in real space is the back-projection approach.[146,147] This approach sums all 2D projections of a volume at different projection angles to restore the 3D object. For a point object, the back-projection of a single projection becomes a ray crossing the volume in the projection direction (Figure 2.14b). This does not allow to locate the point object in 3D and more projections are thus needed. With two back-projections from different directions, an increase in total intensity will be observed at the cross point of the two rays, which corresponds to the location of the original object (Figure 2.14c); with an increasing number of projections, the point object becomes increasingly well defined. More 'rays' are required to describe extended objects uniquely, to represent the shape of the object. By combining a sufficient number of back-projections from different directions, the shape of the original object can be restored (Figure 2.14d-g).[145] In this process, the sampling of projections closely controls the resolution of the tomographic reconstruction. A limited angular sampling causes streaking artifacts in the reconstructed image, seriously degrading the reconstruction resolution in this direction. For a single-axis tilt geometry, the resolution along the tilt axis direction (the x-axis), dx, is equal to the original resolution of the projections, assuming a perfect tilt series alignment. The resolution in the other perpendicular directions (dy, dz) is controlled by the number of projections (N) and the diameter (D) of the volume to be reconstructed:[148]

$$dy = dz = \frac{\pi D}{N} \tag{2-16}$$

However, using this simple direct back-projection, the resulting reconstruction does not look particularly good; it exhibits strong low frequency blurring. This can be understood by considering the reconstruction in reciprocal space.

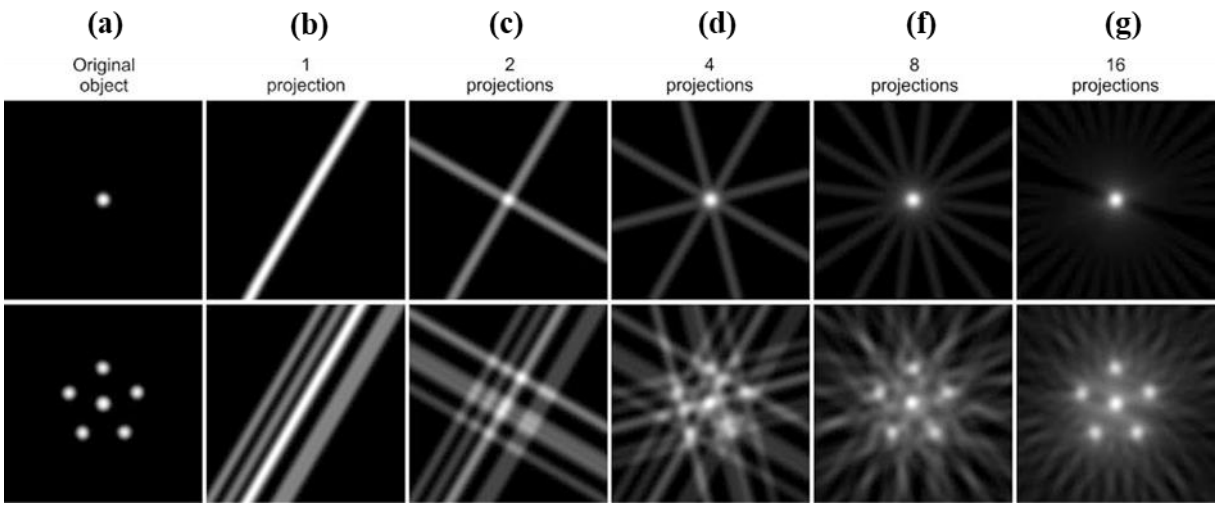

Figure 2.14: Direct back-projection reconstruction combined number of rays with different directions.[145]

3D reconstruction in reciprocal space

The central slice theorem states that the Fourier transform of a projection of an object obtained at a certain projection angle corresponds to a section through the 3D Fourier transform of that object at the same angle.[13,149,150] Thus, a series of projections acquired at different tilt angles is equivalent to a series of central sections through 3D Fourier space of that object.[149] By inverse Fourier transform of the combined slices in reciprocal space, the 3D structure of the object can in principle be reconstructed. A schematic representation of the tomographic reconstruction using the central slice theorem is depicted in Figure 2.15.

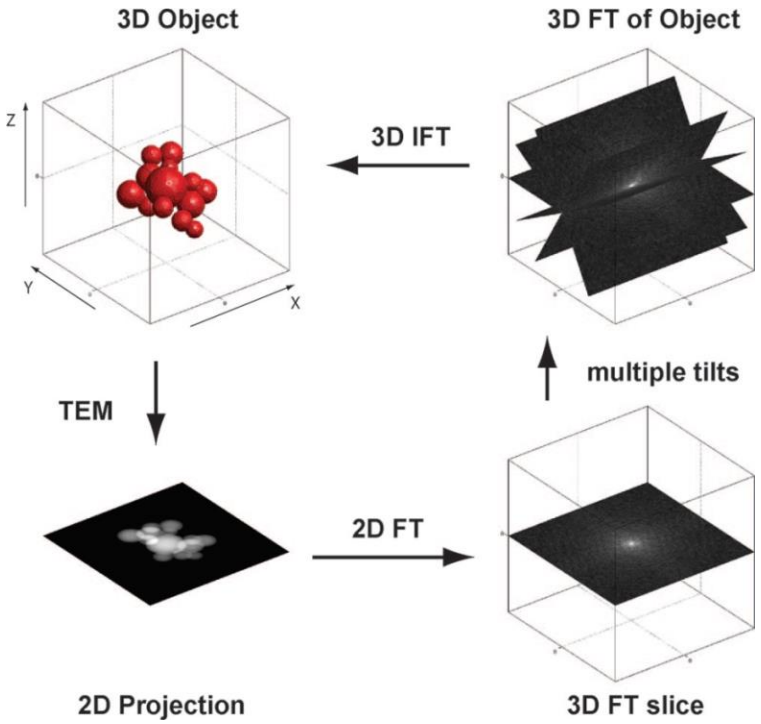

Figure 2.15: Schematic representation of a tomographic reconstruction in Fourier space: 1) acquisition of projection images, 2) Fourier transform, 3) combination of Fourier transform at different tilt-angles, and 4) inverse Fourier transform to reconstruction original shape.[68]

The projections of TEM tomography will results in a high sampling density at low spatial frequencies and low sampling at high spatial frequencies (Figure 2.16a). This will result in a blurry reconstruction in real space due to the over-sampling of the low-frequency components. To improve the blurry reconstruction, a weighting filter can be applied to balance the sampling in the Fourier domain, and the modified algorithm is known as weighted back-projection (WBP).[151] This weighting filter is a radial linear function in Fourier space, zero at the center and a maximum at the edge.[152] In order to reduce high-frequency noise introduced by the (discrete) inverse Fourier transform, the high-frequency information is often dampened by the weighting filter with a high-frequency cut-off.[153] In addition, the discrete number of acquired projections results in the effect of discarding 'zero-frequency' information over a finite range of frequencies and thus always lead to an offset between original and reconstructed intensities. Therefore, due to the discrete number of acquired projections as well as the imperfect weighting filter, reconstructions using WBP always contains artifacts that complicates the interpretation of the tomograms.

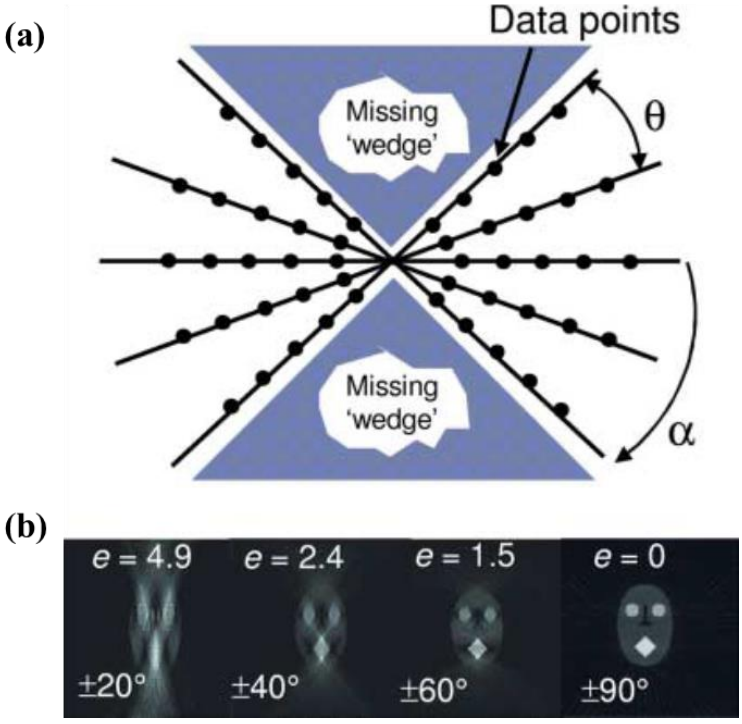

Figure 2.16: Representation of Fourier space sampled in the limited angle showing the relatively small number of data points at high frequencies, which results in a blurred reconstruction and the missing wedge of information that leads to an elongation *e*. The angular sampling is θ and the maximum tilt angle is α.[152]

In practical TEM tomography, the limited space between the objective lens pole pieces and the finite thickness of the specimen holder typically limits the tilt range available in the microscope, giving rise to the 'missing wedge' of information (Figure 2.16a). This leads to a reduced resolution in the direction parallel to the optic axis (*dz*), which is typically described by an elongation factor *e* (example are shown in Figure 2.16b) related to the maximum tilt angle α:[154]

$$dz = e * dy, e = \sqrt{\frac{\alpha + sin\alpha * cos\alpha}{\alpha - sin\alpha * cos\alpha}} \qquad (2\text{-}17)$$

This blurring of reconstruction in the z-direction degrades the quality of the resulting reconstruction, as shown in Figure 2.16b. In practical, the missing wedge results in a fluctuation of the background intensity around the object and also influence the intensity of features within the reconstruction.[155] This will lead to the missing of some smaller features or vary the boundaries of adjacent features when the reconstruction segmented by a threshold.

Iterative reconstructions

One approach to improve the 3D reconstruction is to refine the reconstruction by minimizing the difference between the experimental projections and the ones reprojected from the initially reconstructed tomogram. The differences between the original projections and the reprojections can be back-projected into the reconstructed volume, and finally either used to modify the initial reconstruction or to generate a difference reconstruction. This process is the repeated iteratively. The basic form of an iterative reconstruction is the algebraic reconstruction technique (ART)[156], where the reprojected image from the current reconstruction is compared with an experimental projection at a certain tilt angle and the difference is used to correct the reconstruction. The updated reconstruction is used in the next tilt angle. Even though ART can yield significant improvements in the reconstruction compared to WBP, it tends to be unstable in the presence of noise. A more robust approach is a comparison of all projections simultaneously to generate a difference volume during each iteration.[157] The implementation of this simultaneous iterative reconstruction technique (SIRT) is schematically illustrated in Figure 2.17. The main consideration for such a loop in practice is the number of iterations (N) and whether an additive or multiplicative correction is applied. The number of iterations for SIRT is usually chosen by a subjective 'good-enough' principle[157], as the improvement in the reconstruction tends to be minimal after 20-25 iterations. Moreover, the SIRT algorithm has been found to perform well in the presence of noise. A demonstration of the differences in the reconstruction quality between SIRT, ART and WBP is shown in Figure 2.18 for a test dataset with different noise levels. Because of these characteristics, SIRT has become the standard algorithm in most reconstruction software and is widely used to generate 3D reconstruction data for a number of different materials. However, the SIRT reconstruction still suffers from artifacts (e.g., blurring, elongation, "fan" or "star" artifacts), which arise from the limited number of projections due to a maximum tilt angle (typically ~70°). Such artifacts often influence the segmentation of components in the reconstruction and quantification of this data.

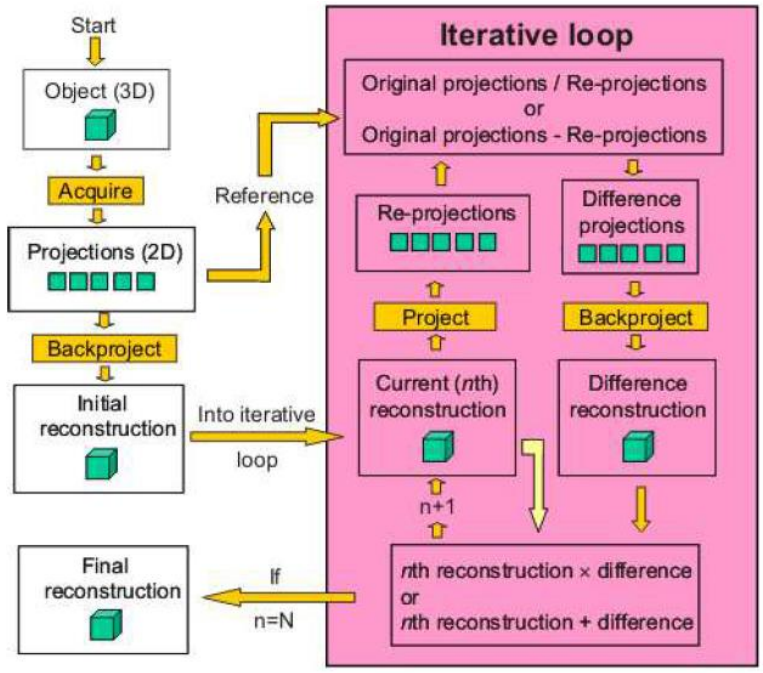

Figure 2.17: The flow chart of SIRT, illustrating implementation of iterative reconstruction for N iterations where n is the current iteration and it starts from n=0.[136]

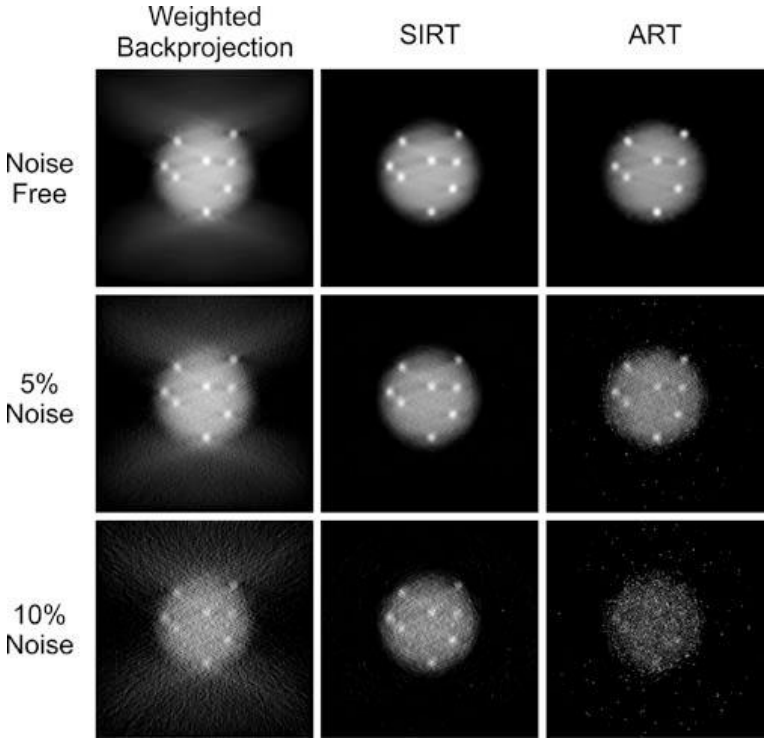

Figure 2.18: Tomographic reconstructions from a test object with WBP, ART and SIRT algorithms, where the WBP demonstrates classical "fan" artifacts due to the missing wedge and SIRT proves more robust in the presence of noise compared to ART.[145]

Advanced 3D reconstruction algorithms

A major drawback of the conventional reconstruction algorithms (WBP, ART and SIRT) mentioned above is the requirement of a large number of projections to obtain reasonable quality

reconstructions. The geometry of the microscope and the electron beam stability of the sample often limit the number of projections that can be acquired. Recently, some advanced reconstruction algorithms that can yield higher quality reconstructions with a reduced number of projections have drawn a lot of attention.[158–160]

DART is an iterative reconstruction algorithm that incorporates prior knowledge about the object. The most critical knowledge is that the object only consists of a few defined components.[160] This prior knowledge of the discrete of the sample is implemented by combining a iterative reconstruction algorithm (such as ART, SIRT) with discretization steps. The algorithm starts from a SIRT reconstruction to obtain information on the gray levels in the reconstructed object. Then a threshold is applied to segment the reconstruction into a few distinct gray levels, corresponding to the components in the sample. The boundary pixels are detected from the segmented reconstruction, which are all the pixels that have at least one neighboring pixel in a different segmentation class. Afterwards, the boundary pixels are reconstructed in another iteration, while non-boundary pixels remain fixed. In this way, the number of uncertain pixels is strongly reduced and the accuracy of the boundary is improved. For the next iteration, the boundary pixels are determined again and the process is repeated resulting in an improved reconstruction with increasing iterations, which is directly segmented corresponding to the different materials classes defined at the beginning. The flow chart of the basic steps performed in the DART algorithm is illustrated in Figure 2.19.

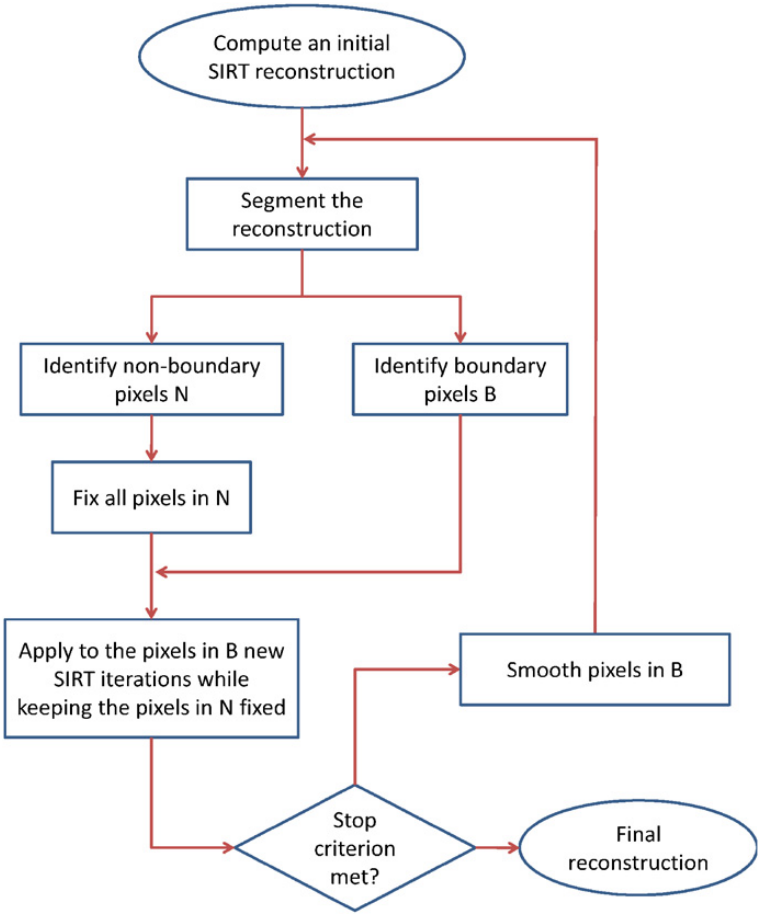

Figure 2.19: Flow chart of the DART algorithm.[160]

With the iterative refinement of the boundary voxels and the incorporated prior knowledge that the sample only consists of a limited number of discrete materials with discrete gray levels, the number of unknown parameters in the reconstruction is drastically reduced and the DART algorithm can effectively reduce the missing wedge artifacts without the need of improved data acquisition.[160] Therefore, the technique is particularly powerful for a quantitative analysis of the reconstruction compared to a SIRT reconstruction.[161–163] However, it should be noted that the sample must be discrete and the gray levels have to be estimated from the SIRT reconstruction. This is an important restriction for the practical use of DART.

Other advanced algorithms[159,164–166] derived from compressive sensing (CS)[167] are exploited increasingly in electron tomography reconstruction. These CS-based algorithms can markedly reduce artefacts such as streaking, blurring of object boundaries and elongation of reconstruction presented in conventional reconstructions, even with fewer projections. Therefore, the CS-based approaches enable more reliable quantitative analysis of the reconstructions as well as novel 3D studies from extremely limited data. For example, Saghi et al. demonstrated that the compressed sensing-electron tomography (CS-ET) algorithm yielded more straightforward and objective segmentation in the 3D study of concave iron oxide NPs.[159] With different numbers of projected images, the volume of the concavity measured from CS-ET reconstructions is remarkably consistent compared to SIRT reconstructions.

2.3. Electron tomography in practice

Electron tomography in practice usually consists of a number of steps, including acquisition, alignment, reconstruction, visualization and segmentation, as shown in Figure 2.20. These steps are discussed hereinafter for their importance and the influences in quality of resolving the 3D structure.

Figure 2.20: The main steps of electron tomography.

2.3.1. Acquisition

The projection requirement

As defined by the Radon transform (Equation 2.14), the ideal projection is a summation of line integrals through the object. To be suitable for tomographic reconstruction a transmitted signal must meet the 'projection requirement' that the detected projected signal must be a monotonically varying quantity representing some physical quantity of the structure (*e.g.* thickness, density, magnetic or electronic properties of materials),[168] which can be linearly summed in projection. BF-TEM and HAADF-STEM are the most frequently used imaging modes for tomographic acquisition. As discussed in section 2.1.1, compared to BF-TEM, the intensity of HAADF-STEM imaging has an approximate monotonic relationship between intensity and sample thickness, whereas the exponential decay of the

image intensity with mass-thickness BF-TEM has to be linearized working with the logarithm of the images. Furthermore, the scanning nature of STEM enables the possibility of dynamic focusing that allows to maintain uniform defocus conditions across a tilted specimen. HAADF-STEM mode has been shown to be a powerful and versatile imaging mode for a lot of materials related to the physical sciences.[70,107,134,135] Therefore, the electron tomography work for the supported catalysts in this thesis has primarily relied on HAADF-STEM imaging.

Acquisition geometry

In order to generate a number of projections of the region of interest, the sample must be tilted or rotated with respect to the electron beam. Single tilt axis acquisition, by tilting the specimen about a single axis, is most commonly used to acquire the different projections. The highest achievable tilt angle depends on the size of the holder and the space of pole piece. For example, a standard FEI double tilt holder (Figure 2.21a) cannot be tilted higher than $\pm 40^{o}$ in a super twin lens. In order to increase the tilt-range, dedicated high-tilt tomography holders with a narrower tip as illustrated in Figure 2.21b are used to reach the highest tilt range of approximately $\pm 80^{o}$. However, this tilt maximum still does not reach the full angular range of $\pm 90^{o}$ due to a shadowing effect of the holder and leads to 'missing wedge' of information, as already shown in Figure 2.16a. An alternative way of reducing the missing wedge is to record a second tilt series about an axis perpendicular to the first one and this is called dual-tilt axis acquisition.[169] Practically, the dual-tilt axis acquisition is more difficult to operate and so far there is not good solutions for dual-axis alignment. Recently, tomography holders have been developed to support a rod-like or needle sample and allow for a full range of tilt angles.[170] The possibility of acquiring a full range tilt-series eliminates missing wedge artifacts and significantly enhances the quality of reconstruction, therefore greatly improving the quantitative prospects of electron tomography. However, the technique remains less popular as the sample preparation is time-consuming and it can only investigate a small volume.

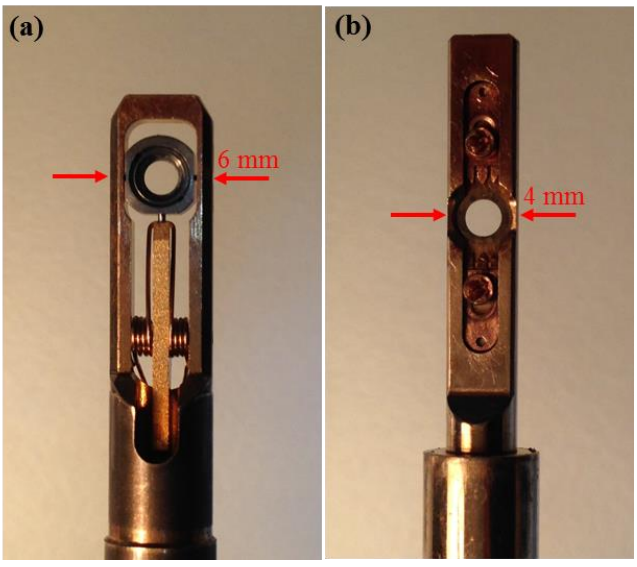

Figure 2.21: (a) A regular FEI double-tilt holder with 6 mm tip size and (b) Fischione model 2020 single tilt tomography holder with 4 mm tip size.

Acquisition in practice

The acquisition of a tilt series consists of a repeating set of steps: tilting of the specimen, repositioning of the sample within the field of view and focusing of the image, which can be performed manually. However, significant advances have been made in automation to ease the acquisition process. In this thesis, the "Xplore3D Suite" from FEI Company was used for the automated tomographic acquisition around a single tilt axis. The specimen is positioned at the eucentric height beforehand to minimize sample movement during tilting. There are always small shifts of images in the successive acquisition and therefore a cross correlation method is applied to measure the sample shift and then compensate this by an image shift. Focusing during acquisition in TEM and STEM modes is different. Typically, a sufficiently large defocus is introduced to enhance the image contrast in TEM mode before acquisition and the focus of the specimen is then adjusted during acquisition. But the problem of the lack of uniform focus may arise when the specimen is tilted to high angles, where different regions of the specimen have different focusing values, resulting in an image with blurred contrast. This problem can be reduced using a dynamic focus option in STEM imaging mode, where the inherent scanning of STEM allows optimizing the focus values for each raster line. Moreover, the focusing procedure implemented in the automated acquisition at STEM mode uses several images acquired at different focus values and the contrast in each image is measured according to the sharpness of image features. The image showing the best sharpness features is selected as the optimal focus image for current tilt angle. After the acquisition, the sample is tilted to the next tilt angle and the previous steps are repeated.

2.3.2. Alignment

Because any misalignment between successive images leads to artifacts or the attenuation of high-frequency information,[171] an accurate alignment procedure for all acquired tilt-series images is very important to ensure a reliable reconstruction. As an example, in Figure 2.22 it is illustrate that an inaccurate estimate of the tilt axis leads to a blurred signal in the reconstructed object and causes a banana shape artifacts.[107] Cross-correlation is a simple method to align successive images in a tilt-series, measuring the displacement from the position of the maximum in the cross-correlation image (Figure 2.23). The cross-correlation accuracy and robustness can be in general improved by the application of filters, especially low- and high-pass filters, to the projections. Alignment by cross-correlation is usually successively applied across the whole tilt-series. However, the sequential cross-correlation may build up errors over the tilt-series because of small, sub-pixel, misalignments between each of the projections. In addition, the tilt-angle of projections approximately identified in the acquisition process is impossible to be refined by this cross-correlation, which will result in smearing artefacts in reconstruction. Magnification variation, image rotation and distortions of tilt-series cannot also be corrected with the cross-correlation. Especially for the thick object, the projections at different angles cannot correlate well by the cross-correlation because features at different height within the sample move in different ways in the projections, leading to larger alignment errors.

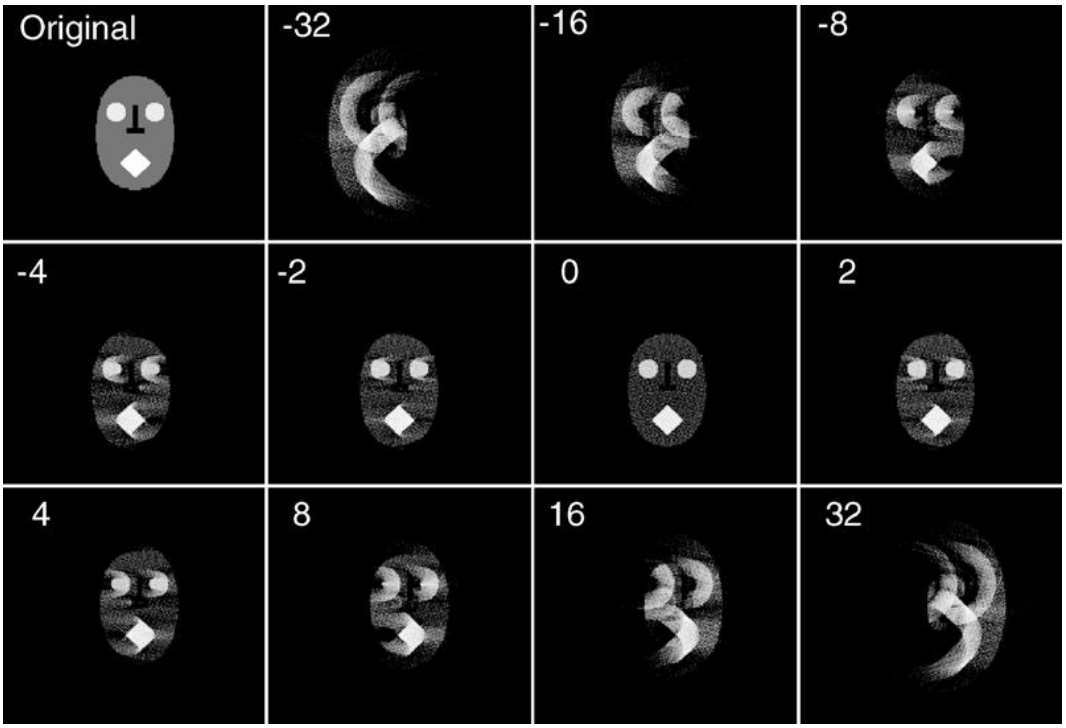

Figure 2.22: Demonstration of the effects of misalignment of the tilt axis on a reconstruction of the head phantom with a 64 pixels wide. The number in images indicates the pixel misalignment, perpendicular to the tilt axis.[107]

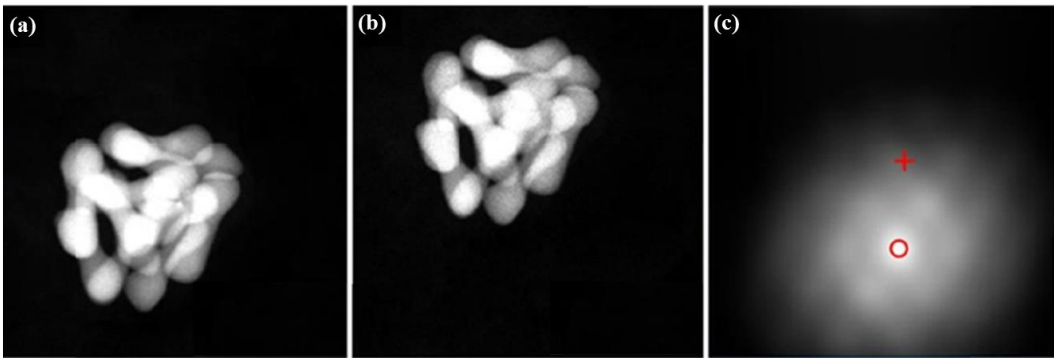

Figure 2.23: The position of the maximum intensity in the cross correlation image (c) of two successive projection images (a) and (b) of Au dumbbells shows the relative shift between them.[172]

The fiducial marker-based procedure is another widely used method for alignment of tilt-series.[173] In this approach, small spherical 'fiducial markers' (often gold beads) are added to the specimen.[15] Typically, 20-30 markers are selected and the positions of these markers tracked throughout the tilt-series. With the initial tilt-series alignment, assuming that the markers move on a line perpendicular to the tilt-axis following a rigid body rotation, the 3D position of each marker is estimated and used to predict the 2D projected positions of this marker in all views of the tilt-series. The alignment of the tilt-series is refined to minimize the difference between the experimentally marked and the calculated projection positions of the markers. This process is iteratively repeated to refine the alignment. In this refinement process, it is also possible to compensate for image distortions, tilt-angle or magnification variations to take these artefacts explicitly into account. Therefore, the fiducial marker-based alignment procedure is superior to the cross-correlation for obtaining an accurate alignment of the projected

images. In this thesis, the fiducial marker-based method has been primarily employed for alignment of tilt-series images. Either additional gold beads or the supported NPs of the actual catalyst were used as 'fiducial markers'.

2.3.3. Visualization

The tomographic reconstruction is not the ultimate task of the process as shown in Figure 2.20. Visualization is an important step towards interpreting the reconstructed 3D volume, which is critical for successful extraction of useful information of 3D structures. One of the simplest treatments for visualization are 'orthoslices' produced by digitally slicing the data to examine a 2D slices from the 3D dataset. The intensity in the orthoslices represents the physical value (often the density) of a voxel in the 3D structure.

Volume rendering or voxel projection is a very intuitive visualization method that is a directional summation of the 3D dataset at any arbitrary angle, which is analogous to the original projection operation in the microscope. The advantage of this approach is that features of interest within the reconstruction can be emphasized by setting voxels with different intensity ranges, to a specific optical characteristic such as luminance, color or transparency. This method is preferred for visualization of internal and external structures and any subtle variations in the object density. Surface rendering, on the other hand, computes a triangular approximation of the interfaces between different components in reconstruction volume, which has to be segmented beforehand.[174] This process reduces the volume data to a set of polygonal surfaces that can be rotated and visualized from any angle and subjected to a variety of light sources, further improving the 3D effect.

2.3.4. Segmentation

Apart from tuning the visualization, quantitative analysis of the 3D structure relies on precise segmentation, which is also the most challenging part in the analysis of tomographic reconstructions. In a simple thresholding for segmentation, each voxel, depending on its gray level in the reconstructed tomogram, is assigned to a specific feature or composition that represents the original object. This thresholding requires well-separated intensity values across the whole region of interest and a high signal-to-noise ratio. However, in practice, such well-separated intensity are rarely achieved due to reconstruction and imaging artifacts and therefore the method locally over/underestimates the features. Alternatively, manual segmentation is another approach, where the features in a 3D reconstruction are determined by a person defining voxels belonging to specific features of interest in each slice. However, this process is very time-consuming, labor intensive and usually subjective. Some groups have developed more advanced segmentation approaches based on an evaluation of the voxel intensities[175], interconnectedness[176] or sharp gradients[177] within reconstructions. However, none has seen wide application in electron tomography because the segmentation approach is typically for dedicated types of structures and would need to be redesigned on a case-by-case basis. In the thesis, the image processing is firstly applied to reduce noise or/and to enhance local contrast of components in the

reconstruction and then the thresholding is to segment the processed reconstruction for further quantitative analysis.

2.3.5. Morphological quantification of the pore structure

Skeleton analysis

The pore volume extracted from the segmented data was analyzed using the skeletonization function in Amira 6.0 (FEI Company) to quantify the geometry and topology of the pore structure. The skeletonization procedure reduces the pore space to a branch-node network (i.e., skeleton) as described by Fouard et al.[178] while both the geometrical and topological information are preserved. A scheme of the skeletonization process is shown in Figure 2.24. There are two keys procedures in this process: i) the distance map to calculate the distance of each voxel to the nearest boundary, which is needed on the one hand to guide the thinning procedure and on the other hand to provide an estimate of the thickness (radius) of the pore space; ii) the thinning is an iterative erosion procedure removing voxel by voxel starting from the boundary voxel until only a string of connected voxels remains. After the skeletonization process, the media axis of pore structure, i.e. the network of the skeleton, is derived, where information including the radius at each voxel of the skeleton, start/end points of individual pores and the number of voxels along the skeleton are recorded. Afterwards, the mean diameter of each individual pore was calculated as average diameter of each voxel within the skeleton and the pore length was obtained from the number of voxels along the skeleton. The pore coordination number was also determined by counting the number of individual branches connected a common point.

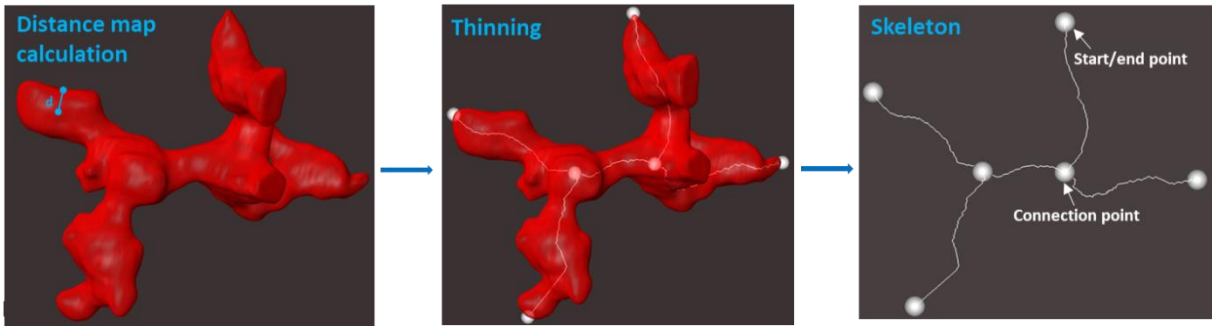

Figure 2.24: Scheme of the skeletonization process: distance map calculation, thinning and the derived skeleton (left to right).

The tortuosity of the pores was estimated from the skeletonized data using a home-made code in MATLAB. The tortuosity (τ) of each individual branch is defined as the ratio of the pore length (d_l) and the Euclidean distance ($d_{eucl.}$) between start and end points of the pore:

$$\tau = d_l / d_{eucl.} \qquad (2\text{-}18)$$

Chord length distribution (CLD) analysis

CLD analysis is used to describe geometry of the disordered pore structure of the investigated mesoporous carbons, which has been performed by my collaborator, Artur Svidrytski at the Philipps-

Universität Marburg. Random points were generated in the void (pore) space of the image stack. From each point, 26 vectors were projected in angularly equispaced directions until the vectors either hit a boundary to the solid phase or projected out of the image region; chords pointing out of the image were discarded. Points of origin were generated until a total of 10^7 chords were collected for each image stack. The lengths of resulting chords was estimated from the sum of the absolute lengths of pairs of opposing vectors. The collected chord lengths were binned using the size of 1 nm to generate the CLD histogram of the pore space, which was fitted with a *k*-gamma function:[179]

$$f(l_c) = \frac{k^k}{\Gamma(k)} \frac{{l_c}^{k-1}}{\mu^k} \exp\left(-k\frac{l_c}{\mu}\right) \quad (2\text{-}19)$$

where l_c denotes the chord length, Γ is the gamma function, μ is the first statistical moment of the distribution, and k is a second-moment parameter defined by the mean and the standard deviation σ as $k = (\mu^2/\sigma^2)$. The values for μ and k derived from the *k*-Gamma function fitting of CLD represent the average pore size and for the homogeneity of the pore volume distribution, respectively.[179–181]

2.3.6. Pore-scale diffusion simulation

A cubic domain with a size of up to 220x220x220 voxels was cropped from the pore volume for the pore-scale simulations of diffusive transport in each reconstruction, which had also been done by Artur Svidrytski in Philipps-Universität Marburg. The random-walk particle-tracking (RWPT) technique was used to simulate for diffusion in the void (pore) space of the cubic domains.[182] A large number (10^7) of passive, point-like tracer particles was randomly distributed in the void space. In the random diffusion motion, the displacement $\Delta\mathbf{r}$ of every tracer in each time step Δt of the simulation was calculated as

$$\Delta\mathbf{r} = \boldsymbol{\gamma}\sqrt{6D_{bulk}\Delta t} \quad (2\text{-}20)$$

where D_{bulk} is the tracer diffusion coefficient in the open space and $\boldsymbol{\gamma}$ is a vector with random orientation in space and a length governed by a Gaussian distribution with zero mean and unity standard deviation. The value of Δt was adjusted such that the mean diffusive displacement did not exceed $\frac{\Delta h}{10}$ (where $\Delta h = 0.32$ nm is the voxel size of reconstruction). To restrict diffusion to the void space, a multiple-rejection boundary condition was implemented at the solid–void interface: If at the current iteration step a tracer crossed the solid–void interface, this displacement was rejected and recalculated until the tracer position was in the void space. At the external faces of the cubic domain, mirror boundary conditions were imposed: when a tracer hit an external face, it was mirror-reflected from that face, but the total length of the displacement (with reflection) was equal to $\Delta\mathbf{r}$. During the simulation, the displacements of every tracer in x-, y-, and z-direction was monitored, which was used to determine the time-dependent diffusion coefficients along each direction j according to[183]

$$D_j(t) = \frac{1}{2N}\frac{d}{dt}\sum_{i=1}^{N}\left[\Delta r_{ij}(t)\right]^2 \quad (2\text{-}21)$$

where j denotes x, y, or z, and $\Delta r_{ij}(t)$ are the accumulated displacement of the i^{th} tracer along direction j after time t. A decrease of $\frac{D_j(t)}{D_{bulk}}$ with time (i.e., the number of iterations) from the initial value of 1 results from interactions of tracers with the solid phase. In the beginning, only a small fraction of the tracers experiences geometric confinement during their random walk. With increasing time, the transient diffusion coefficients asymptotically approach the sought values.

3. Quantifying morphology and diffusion properties of mesoporous carbon from high fidelity 3D reconstructions

3.1. Introduction

Porous materials have long been deemed to be a good support for the active nanometer-size metal particles in heterogeneous catalysis.[31,184] As introduced in chapter 1, the catalytic performance strongly depends on the pore morphology, which is controlling diffusion of reactants and products, confines the reaction geometry and influences migration of NPs. Electron tomography has been extensively used to characterize the 3D pore structure of ordered porous support and demonstrated to provide quantifiable 3D structural information at the nanoscale.[185–188] However, the measured/calculated properties of the investigated material highly rely on the fidelity of the segmented 3D reconstruction, which has been limitedly addressed much so far. Moreover, investigation of disordered pore structures providing quantitative information on their geometry and topology are still very limited. In this chapter, the 3D structure of a disordered mesoporous carbon, commonly used as support in heterogeneous catalysis, is elucidated by combined electron tomography with advanced image analysis. The fidelity of the segmented 3D object obtained by image processing of a SIRT and a DART reconstruction is investigated using both experimental data and realistic phantoms for the material. Moreover, the influence of the two reconstruction approaches on the pore morphology is investigated in terms of pore size, pore length, tortuosity and connectivity. Most important, the effect of variations introduced in reconstruction and segmentation process is evaluated on the diffusion properties calculated from the support structure, which is one of the critical properties of the mesoporous material for catalysis.

3.2. Materials and experimental methods

3.2.1. Synthesis of mesoporous carbon

The mesoporous carbon had been synthesized by Dr. Alberto Villa at University of Milano. The same amount (17.6 g) of Resorcinol and Pluronic F127 were dissolved in a mixed solution of ethanol (72 mL)/water (54 mL)/HCl (17.6 mL, 12.5M). Formaldehyde (20.8 mL) was subsequently added. After 6 min, a phase separation was observed. The gel was stirred for another 60 min. The top liquid phase was separated and the bottom gel polymer was cast on Mylar. The film dried overnight at room temperature and then at 80 $^{\circ}$ C for 24 h. The resulting polymer composite was heated to 850 $^{\circ}$ C (the heating rate of 5 $^{\circ}$ C/min) to carbonize for 120 min under Ar flowing (500 mL/min). The synthesized material has a specific surface area of 589 m^2/g with an average pore diameter of 6.9 nm according to using the Brunauer Emmett Teller (BET)[189] analysis, similar to the support material in previous heterogeneous catalysis studies[190].

3.2.2. Electron tomography data acquisition

A small amount (~5 µL) of colloidal Au NPs (6.5 nm diameter, provided by the University Utrecht) in suspension was dropped on a 100x400 mesh carbon coated copper grid (Quantifoil) and then residual solvent was removed from the grid. After the solvent evaporated at room temperature, the powder of mesoporous carbon was directly dispersed on the prepared copper grid. Electron tomography was performed using a Fischione 2020 tomography holder in a Titan 80-300 microscope (FEI Company) operated at 300 kV in STEM mode with a nominal beam diameter of 0.27 nm. STEM images were acquired with a HAADF detector using the Xplore3D software (FEI Company) over a tilt range of ±76° with a tilt increment of 2°. Alignment of the tilt series was performed in IMOD[191] using the Au NPs as fiducial markers and achieved a mean residual error of 0.44 pixels.

3.2.3. Reconstruction and segmentation

The aligned tilt series was reconstructed using SIRT implemented in Inspect3D 3.0 (FEI Company). Because of noise and because the reconstructed intensity of different components also depend on the local environment, the reconstructed tomogram was processed prior to segmenting the 3D volume for further quantitative analysis. The image processing reduced noise and resulted in better separated intensities for each component, while preserving sharp boundaries between components. This was performed using plugins in the Fiji software package[192] with following steps: i) noise reduction of the image stack using the PureDenoise plugin[193] and the anisotropic diffusion filter[194]; ii) enhancement of local contrast using the CLAHE plugin;[195] iii) binarization by global thresholding, where the threshold was determined by manual to represent most of the pore features in the reconstruction. The generated binary 3D volume (labelled as segmented-SIRT) was further separated into three parts: vacuum, internal pore and carbon using the pore filling approach implemented in Amira 6.0 (FEI Company). Figure 3.1 illustrates the full image processing steps. In addition, the aligned tilt series was reconstructed using the DART implementation in the TomoJ plugin[196] in Fiji, which yielded a segmented 3D reconstruction (labelled as DART). The resulted reconstructions had a final voxel size of 0.32 nm.

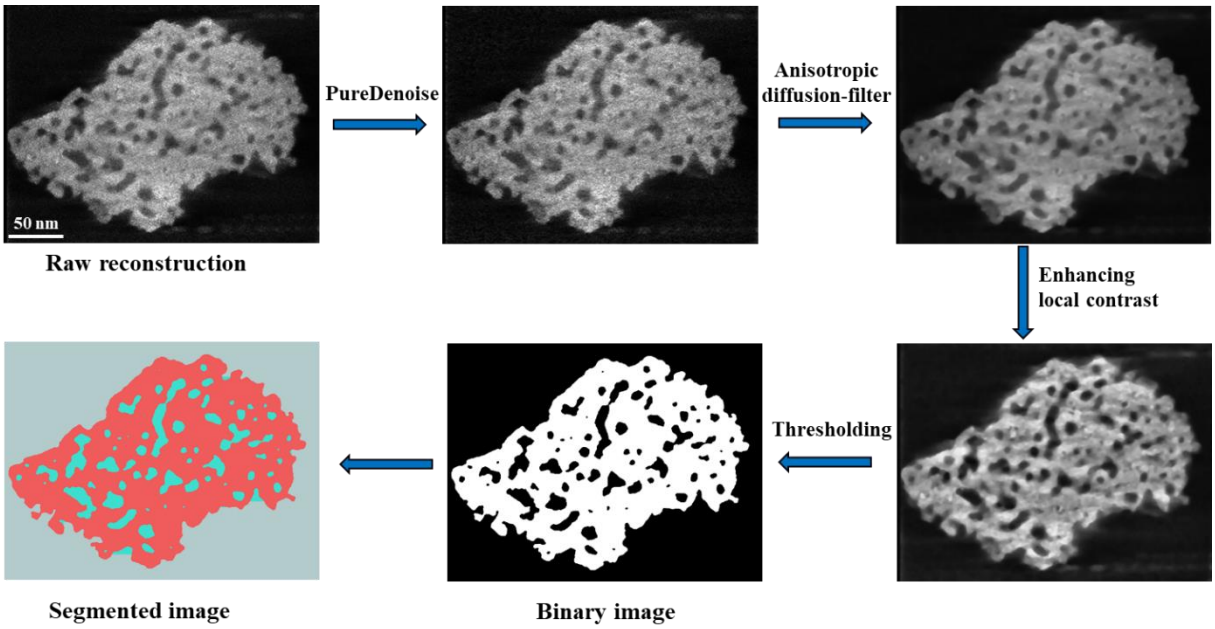

Figure 3.1: Illustration of the image processing steps after SIRT reconstruction for the mesoporous carbon.

3.2.4. Validation of experimental reconstruction and segmentation

Tilt-series of 2D projections covering the angular range of 90° in 2° increments were created using MATLAB based on the 3D volume of the segmented-SIRT and DART reconstruction. To validate the experimental reconstruction and segmentation, the mean absolute error (MAE)[197] approach was used to estimate the difference between the experimental tilt-series and the re-projected segmented images within the ±76° tilt-range of the experimental data. To compare the two projected images for the MAE calculation, the gold markers within the experimental tilt-series images were removed by interpolating the image intensities in the corresponding areas using IMOD and the complete tilt-series of projected images was scaled to cover the full 8-bit intensity range of 0-255 with the intensity of the vacuum regions set to 0.

3.2.5. Phantom study

To evaluate the fidelity of the reconstruction and segmentation approaches in more detail, the DART reconstruction was used as a phantom to generate the re-projected tilt-series in the angular range of ±76° and ±90° with a tilt step of 2°. The generated tilt-series data were reconstructed with the same procedure of SIRT and DART reconstruction used for the experimental data, resulting in 3D reconstructions are labeled as *Phantom.*segmented-SIRT and *Phantom.*DART. Afterwards, these phantom reconstructions were quantitatively compared with the initial phantom for evaluating any differences on a voxel level as well as in the mesopore morphological description and the diffusion simulations.

3.3. Quantitative comparison of the morphological information obtained from experimental SIRT and DART reconstructions

A STEM image from the tilt-series (Figure 3.2a) gives some idea of the disordered morphology of the investigated mesoporous carbon. After 3D reconstruction, the internal mesopore structure is better revealed with the irregular shape and non-uniform size visible in the slice (Figure 3.2b). Segmenting the 3D reconstruction is an indispensable step to provide any quantitative 3D structural information. As indicated in section 3.2.3, the SIRT reconstruction and the DART reconstruction were segmented to provide quantification information on the morphology of the investigated material. Figure 3.2c and d show the segmented 2D slices of the segmented-SIRT and the DART reconstruction. Visually, most of the features are presented in the segmented slices compared to the initial SIRT reconstruction slice (Figure 3.2b). However, when looking closely at the highlighted regions, there are still differences in the size (red circles) and 2D connectivity (blue circles) of some pores, indicating imperfections in the segmentation. To evaluate the fidelity of the segmented reconstructions, the re-projection tilt-series generated from the segmented-SIRT and DART reconstruction are compared with the experimental tilt-series (Figure 3.3). The difference between the experimental projections and the re-projections were estimated by MAE calculation, where the MAE was calculated for the nine re-projection directions shown in Figure 3.3d. The result indicates that the MAE values of the segmented-SIRT reconstruction are slightly larger than the DART reconstruction. However, it is hard to tell which reconstruction is better from the MAE calculation because the differences are so small.

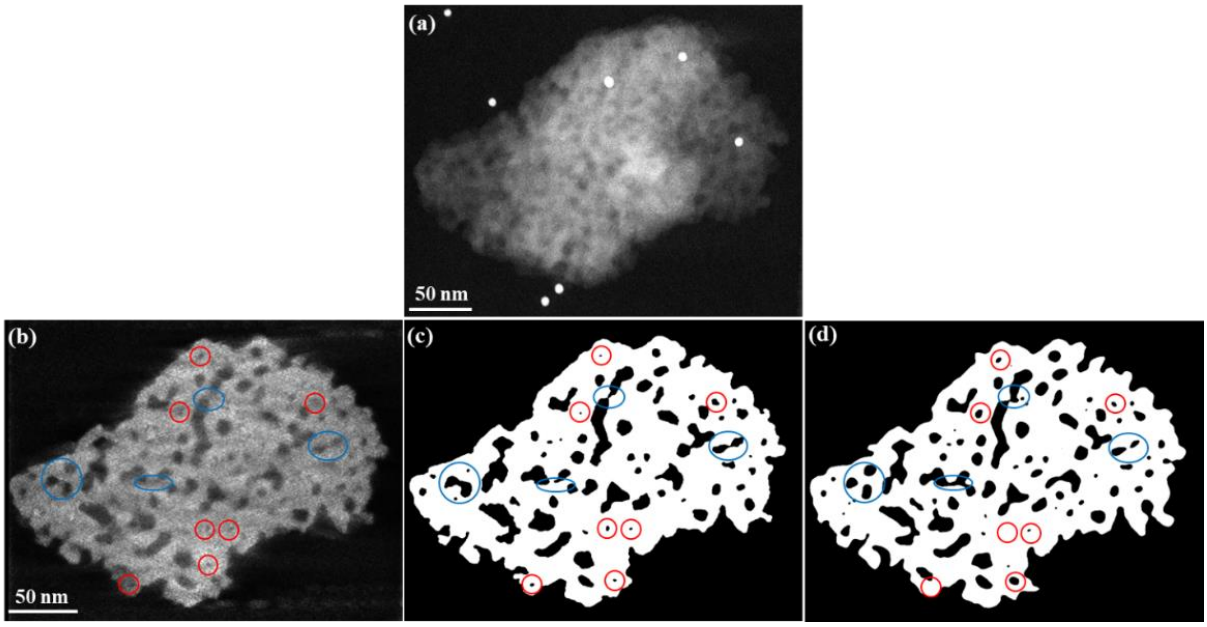

Figure 3.2: (a) HAADF-STEM image at 0° from the tilt-series of a disordered mesoporous carbon (the white particles are the added gold markers); Typical slice of (b) the SIRT reconstruction, (c) the segmented-SIRT and (d) the DART reconstruction (the areas highlighted by red cycles exhibit pore size variations and the blue regions indicated differences in connectivity of the pores in 2D).

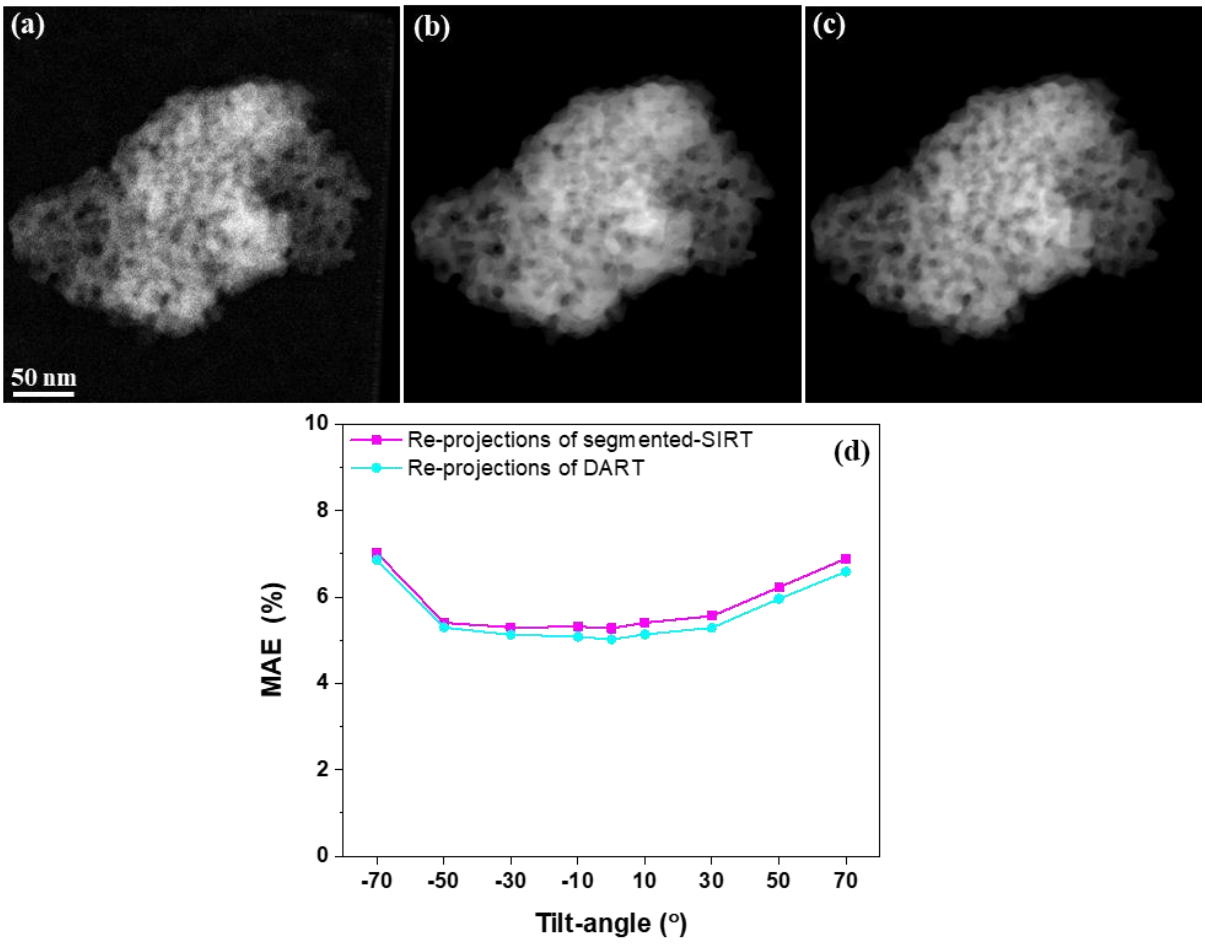

Figure 3.3: Projected images at 0°: (a) experiment STEM tilt-series, (b) segmented-SIRT and (c) DART reconstructions. (d) MAE calculation for re-projected images from the segmented-SIRT (purple) and DART (blue) reconstructions at angles of -70°,-50°,-30°,-10°, 0°, 10°, 30°, 50° and 70°.

The CLD and skeleton analysis were performed to quantify the pore morphology of the segmented reconstructions in terms of geometry and topology. Chords generated from a random point within the pore space are schematically in Figure 3.4a and the resulting chord length distribution for the segmented-SIRT and the DART reconstruction are summarized in Figure 3.4b; the histograms are fitted by a *k*-Gamma function. The resulting distribution of chords as well as the μ and *k* values (Table 3.1) derived from *k*-Gamma fitting of the CLD histograms indicate that the geometry and the homogeneity of the pore space are similar for the segmented-SIRT and the DART reconstruction. Furthermore, the geometry and topology of the pore structure including pore size, pore length, tortuosity and interconnectivity are derived from the skeleton analysis, summarized in Figure 3.5. The pore diameter distribution shows a higher percentage of pores with diameter< 4 nm in the segmented-SIRT reconstruction compared to the DART reconstruction (Figure 3.5a), thereby resulting in a slightly smaller mean pore diameter (Table 3.1). The pore length distribution and the mean pore length are very similar in the two reconstructions (Figure 3.5b), in agreement with the similar mean chord length determined from the CLD analysis. The distribution of pore tortuosity (Figure 3.5c) and the coordination number (Figure 3.5d), two important parameters regarding to topology, are also similar.

Therefore, the CLD and skeleton analysis (Table 3.1) indicate that the overall morphology of the two reconstructions is similar and independent of the reconstruction method. However, it should be noted that the total pore volume of the DART reconstruction differs noticeably (~25%) from the segmented-SIRT reconstruction. This is not seen in the MAE calculations (Figure 3.3d) because the intensities of the experimental projections and the calculated projections were both scaled to cover 8-bit as mentioned in section 3.2.4, thereby compensating for most of the pore volume differences. This difference for the SIRT reconstruction is mainly due to the difficulty of defining a good global threshold. Even after image processing, the intensity of the pore/solid varies noticeable in different parts of the particle and therefore a global threshold for segmentation becomes difficult. The effect of the threshold on the SIRT reconstruction will be discussed more details in the phantom studies.

Table 3.1: Morphological descriptors for the pore structure of the segmented-SIRT and the DART reconstruction.

Data	CLD analysis		Skeleton analysis			
	μ (nm)	k	Pore volume (10^5 nm^3)	Pore diameter (nm)	Pore length (nm)	Tortuosity
segmented-SIRT	11.1	3.13	4.39	5.2±2.6	13.1±11.0	1.17±0.31
DART	10.9	3.10	5.67	5.6±2.1	13.3±10.3	1.15±0.24

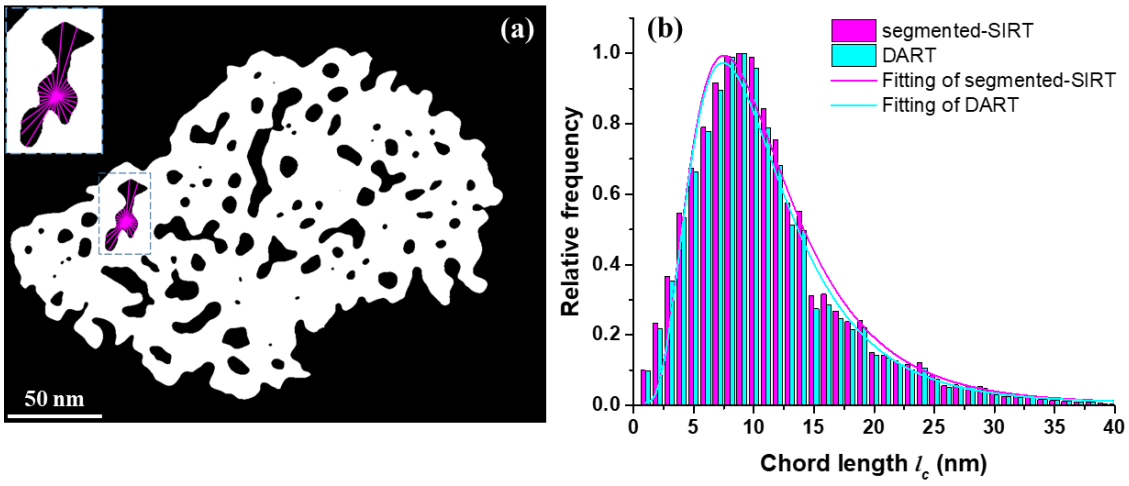

Figure 3.4: Schematic illustration of the CLD analysis of the pore space: chords scanning the solid–void border from a random point in the pore space and (b) chord length (l_c) distribution of the pore space for the segmented-SIRT and the DART reconstruction.

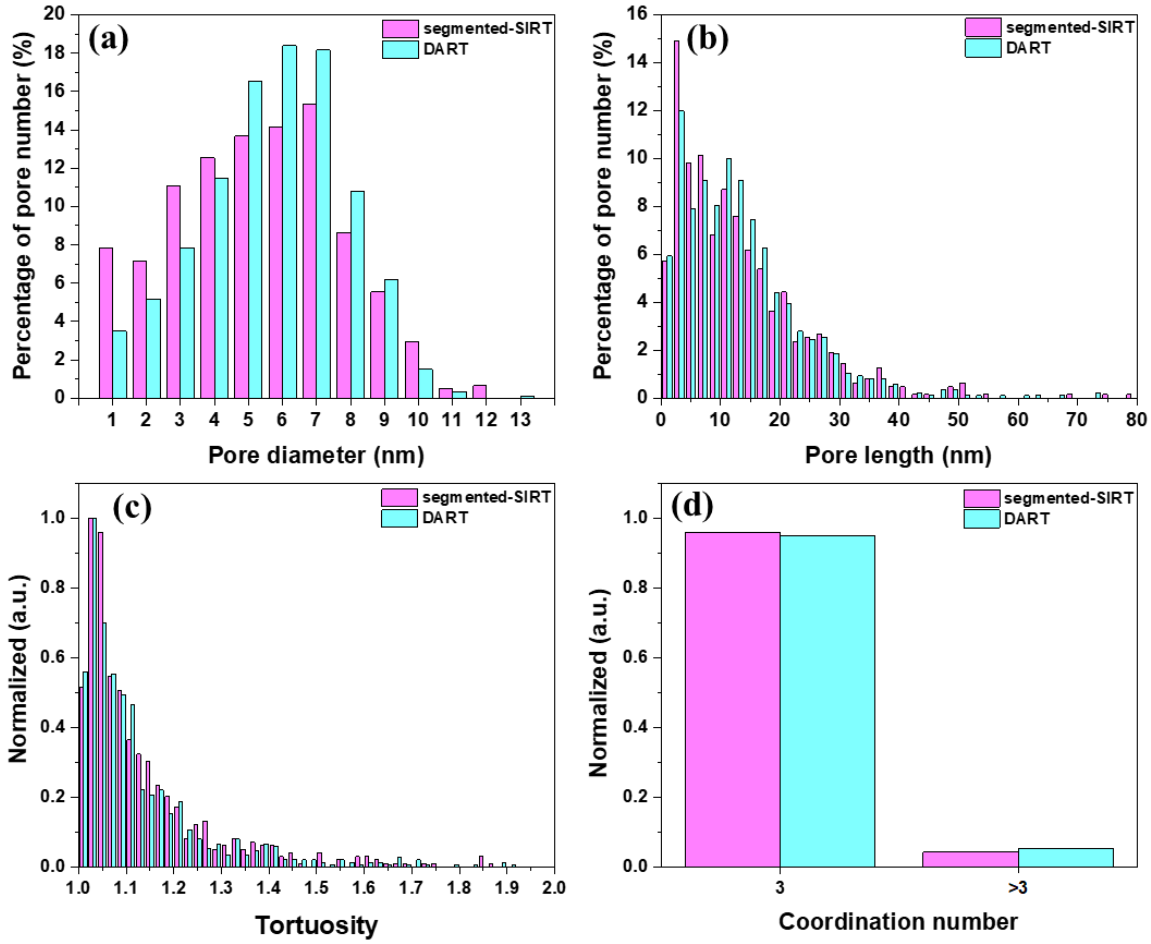

Figure 3.5: (a) Pore size distribution, (b) pore length distribution, (c) pore tortuosity and (d) coordination number based on the segmented-SIRT and the DART reconstruction.

3.4. Diffusion simulations based on experimental segmented-SIRT and DART reconstructions

The pore morphology of the support is confining the diffusion of reactants and products, which is one of the critical aspects to understand activity and selectivity in catalysis.[198–200] To estimate the diffusion properties of the investigated material, taking into account the irregular morphology, the diffusion of this particle was simulated in a cubic volume with a size of up to 220x220x220 voxels (Figure 3.6). This is the largest volume available within the particle, where mirror boundary conditions can be used for the simulation. With increasing box size, the diffusion values become almost stable, indicating that the largest domain is starting to be statistically meaningful considering the local variations within this particle. The diffusion simulation results of the segmented-SIRT and the DART reconstruction are summarized in Figure 3.6c. The effective diffusion (D_{eff}/D_{bulk}) within the largest cubic domain of the DART reconstruction differs noticeably (~51%) from the segmented-SIRT reconstruction, whereas the difference of the pore volume in the biggest box used for the simulations is only 12%. As indicated from the CLD and skeleton analysis, the topology of the pore structure derived from the two reconstructions is similar. Therefore, this significant difference is probably due to the

larger pore volume difference of the segmented-SIRT and the DART reconstruction. The SIRT reconstruction always introduces local and global intensity variations[201,202] and it is therefore difficult to define a global threshold for segmentation even after image processing to enhance the local contrast. In contrast, the DART algorithm[203] starts from a simple thresholded reconstruction, where voxels close to a boundary are iteratively refined to achieve the best agreement between the re-projections from the current segmentation and the experimental projections. This refinement results in the DART reconstruction and thus the DART based diffusion measurements tends to be more accurate. However, it should be noted that in particular DART has a problem detecting small pores of a few voxels, because they are missed in the initial thresholding and might never be close to another boundary. This resulted in a lower percentage of small pores in the DART reconstruction compared to the segmented-SIRT reconstruction, as shown in Figure 3.5a. These imperfections from both SIRT and DART make it difficult to verify the experimentally available data. Moreover, there is not the ground truth to determine the fidelity of the DART based diffusion measurements.

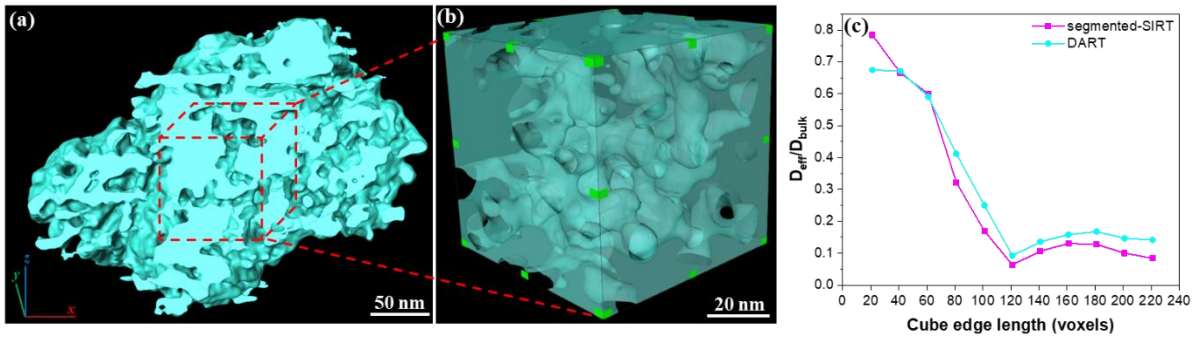

Figure 3.6: (a) Overall 3D morphology of the mesoporous carbon particle, (b) cubic substructure used for the diffusion simulations and (c) calculated effective diffusion (normalized by the bulk diffusion constant) depending on cube edge length for the segmented-SIRT and the DART reconstruction.

3.5. Fidelity of the 3D reconstruction and effect on the morphology and diffusivity

The fidelity of the 3D reconstruction of mesoporous materials and the effects on the calculated properties of this material were investigated using the DART reconstruction as a phantom. This allows to directly quantify differences between the SIRT and DART based reconstructions obtained using the same procedures used for the experimental data. To further evaluate the effect of the missing wedge, the phantom based DART reconstructions were carried out both for tilt-angle ranges of ±76° and ±90°.

As discussed in section 3.3 and 3.4, to evaluate the SIRT reconstruction as well as the DART reconstruction, defining the threshold for the segmentation is very important. Three common unbiased approaches: the isodata-algorithm,[204] moment-preserving[205] and Otsu's[206] thresholds in Fiji were used to define the threshold for the SIRT reconstruction after image processing. The resulting binary slices are shown in Figure 3.7. There are significant differences in the pore features (highlighted by red arrows) in all thresholded cases compared to a visual analysis of the initial SIRT reconstruction.

Instead, a manual threshold was defined for segmentation to best represent most of the features (Figure 3.7b). The threshold of DART reconstruction was estimated from several regions that clearly represent pores or carbon as is commonly done in literature[161,203]. To evaluate the effect of the threshold settings, the variation of the pore volume was investigated by varying the threshold by 10% and 20%. The results are shown in Figure 3.8b and indicate that the pore volume of the segmented SIRT reconstructions is more sensitive to variations of the threshold compared to the DART reconstructions. Experimentally, this means that the SIRT reconstruction will be more difficult to reproducibly threshold compared to the DART reconstruction.

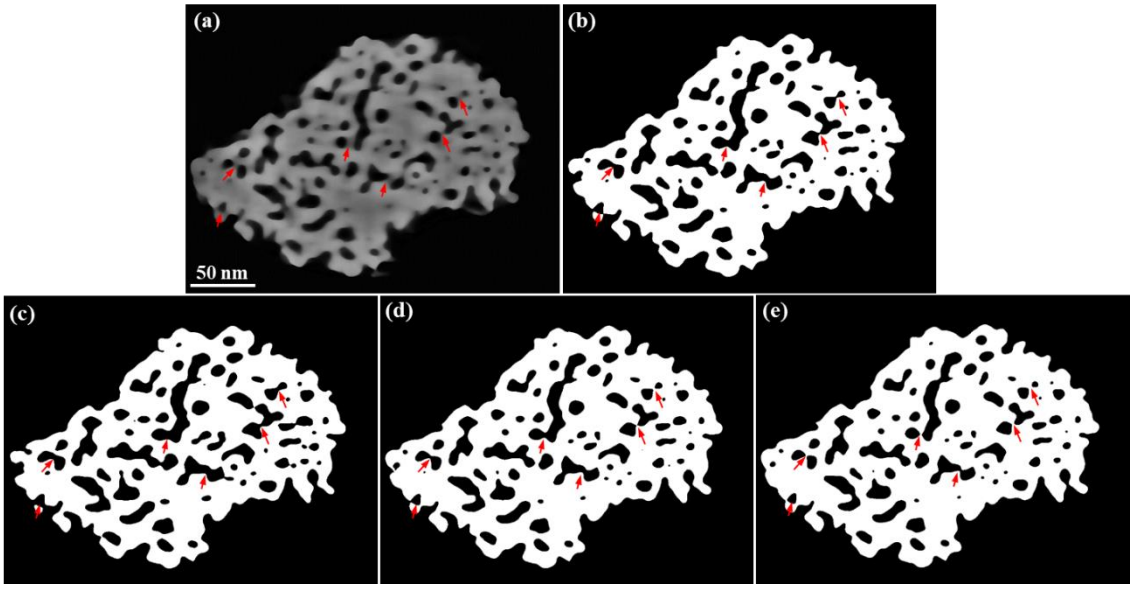

Figure 3.7: (a) Gray-scale slice of the *Phantom*.segmented-SIRT±90° reconstruction, (b) the manually defined threshold probably presented most of features and the corresponding binary slice defined by the isodata-algorithm (c), moment-preserving (d) and Otsu's (e) thresholding methods in Fiji.

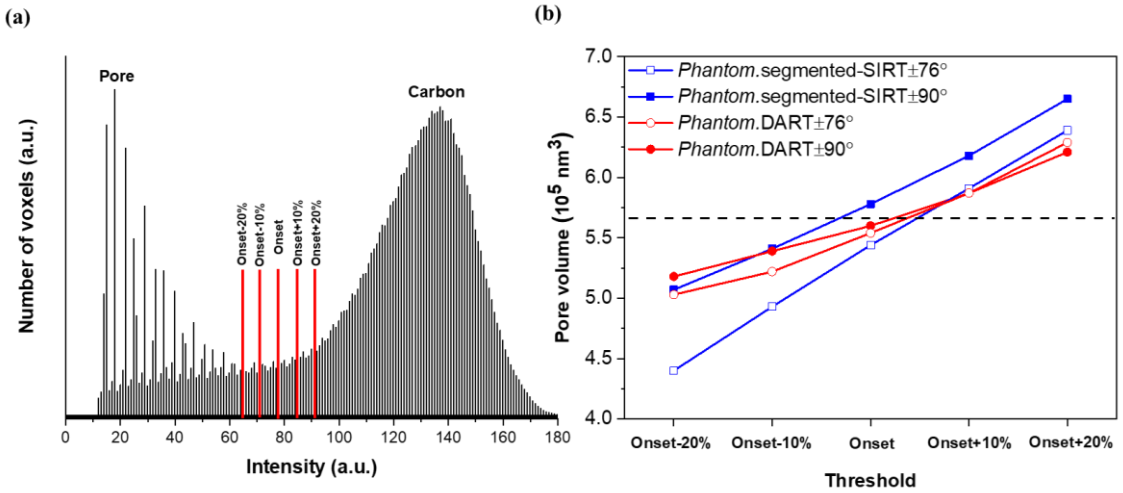

Figure 3.8: (a) Intensity histogram of a 3D reconstruction showing two main peaks corresponding to pore (void) and carbon (solid) part; (b) the effect of threshold on the reconstructed pore volume within *Phantom*.segmented-SIRT and the *Phantom*.DART reconstructions (the dash line indicates the pore volume of the reference phantom).

The *Phantom*.segmented-SIRT and the *Phantom*.DART reconstructions defined by the Onset threshold were investigated in more detail to further evaluate the fidelity of the reconstruction approaches. Representative 2D slices (Figure 3.9) and a surface rendering of the pores in 3D (Figure 3.10) were evaluated in comparison to the corresponding slice and pores of the original phantom. Visually, all four reconstructions exhibit a very similar morphology and have a high similarity with the original phantom. However, the size and 2D connectivity of some pores (highlighted areas in Figure 3.9b-e) are altered by the artifacts introduced during the reconstruction and segmentation process. To evaluate differences between the segmented reconstructions better, 'missing' pixels/voxels and 'additional' pixels/voxels in the reconstructions compared to the reference phantom are highlighted in red and green. These variations are mainly present in a few voxel wide boundary region of the pores, where the missing and additional voxels in the pores are more or less balanced with the defined threshold. Comparing the reconstructions, it is visually obvious that the *Phantom*.DART±90° reconstruction shows the least variations with a lower amount of 'missing' and 'additional' voxels.

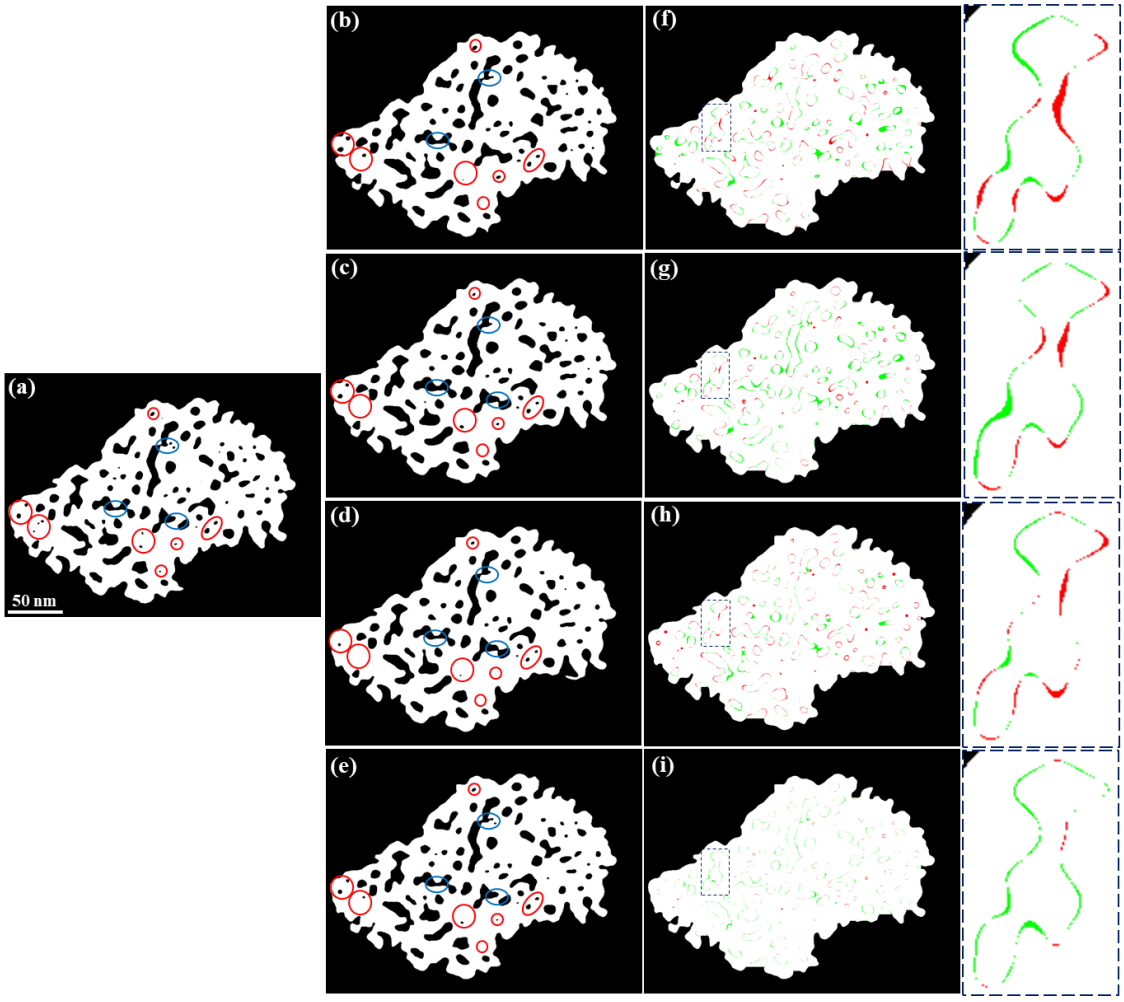

Figure 3.9: Slices of the (a) DART phantom reference, (b) *Phantom*.segmented-SIRT±76°, (c) *Phantom*.segmented-SIRT±90°, (d) *Phantom*.DART±76° and (e) *Phantom*.DART±90° reconstructions with (f-i) the differences in the pore structures: red and green parts pixels represent 'missing' and 'additional' voxels of the reconstructed pore compared to the phantom (the areas highlighted by red circles exhibit pore size variations and the blue regions indicated differences in connectivity of the pores).

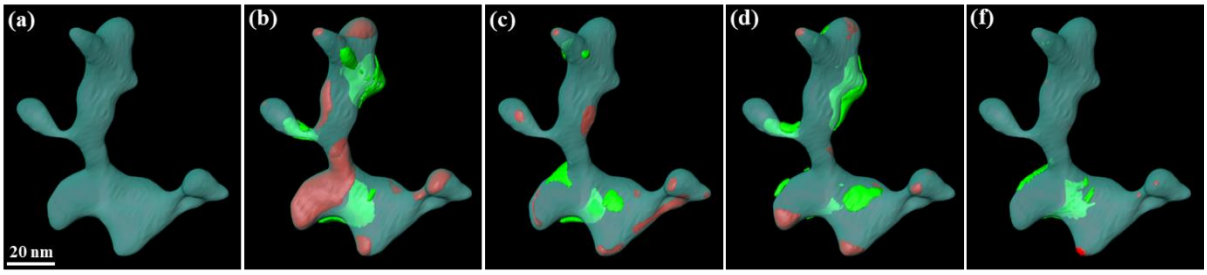

Figure 3.10: 3D view of a selected pore: (a) reference, (b) *Phantom*.segmented-SIRT±76°, (c) *Phantom*.segmented-SIRT±90°, (d) *Phantom*.DART±76° and (e) *Phantom*.DART±90° with the differences highlighted in red (missing voxels) and green (additional voxels).

The variations between these reconstructions and the reference phantom were further quantified by counting the number of differing ('missing' and 'additional') voxels for each reconstruction both on a slice-by-slice basis as well as for the overall volume. The ratio of number of differing voxels to the total number of pore voxels in the 2D slices and the 3D volume are summarized in Figure 3.11a and Table 3.2. Moreover, the similarity between reconstructed and the phantom in both 2D slices and 3D volume was measured by the structural similarity (SSIM) index[207], shown in Figure 3.11b and Table 3.2. In all investigated slices, the *Phantom*.DART±90° and *Phantom*.DART±76° reconstructions show a lower pore variation compared to the *Phantom*.segmented-SIRT reconstructions. This is also indicated by the SSIM calculation, where the *Phantom*.DART±90° data has the highest structural similarity with the initial structure. This tendency is also confirmed in investigations on the overall differences in 3D (Table 3.2). Moreover, the effect of the missing wedge is clearly observed in the comparison. Both the SIRT and the DART reconstructions obtained with a missing wedge of 28° have higher pore variations and lower structural similarity compared to the ones without missing wedge, indicating that the missing wedge resulted in a lower fidelity of reconstructions. However, this difference is lower in case of the DART reconstruction, where the missing wedge may be suppressed partially by the iterative refinement of boundary voxels in the DART implantation. The MAE calculations for this phantom studies (Figure 3.12) also indicate the same trend. All MAE values (below 1%) are significantly lower compared to the experimental values. This is presumably due to the missing noise in the phantom studies. Other factors such as slight structural changes, contamination and the beam convergence might also contribute to the higher MAE values for the experimental reconstructions.

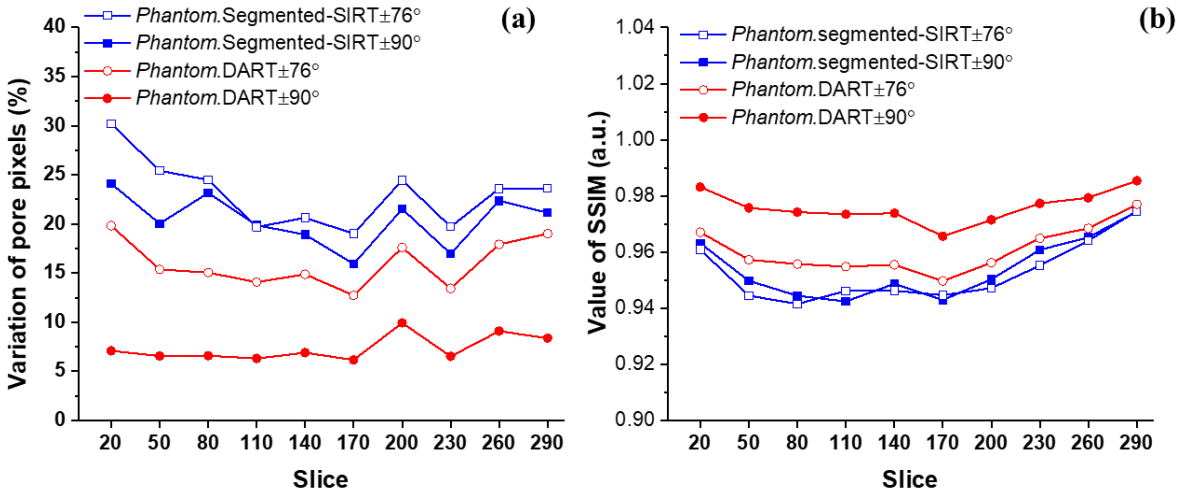

Figure 3.11: (a) Percentage of pore variation and (b) SSIM calculated for slices distributed throughout the reconstructed volume for the four phantom reconstructions.

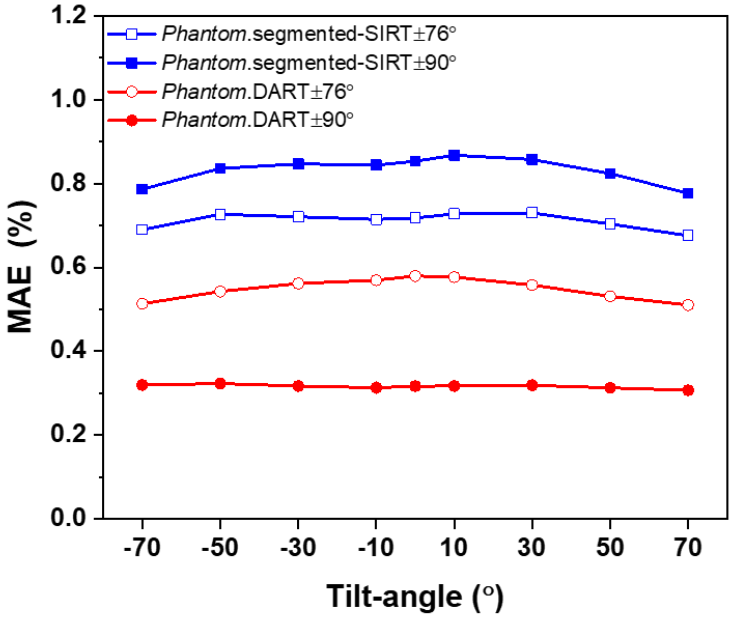

Figure 3.12: MAE calculation for the *Phantom*.segmented-SIRT and *Phantom*.DART reconstructions at angles of -70°,-50°,-30°,-10°, 0°, 10°, 30°, 50° and 70°.

Table 3.2: Pore variation and SSIM calculation for the phantom segmented 3D reconstructions.

Segmentation	Pore variation (%)	SSIM
Phantom.segmented-SIRT±76°	21	0.946
Phantom.segmented-SIRT±90°	19	0.947
Phantom.DART±76°	15	0.954
Phantom.DART±90°	7	0.973

The above evaluation clearly shows that the segmented 3D reconstructions are not perfect even though they are close to the original phantom structure visually. Therefore, the reconstructed phantom structures were analyzed analogously to the experimental data to further evaluate the effect of the differences on the morphological parameters and diffusion properties. Table 3.3 summarizes the quantitative information on the pore morphology derived from CLD and skeleton analysis. The morphological parameters of all four reconstructions are quite similar to the reference phantom. Especially, the mean coordination number and the tortuosity indicate that the topology of the constructed volumes fit well. This fits to the visual analysis of the pores in 3D (Figure 3.10) and suggests that the connectivity differences observed in individual 2D slices (Figure 3.9) do not significantly alter the 3D pore connectivity. However, it should be noticed that the geometry related parameters including pore diameter and length, μ as well as the total pore volume show slightly stronger differences in the four reconstructions. Moreover, the *k* values, the indicator for the homogeneity of pore structure, are found higher in both the segmented-SIRT and the DART reconstructions, especially for the limited tilt range of ±76°. This might be due to the effect of the missing wedge on the reconstructions.

Table 3.3: Quantitative morphological information on the pore structure.

Data	**CLD analysis**		**Skeleton analysis**						
	μ (nm)	k	Pore volume[a] (10^5 nm^3)	Pore volume[b] (10^5 nm^3)	Pore diameter (nm)	Pore length (nm)	Tortuosity	Coordination number	
								3	>3
Reference(DART)	10.9	3.10	5.67	0.79	5.6±2.1	13.3±10.3	1.15±0.24	94.8%	5.2%
***Phantom*.SIRT±76°**	11.5	3.23	5.44	0.75	5.6±2.5	14.6±11.8	1.16±0.48	95.6%	4.4%
***Phantom*.SIRT±90°**	12.3	3.16	5.78	0.90	6.2±2.5	14.8±11.2	1.15±0.23	96.0%	4.0%
***Phantom*.DART±76°**	11.7	3.23	5.54	0.80	5.9±2.4	13.8±11.2	1.12±0.17	94.9%	5.1%
***Phantom*.DART±90°**	11.4	3.15	5.60	0.82	5.8±2.3	13.7±11.2	1.14±0.21	94.8%	5.2%

[a] the overall pore volume of reconstruction.
[b] the pore volume within largest cubic domain.

To further compare the differences between the reconstruction algorithms and to evaluate the effect of the missing wedge, the diffusion behavior within the 3D pore volume of the phantom reconstructions have been simulated as before for the experimental data (Figure 3.13a). The effective diffusion of the four reconstructions are discussed within the largest cubic domain. The calculated diffusion value of the *Phantom*.segmented-SIRT±76° reconstruction is about 14% lower while the value of *Phantom*.segmented-SIRT±90° reconstruction is about 21% higher compared to the reference. This difference may be partially due to the pore volume variation between the reconstructions. The *Phantom*.segmented-SIRT±76° has a pore volume about 5% lower than the reference, whereas the *Phantom*.segmented-SIRT±90° has a pore volume about 14% higher than the reference. In case of the *Phantom*.DART reconstructions, the variation of the diffusion coefficients compared to the reference is

significantly smaller, 7% in case of *Phantom*.DART±76° and 3% in case of *Phantom*.DART±90°. However, it should be noted that the corresponding pore volume of *Phantom*.DART±76° is almost same as the reference (1% higher) while the *Phantom*.DART±90° is 4% higher. This indicates that the pore volume is not the only factor affecting the diffusion constant variations in the 3D reconstructions. The slight morphology differences and necking between pores observed in above parts also play a potential role for the variation of the diffusion in 3D.

The effect of the missing wedge was investigated as another critical parameter influencing the measured diffusion properties. In particular, this causes the anisotropy of the determined diffusion properties, which were evaluated by separately analyzing the diffusion along *x*-direction (perpendicular to the tilt-axis and the electron beam direction), *y*-direction (parallel to the tilt-axis) and *z*-direction (parallel to the electron beam direction), using the corresponding orientation dependent diffusion coefficients (Figure 3.13b-c). Because the initial pore structure in the investigated cubic domain is not fully isotropic, it is not possible to directly compare the diffusion coefficients for the different directions. Instead, the differences of each component relative to the reference phantom are compared. In case of the *Phantom*.segmented-SIRT±76°, it has the 14% lower diffusion value in 3D compared to the reference, but the *z*-component of the diffusion is obviously enhanced and almost the same as the diffusion in this direction of reference. This is the expected result of the missing wedge, which leads to a lower intensity of pore walls (solid) oriented perpendicular to the electron beam and therefore enhances the pore (void) length/connectivity in *z*-direction. Beyond this, it was also found that the missing wedge has a significantly different effect on the *x*- and *y*-component of the diffusion coefficients, which has not been considered before. The *x*-component of the diffusion is 10% lower than the reference value and slightly enhanced compared to the difference in 3D. However, the *y*-component of the diffusion is strongly reduced with a 56% lower value compared to this direction in the reference. This was a surprise as the y-component is typically considered the direction least affected by the tomography reconstruction. In order to understand this effect better, a SIRT reconstruction of a 3D shell as a simplified model for a pore was investigated (Figure 3.14). The missing wedge significantly reduces the reconstructed intensities of the shell perpendicular to the *z*-direction because of the strong Fourier coefficients for this part of the shell within the missing wedge (Figure 3.14a/b). Furthermore, anisotropy for the central slice in *x*- and *y*-direction (Figure 3.14c) is also revealed in this reconstruction. The intensity profile in the three directions (Figure 3.14d) indicates that the shell perpendicular to the *y*-direction has the highest reconstructed intensities, slightly higher than the intensities of the shell perpendicular to the *x*-direction and much higher than the intensities of the shell perpendicular to the *z*-direction. Therefore, the effective diffusion coefficient in the three directions should be inversely affected, which is exactly the trend seen in the diffusion simulations of the *Phantom*.segmented-SIRT±76° reconstruction compared to the reference. In case of the *Phantom*.DART±76° reconstruction, the anisotropy of the effective normalized diffusion components is significantly reduced compared to the *Phantom*.segmented-SIRT±76° reconstruction, which suggests that the missing wedge artifacts were significantly reduced in the DART reconstruction. However, it

still shows the same trend as seen in the SIRT reconstruction. The z-component is enhanced and 13% higher compared to the reference while the x-component and the y-component are almost the same. This residual anisotropy indicates that the missing wedge artifacts were not fully compensated for in the DART reconstruction.

In the reconstruction with the full tilt range of ±90°, it was found in the *Phantom*.segmented-SIRT±90° that the normalized diffusion constants in x- and z-direction are slightly higher compared to y-direction, which may be due to artifacts in the SIRT implementation. To better understand this, a tilt-series of projections of a 3D shell model covering the full tilt-range of ±90° was reconstructed using SIRT. This revealed that the intensity of shell in x-and z-direction is lower compared to y-direction (Figure 3.14e) and therefore a higher diffusion both in x-and z-direction, which is exactly the same observation in diffusion simulations of the *Phantom*.segmented-SIRT±90° reconstruction. In case of the *Phantom*.DART±90°, the anisotropy of the diffusion components is again significantly reduced, resulting in a just slightly higher component in z-direction compared to the other two directions.

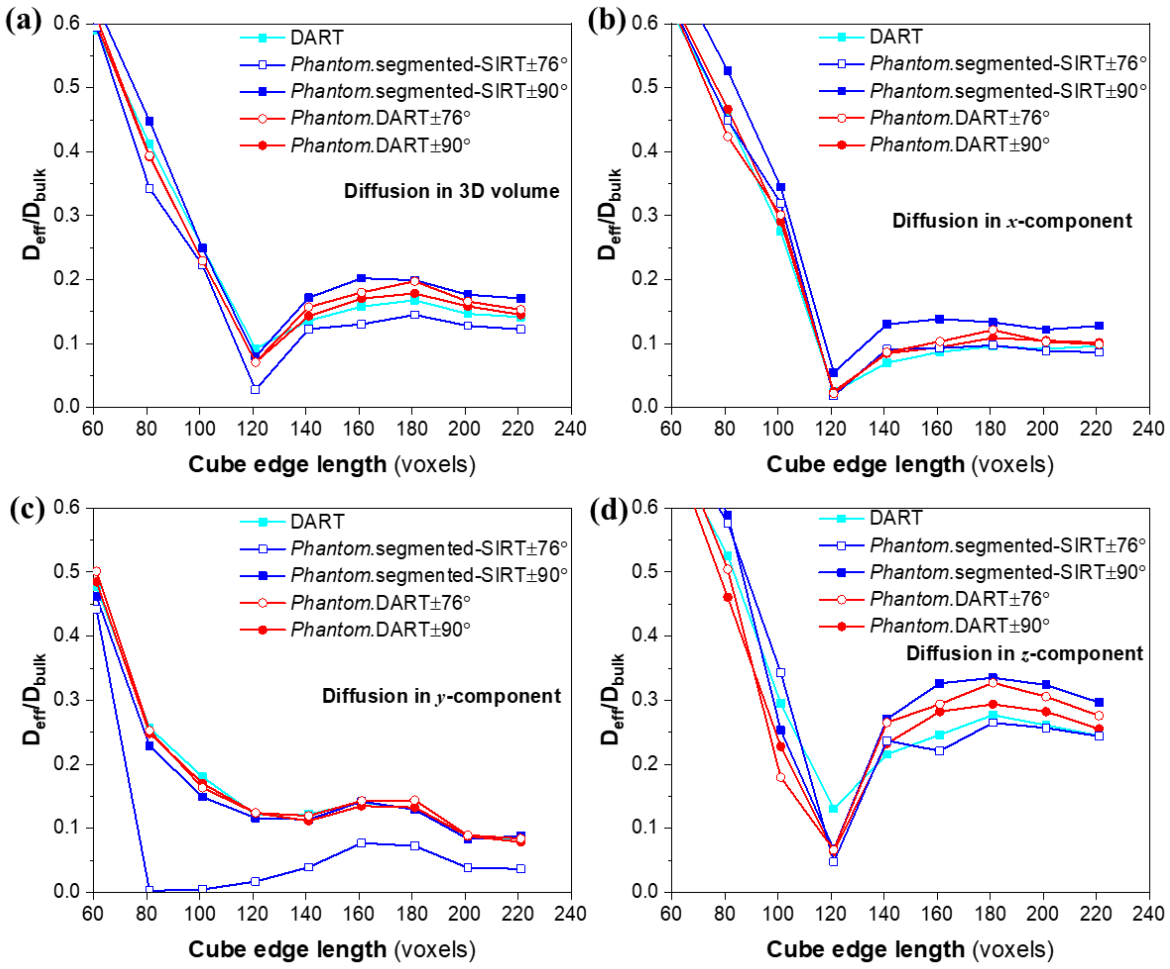

Figure 3.13: Effective diffusion normalized by the bulk diffusion as a function of the simulation box size (a) 3D, (b) x-component, (c) y-component and (d) z-component.

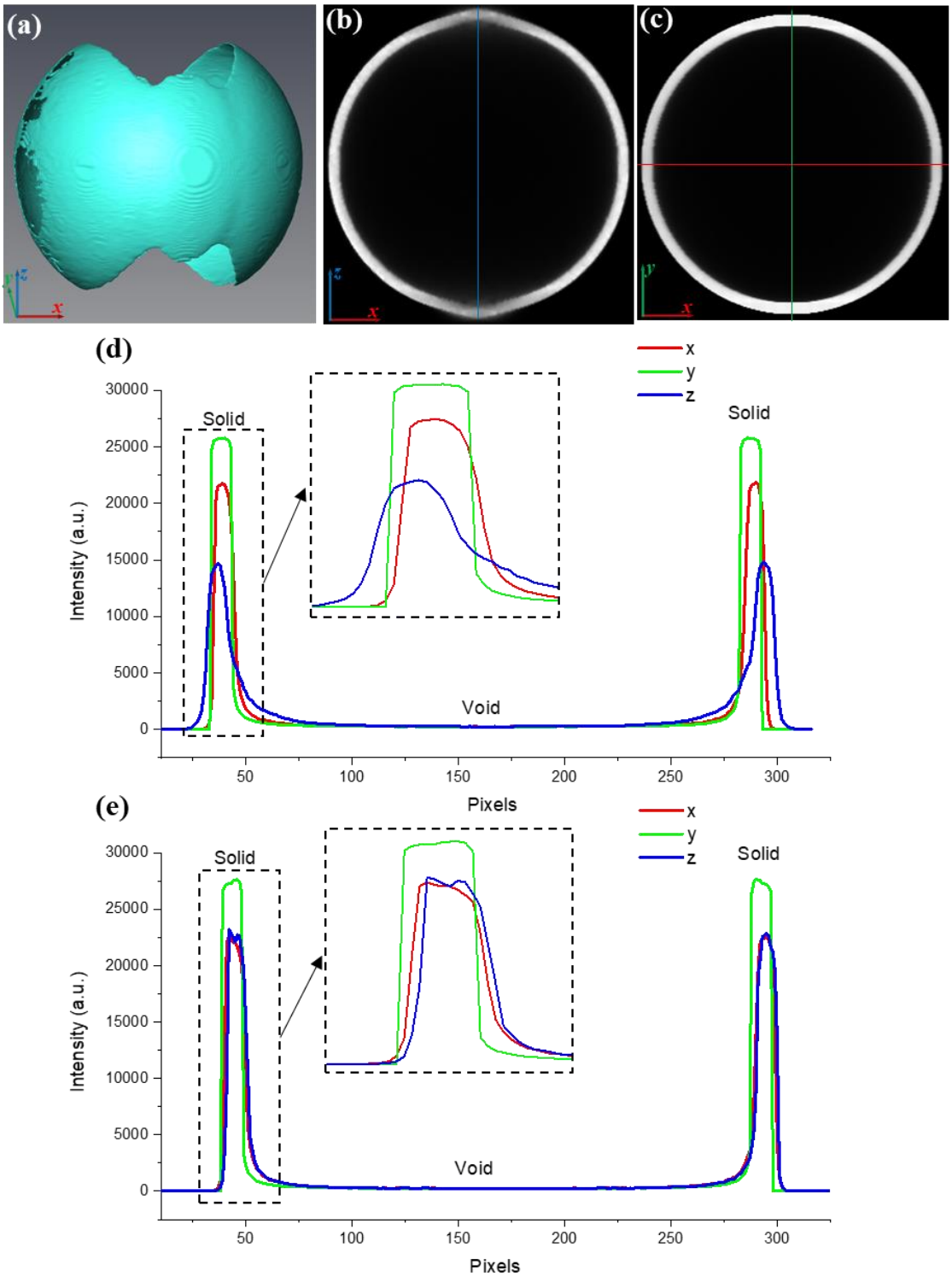

Figure 3.14: Phantom study of a shell reconstructed using SIRT with a tilt-range of ±76°: (a) surface rendering of the reconstructed structure; central (b) *xz* and (c) *xy* slices and the corresponding intensity profile of central lines in *x*, *y* and *z* directions (red, green and blue lines in b and c) indicating the anisotropy effect of the missing wedge on the reconstructed intensity. (e) The intensity profile of central lines in *x*, *y* and *z* directions of the same shell phantom reconstructed using SIRT with a tilt-range of ±90°.

3.6. Conclusions

Quantifying morphology and diffusion properties of a disordered mesoporous carbon material have been investigated based on an electron tomographic reconstruction. The quantitative analysis strongly relies on the fidelity of the reconstruction and the segmentation. It is found that the fidelity of the reconstruction is affected by pore size variations, the missing wedge and the reconstruction approach. In both the SIRT and DART reconstruction, the geometry and topology of pore structure can be evaluated reliably even in the presence of a limited missing wedge. However, the measured pore volume varies depending on the threshold used for segmentation. Particularly, it is difficult to reproducibly define a uniform global threshold for SIRT reconstruction. This results in around 25% difference of pore volume between the experimental SIRT and DART reconstruction. In turn, the diffusion constants calculated by the diffusion simulation differed by ~51% between the two experimental reconstructions because the diffusion through the pore network depends strongly on porosity, i.e., on the void volume fraction.

With the phantom study of the reconstructed mesoporous carbon, the fidelity of the reconstruction and segmentation approach for disordered mesoporous materials was investigated in more detail. The pore volume of the SIRT reconstruction is more sensitive to the threshold settings compared to the DART reconstruction. This makes it more difficult to define a good global threshold and thus to reproducibly measure the pore volume based on a SIRT reconstruction. In addition, the pore variations introduced in the reconstruction and segmentation process are mainly present in a few voxel wide boundary region of the pores. This slightly alters the local size of the pore structure, but does not significantly affect the morphology. However, it is found that the measured effective normalized diffusion coefficients vary for the different reconstructions, mainly due to differences in the pore volume. Nevertheless, a reproducible measurement of the diffusion coefficient was found in the DART reconstruction. Moreover, investigations on the SIRT reconstruction indicate that the missing wedge artifacts result in a noticeable anisotropy of the measured x-, y- and z-components of the diffusion coefficients, where the z-component has the highest diffusion coefficients while the y-component shows the lowest diffusion coefficient. However, it should be noted that this anisotropy is strongly reduced in the DART reconstruction, where the differences are only a few percent even in the presence of a limited missing wedge.

In summary, this indicates that electron tomography based on a DART reconstruction is possible to provide a reproducible and reliable analysis of the pore structure of mesoporous materials. This can be critical input for understanding structure-property relationships in heterogeneous catalysis, especially for the effective normalized diffusion properties of porous support. The SIRT reconstruction also enables a reasonable analysis of the pore structure. However, as the absolute pore fraction is difficult to determine accurately, the absolute diffusion constant is not measured very accurately. Nevertheless, diffusion properties can be compared when normalized with respect to the mean pore diameter as has been demonstrated in collaboration with the group of Prof. Tallarek[208].

4. Tailoring the 3D structure of Pd nanocatalysts supported on mesoporous carbon for furfural hydrogenation

In this chapter, electron tomography is applied to quantitatively characterize the metal NP distribution to correlate structural differences of Pd/CMK-3 catalysts with their performance in liquid phase furfural hydrogenation.

4.1. Introduction

Furfural offers a rich platform to generate biofuels[209,210] as well as chemical intermediates[211] has been identified as one of the most promising chemicals for a sustainable production in the 21st century.[212] Apart from rearrangements and furan coupling, hydrogenation is the most important process in the conversion of furfural.[211] Figure 4.1 shows the reaction pathways of furfural hydrogenation, in which hydrogenation of furfural can generate a variety of different products. In order to optimize the hydrogenation for the desired product, one has to understand the catalytic mechanism for each of the products, correlate this with the structural features of the catalyst and then optimize the catalyst synthesis accordingly. Therefore, it is critical to characterize the full structure of the catalyst. As introduced in chapter 1, the location and distribution of the supported NPs has a significant effect on the catalytic performance. To better understand this effect, a precise determination of location and distribution of NPs is essential.

The works of de Jong et al.[72,76,141–144] and Midgley et al.[213,214] have pioneered the 3D characterizations of the morphology and location of small metal particles deposited inside zeolites and mesoporous networks by means of electron tomography. It has been shown that the spatial distribution of NPs in porous supports, such as SBA-15, is an important factor for catalyst stability[143,144] or that confinement of Au NPs inside CNTs significantly enhances the catalytic activity and promotes selectivity towards di-acid products in polyol oxidation[33]. However, so far no systematic work has been performed to investigate the relationship between the spatial distribution of supported NPs on/in porous carbons and the catalytic properties in furfural hydrogenation. In this work, based on a quantitative tomographic analysis, the 3D distribution of Pd NPs supported on an ordered porous CMK-3 carbon with well-defined pore structure has been systematically investigated for catalysts prepared by three synthetic methods: incipient wetness impregnation, wet impregnation and immobilization of preformed PVA stabilized NPs. The correlation of the resulting spatial distribution of the Pd NPs in/on the three Pd/CMK-3 catalysts and their influence on activity, selectivity and stability in furfural hydrogenation is evaluated.

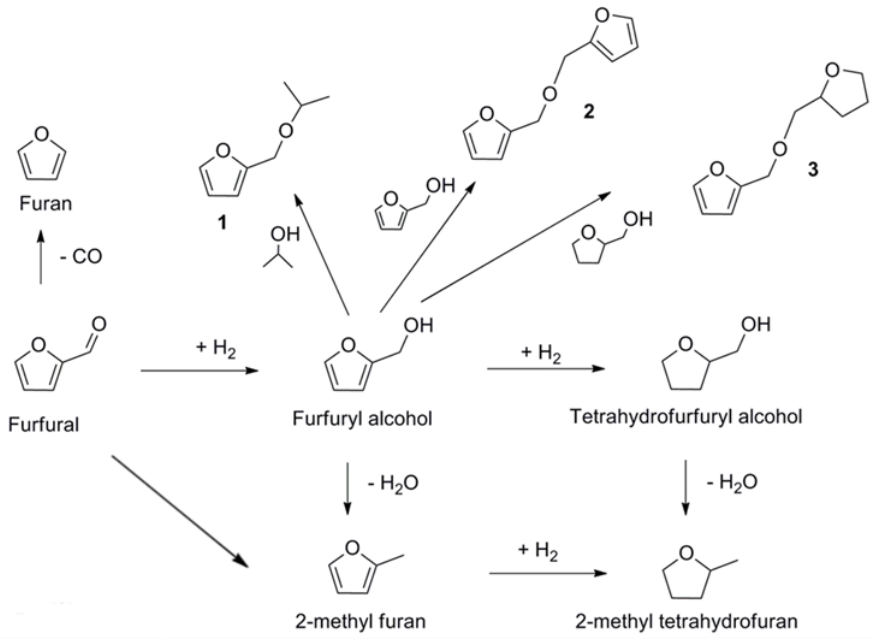

Figure 4.1: Representative reaction pathways during hydrogenation of furfural.

4.2. Experimental

4.2.1. Catalyst preparation

The mesoporous carbon CMK-3 (Nanjing XFNANO Materials Tech) with a specific surface area of ~900 m^2/g shows an ordered porous structure with a pore diameter of 3-4 nm. The Pd/CMK-3 catalysts were synthesized using incipient wetness impregnation (Pd_{IW}/CMK-3), wet impregnation (Pd_{IMP}/CMK-3) and immobilization of preformed PVA stabilized NPs (Pd_{PVA}/CMK-3). The catalyst synthesis has been done by Dr. Alberto Villa at the University of Milano.

For incipient wetness impregnation, solid $Na_2PdCl_4 \cdot 2H_2O$ (Aldrich, purity 99.99 %) (0.094 mmol of Pd) was dissolved in water. Based on the total pore volume estimated from N_2 sorption analysis (1.24 cm^3/g), metal-containing solution was added to 1 gram of support (CMK-3) to completely fill the pores. The concentration of the precursor solution was calculated to obtain a final metal loading of 1 wt.%. The catalyst was filtered, re-dispersed in water and reduced with $NaBH_4$ ($Pd/NaBH_4$, 1/8 mol/mol). Afterwards the catalyst was filtered and washed several times with distilled H_2O and dried at 80 °C for 4 h.

For wet impregnation, solid $Na_2PdCl_4 \cdot 2H_2O$ (0.094 mmol of Pd) was dissolved in 100 mL water. The resulting Na_2PdCl_4 solution was mixed with 1 gram of support (CMK-3) under stirring for 4 h. Then the catalyst was filtered, re-dispersed in water and reduced with $NaBH_4$ ($Pd/NaBH_4$, 1/8 mol/mol). After that, the catalyst was filtered and washed several times with distilled H_2O and dried at 80 °C for 4 h.

For sol-immobilization, solid $Na_2PdCl_4 \cdot 2H_2O$ (0.094 mmol of Pd) and PVA water solution (1 wt.%) (Pd/PVA, 1/0.5 wt/wt) were added to 100 mL of H_2O. After 3 min, $NaBH_4$ ($Pd/NaBH_4$, 1/8 mol/mol)

solution (the reduction agent) was added to the mixed solution (yellow-brown) under vigorous magnetic stirring to form a brown Pd(0) sol. An UV/Vis spectrum of the Pd sol was recorded to check that the reduction of $PdCl_4^{2-}$ was complete. Within a few minutes from their generation, the colloid (acidified at pH 2 by sulphuric acid) was immobilized by adding the support (CMK-3) under vigorous stirring. The amount of Na_2PdCl_4 and support was calculated in order to obtain a final metal loading of 1 wt.%. The catalyst was filtered and washed several times with distilled H_2O at 60°C to remove excess PVA and dried at 80 °C for 4 h.

4.2.2. Furfural hydrogenation

The catalytic testing for furfural hydrogenation has been done by Dr. Alberto Villa at University of Milano. Furfural hydrogenation was performed at 50°C, using a stainless steel batch reactor (30 mL capacity) equipped with heater, mechanical stirrer, gas supply system and thermometer. Furfural solution (15 mL; 0.3 M in 2-propanol) was added into the reactor and the desired amount of catalyst (Furfural /catalyst, 500/1 wt/wt) was suspended in the solution. The H_2 pressure was set to 5 bar to avoid the mass transport. The mixture was heated to the reaction temperature of 50 °C and mechanically stirred (1250 rpm). During the reaction, samples were removed periodically (0.2 mL) and identification of the products was performed using a Thermo Scientific Trace ISQ QD Single Quadrupole GC-MS equipped with a capillary column HP-5 30 m x 0.32 mm, 0.25 x m Film, by Agilent Technologies. Quantitative analysis with an external standard method (n-octanol) was used. After 5h, at the end of the reaction, the autoclave was cooled to room temperature, the H_2 flow stopped and the autoclave purged with flowing nitrogen. Recycling tests were carried out under the same experimental conditions. The catalyst was recycled for the subsequent run after filtration without any further treatment.

4.2.3. Atomic absorption spectroscopy

Metal content and metal leaching was verified by atomic absorption spectroscopy (AAS) using a Perkin Elmer 3100. After 60 min of reaction time, the catalyst was isolated by filtration without cooling the reaction mixture and inductively coupled plasma (ICP) were used to measure the filtrate. This work has been done by Dr. Alberto Villa at the University of Milano

4.2.4. Transmission electron microscopy and electron tomography analysis

The powdered Pd/CMK-3 catalysts were dispersed on copper grids coated with holey carbon film (Quantifoil). The morphology of the catalysts was characterized by HAADF-STEM using a FEI Titan 80-300 TEM operated at 300 kV. The size of the supported Pd NPs was estimated from HAADF-STEM images using ImageJ[192] approximating the particles with an elliptical shape. For electron tomography analysis, a small amount (~5 μL) of colloidal Au NPs (6.5 nm diameter, University of Utrecht) solution was dropped on the 100x400 mesh carbon coated copper grids (Quantifoil) and then residual solvent was removed from the grid. After it dried at room temperature, the powders of the catalysts were directly dispersed on the so prepared copper grids. Electron tomography was performed

using a Fischione 2020 tomography holder in the FEI Titan 80-300 microscope operated at an acceleration voltage of 300 kV in STEM mode with a nominal beam diameter of 0.27 nm. HAADF-STEM tilt series with image dimensions of 2048 x 2048 pixels were collected using the Xplore3D software (FEI Company) over a tilt range of at least ±70°, with tilt increments of 2°. Alignment of the tilt series was performed in IMOD[191] using both Au colloids and supported Pd NPs as fiducial markers. A mean residual error of 0.47-1.00 pixels was achieved as final alignment quality. The aligned tilt series were reconstructed using SIRT implemented in Inspect3D (FEI Company). The resulting tomograms had a final voxel size of 0.32 or 0.46 nm.

4.3. Analysis of the 3D reconstruction

4.3.1. Determination of the 3D Pd locations in Pd/CMK-3 catalysts

3D image analysis and segmentation of the electron tomograms of Pd/CMK-3 catalysts were performed in Amira 6.0 (FEI Company). The reconstructed volumes were denoised using median-filtering and then a global threshold was applied to the volumes to extract the features of interests, *i.e.*, Pd NPs and CMK-3 support. Afterwards, the segmentation of the Pd NPs was refined by an adaptive threshold, where the adaptive threshold was set to a certain percentage of the local maximum intensity within the particle region to dynamically compute the segmentation of each individual Pd particle. The border of the segmented CMK-3 was eroded by 20 voxels to detect the particles on the support surface as Pd particles in contact with vacuum (Figure 4.2). This erosion step is essential to avoid recognizing the intensity gradient between metal particle and vacuum as carbon. The number of NPs on the external surface and inside the pores of the support was counted and the NP sizes measured as the diameter of volume-equivalent spheres. The measured volumes were corrected by the elongation factor for the missing wedge.[154,202] Segmented Pd NPs with volumes below 20 voxels (small than 0.66 or 1.95 nm^3 depending on the voxel size of tomogram) were ignored during further analysis. To provide sufficient statistical sampling and to explore the influence of the size of the support on the particle distribution, several tomograms were analyzed for each catalyst after segmentation and identification of the particles to calculate the surface particle fraction and the NP size distribution. In addition, Pd loading (in wt.%) for individual Pd/CMK-3 tomogram was calculated based on the volumes derived for Pd and the support (CMK-3) segmentation using the nominal densities of metallic Pd (12.02 g/cm^3) and CMK-3 carbon (~0.6 g/cm^3).

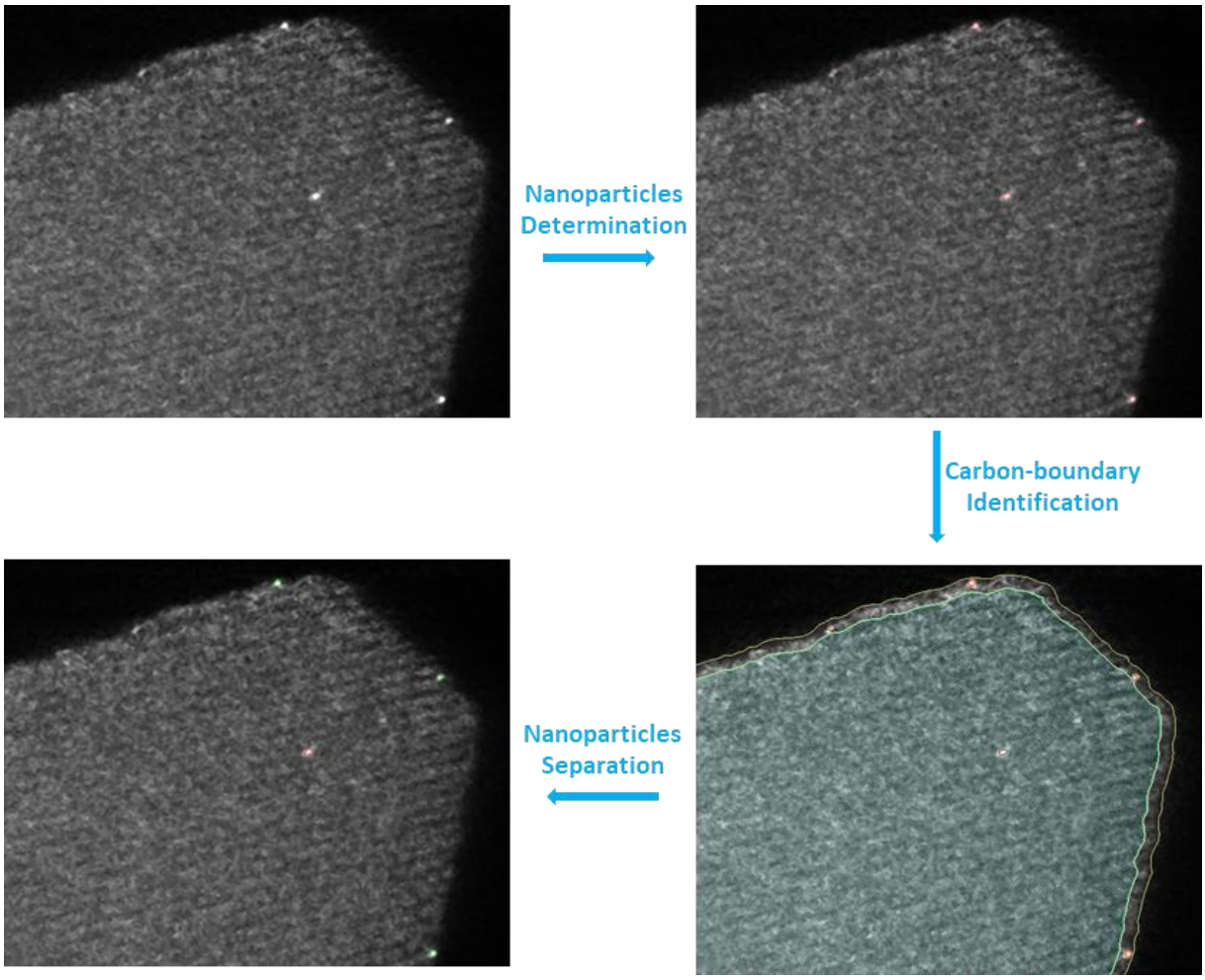

Figure 4.2: Detection of Pd NPs located on the outer surface or inside the pores of the CMK-3 support by segmentation of the reconstructed 3D volume and refining the 3D boundary.

4.3.2. Calculation of the pore area to support volume ratio in CMK-3 material

A tomogram of pure CMK-3 support was acquired at a resolution comparable to the Pd/CMK-3 data sets and an inner part of this tomogram was cropped. The cropped volume was manually segmented and divided into two parts: pore space and the carbon framework as shown in Figure 4.3. Based on the segmentation data, the surface area of the pores and the size of the whole volume were measured to calculate the ratio of the internal surface area and the support volume (Table 4.1). This ratio is a constant because of the regular columnar shape of the CMK-3 pores. For each tomogram of the Pd/CMK-3 catalysts, the external surface area of the CMK-3 support was measured in the segmented data and the internal pore surface calculated based on the volume of the segmented CMK-3 using the pore area/support volume ratio calculated from the pure CMK-3 support tomogram.

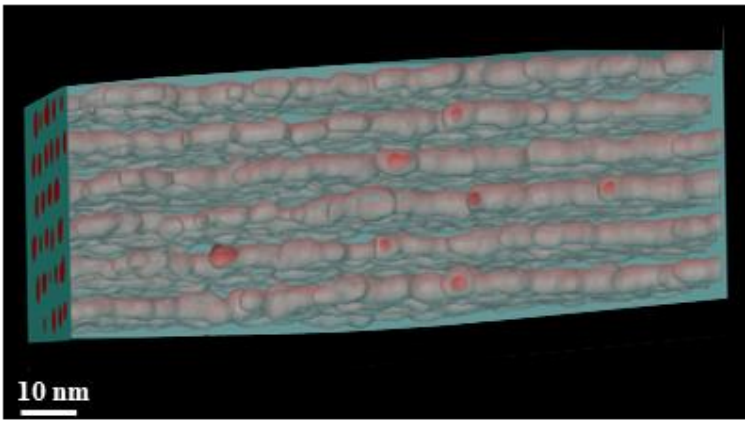

Figure 4.3: 3D view of the pore and carbon framework of a cropped region from CMK-3 materials.

Table 4.1: The calculation of the inner pore area/support volume ratio.

CMK-3 volume	4.48×10^5 nm^3
Area of inside pore	7.26×10^4 nm^2
Ration of inside pore area/CMK-3 volume	0.16 nm^{-1}

4.4. Furfural hydrogenation testing and STEM measurements of Pd/CMK-3 catalysts

The results of furfural hydrogenation testing of the three Pd/CMK-3 catalysts are summarized in Table 4.2 and the representative reaction pathways during hydrogenation of furfural are illustrated in Figure 4.1. The initial activity (1125 h^{-1}) of the Pd_{IMP}/CMK-3 catalyst is higher than that of Pd_{PVA}/CMK-3 (750 h^{-1}) and Pd_{IW}/CMK-3 (438 h^{-1}). However, analysis of the conversion versus time on stream (Figure 4.4a) revealed that Pd_{PVA}/CMK-3 obtained the highest conversion (98%) after 5 hours, compared to Pd_{IMP}/CMK-3 (88%) and Pd_{IW}/CMK-3 catalysts (64%), where the Pd_{IMP}/CMK-3 catalyst exhibited a significant deactivation over time at high conversion. In all cases, furfuryl alcohol was the major product (Table 4.2). Pd_{PVA}/CMK-3 showed a selectivity to furfuryl alcohol of 75%, higher than Pd_{IW}/CMK-3 (61%) and Pd_{IMP}/CMK-3 (56%). Tetrahydrofurfuryl alcohol was the major secondary product for Pd_{IMP}/CMK-3 (24%) and Pd_{PVA}/CMK-3 (13%), whereas Pd_{IW}/CMK-3 promoted the formation of methyl furan with a selectivity of 22%. Moreover, the stability of the catalysts was investigated by recycling tests as shown in Figure 4.4b-d, where these recycling tests consisted of the filtration and reuse of the catalyst for the next run without further purification. Both Pd_{IW}/CMK-3 and Pd_{PVA}/CMK-3 catalysts exhibited good stability, maintaining activity and selectivity over 6 cycles (Fig. 4.4b and 4.4d). Conversely, a clear decrease in the conversion and continuous changes in the selectivity were found in Pd_{IMP}/CMK-3 catalyst (Fig. 4.4c): the selectivity for tetrahydrofurfuryl alcohol is enhanced while the selectivity of furfuryl alcohol and methyl furan decreases with increasing cycles. To investigate differences of catalytic behavior of the three catalysts, the as-prepared Pd/CMK-3 catalysts were characterized using STEM to assess the particle size. Figure 4.5 shows STEM images of the three catalysts and their NP size histograms. Pd NPs of the three catalysts exhibit a fairly homogeneous

dispersion on the support and the Pd NP size of all catalysts is similar, around 2.5 nm with a similar size distribution. This indicates that there are clearly other factors rather than the particle size that influence the activity and selectivity.

Table 4.2: Furfural hydrogenation in 2-propanol[a].

Catalyst[a]	Activity[b]	Conversion (%) after 5h	Selectivity (%)[c]					
			Furfuryl alcohol	Tetrahydrofurfuryl Alcohol	2-methyl furan	Ethers		
						1	2	3
Pd_{IW}/CMK-3	438	64	61	8	22	5	nd	nd
Pd_{IMP}/CMK-3	1125	88	56	24	6	8	4	nd
Pd_{PVA}/CMK-3	750	98	75	13	-	7	nd	nd

[a] Reaction conditions: Furfural = 0.3 M; F/catalyst ratio=500 wt/wt, 50°C, 5 bar H_2.

[b] Converted mol (mol Pd)$^{-1}$ h^{-1} calculated after 15 min of reaction.

[c] Selectivity calculated at 60% conversion.

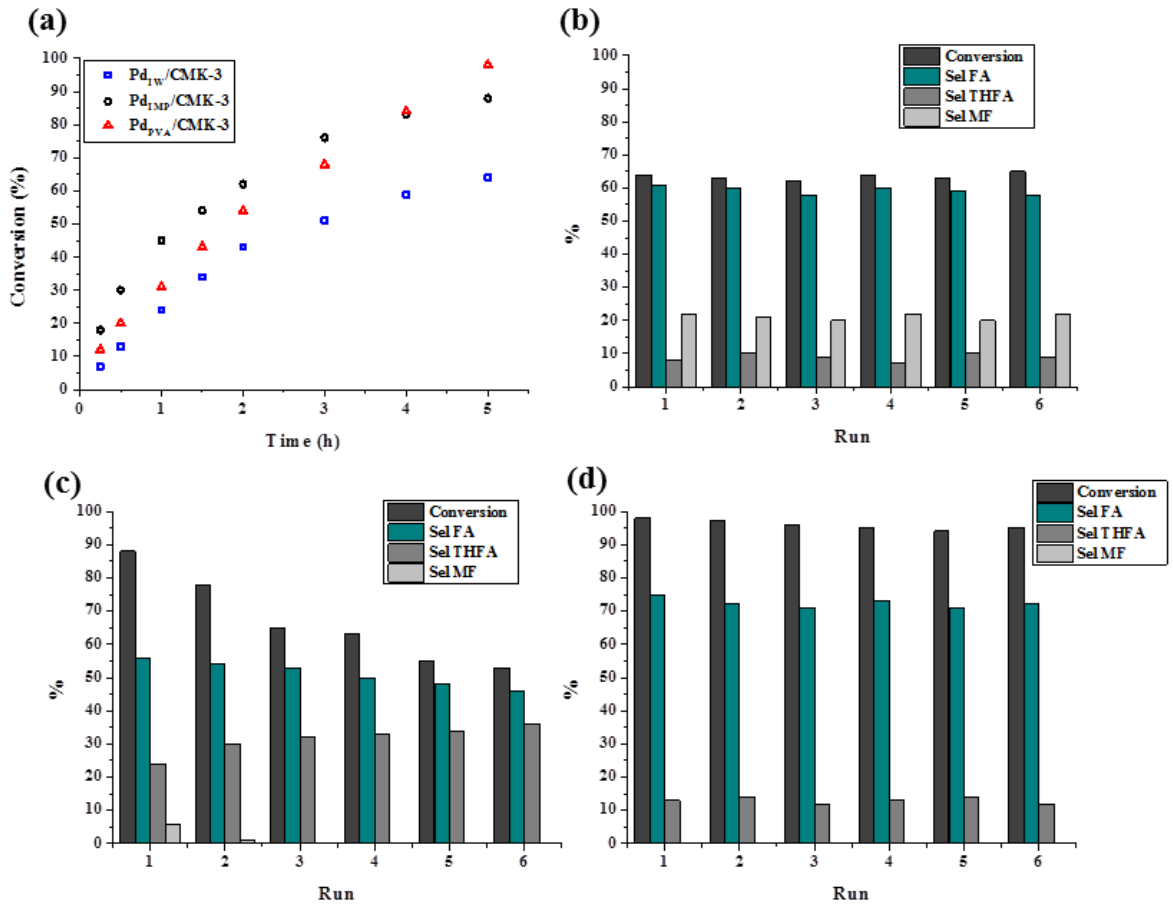

Figure 4.4: (a) Reaction profiles for Pd/CMK-3 catalysts during the 1st cycle of furfual hydrogenation and stability tests running in 6 reaction cycles of (b) Pd_{IW}/CMK-3, (c) Pd_{IMP}/CMK-3 and (d) Pd_{PVA}/CMK-3 catalysts. (FA: Furfuryl alcohol, THFA: Tetrahydrofurfuryl alcohol, MF: 2-methyl furan).

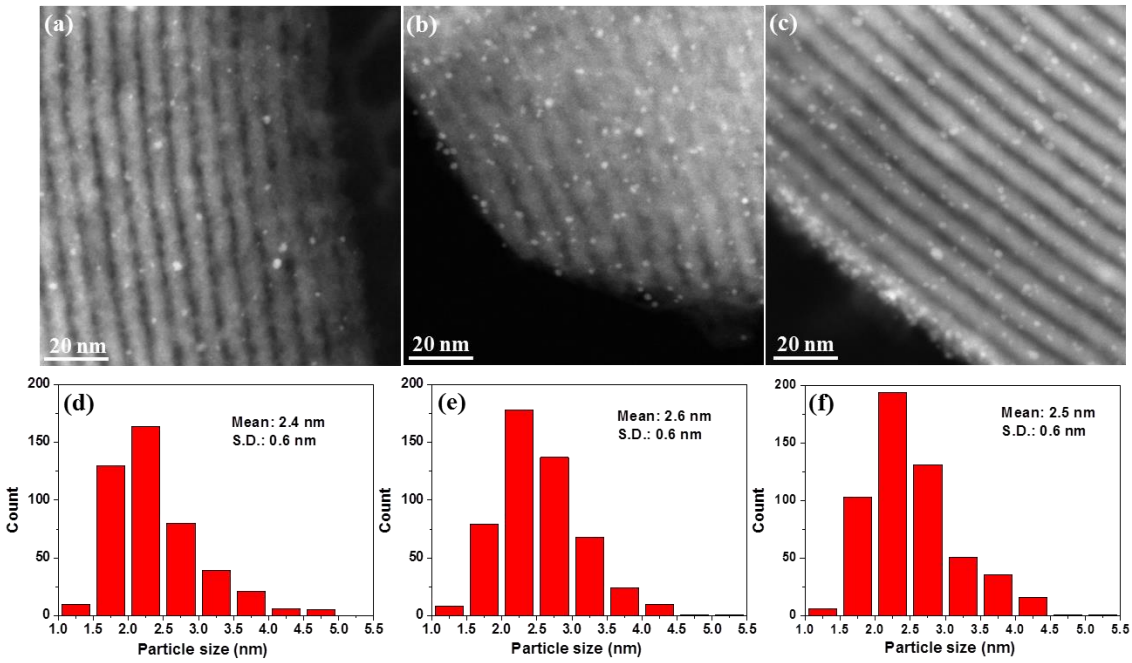

Figure 4.5: Representative STEM images of as-prepared (a) Pd_{IW}/CMK-3, (b) Pd_{IMP}/CMK-3 and (c) Pd_{PVA}/CMK-3 catalysts and (d-f) the corresponding particle size distribution histograms.

4.5. Quantification of the Pd distribution in the Pd/CMK-3 catalysts

To further evaluated the origin of the performance difference of the catalysts, the 3D distribution of supported Pd NPs has been investigated by electron tomography. Figure 4.6 shows representative 2D slices of the reconstructed volume of the three Pd/CMK-3 catalysts and the corresponding surface rendered volumes. NPs inside the pores are marked in red and NPs on the external surface are marked in green. Pd NPs were found both inside the support pores and on the external surface for the Pd_{IW}/CMK-3 and Pd_{IMP}/CMK-3 catalysts, whereas in case of Pd_{PVA}/CMK-3 Pd NPs were only observed on the external surface. The hydrodynamic radius of the preformed particles in Pd_{PVA}/CMK-3 with the capping agent (PVA) present is preventing diffusion into the pores.[33] The number of Pd NPs on the external vs. internal support surface were counted after segmentation and the percentage of particles on the external surface is calculated based on several (3-7) tomograms of each Pd/CMK-3 catalyst to quantify the 3D distribution of the particles. Moreover, Pd loadings for individual Pd/CMK-3 tomogram were estimated from the volume of the segmented Pd NPs and the support volume. The results are summarized in Figure 4.7.

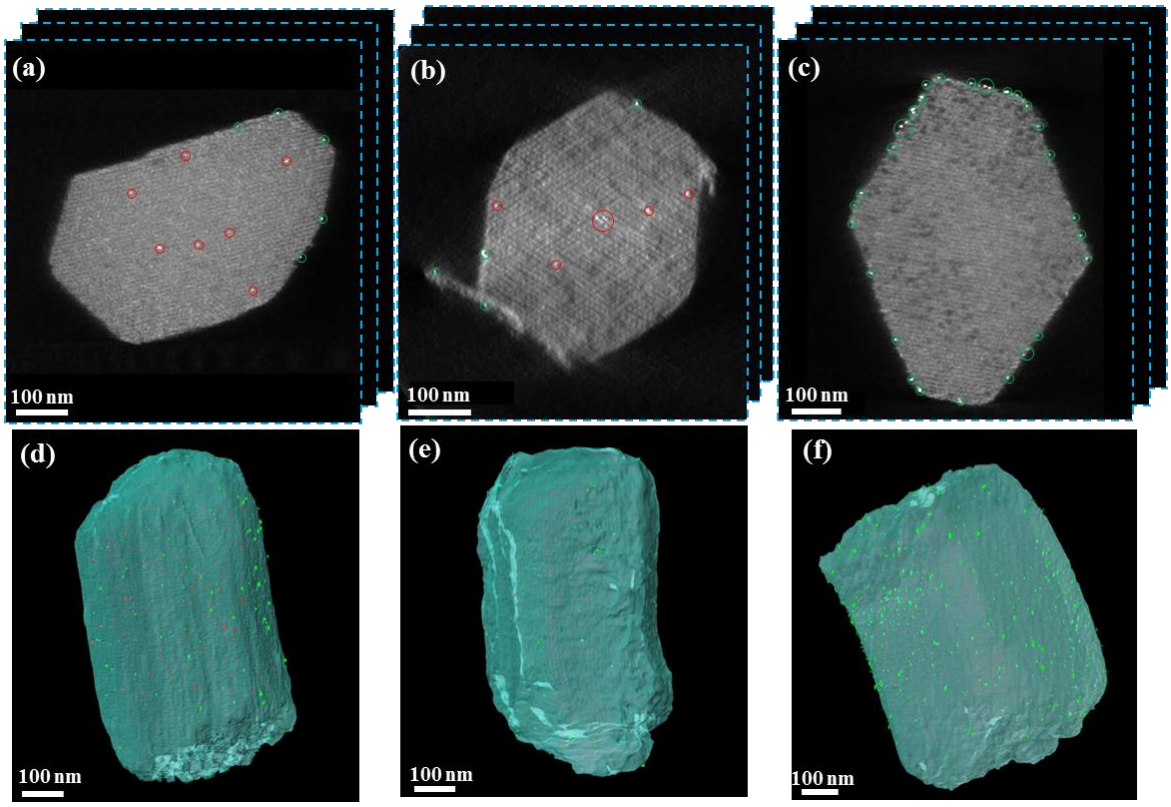

Figure 4.6: Typical 2D slices from the reconstructed volume of (a) Pd_{IW}/CMK-3, (b) Pd_{IMP}/CMK-3 and (c) Pd_{PVA}/CMK-3 and the corresponding representative 3D visualization (d-f). The green and red circles in a-c highlight Pd NPs on the external surface and inside of the porous support.

The relation between Pd loading and size of CMK-3 support is shown in Fig. 4.7a. The Pd loading is more or less uniform in large support pieces and varies slightly around the nominal loading of 1 wt.% in the three as-prepared catalysts. While the metal loading on small support pieces (~2×10^7 nm^3 or smaller) was considerably higher (>1 wt.%) in the as-prepared Pd_{IW}/CMK-3 and Pd_{IMP}/CMK-3 catalyst, which could be due to the fact that pores in small support pieces are easier to be completely filled by the Pd precursor and because of the higher contribution of the external surface. The Pd loading on small support pieces of Pd_{IW}/CMK-3 is particularly high. This may be the result of a faster filling with Pd precursor in case of incipient wetness impregnation due to the capillary forces,[11] while the Pd precursor during wet impregnation has sufficient time for diffusion if the Pd precursor is not too strongly bound resulting in a more homogeneous distribution of the NPs. The fraction of Pd NPs on the external surface for the three as-prepared Pd/CMK-3 catalysts is plotted with respect to the CMK-3 support volume in Fig. 4.7b. About 20%-30% of Pd NPs are located on the external support surface for as-prepared Pd_{IW}/CMK-3, almost independent to the size of the CMK-3 support, whereas in case of as-prepared Pd_{IMP}/CMK-3, the amount of Pd particles on the external surface roughly decreases with the increase of the CMK-3 support volume. For the as-prepared Pd_{PVA}/CMK-3, all Pd NPs are exclusively located on the external CMK-3 surface. As indicated in section 4.3.2, the area of the external surface and the surface area inside the pores were calculated from the segmented tomograms of pure CMK-3. To better evaluate the difference of the particle distribution for incipient wetness impregnation and wet impregnation preparation, the fraction of Pd particles located on the external surface is plotted against

the fraction of the external support surface (Fig. 4.7c). For Pd_{IMP}/CMK-3, the fraction of Pd NPs on the external surface is roughly proportional to the external surface fraction. This linear correlation indicates that during the impregnation process, the precursor solution has adequate time to reach the anchoring positions on both the external surface and the internal pore surfaces. However, the factor of ~2 between the external surface fraction and the Pd loading on the external surface indicates that Pd adsorption has a higher likelihood on the external surface compared to inside the pores. In the contrast, a similar fraction of the precursor solution is absorbed into the inside pores of the support and always leaves 20-30% on the external surface during incipient wetness preparation. By comparing the tomographic analysis of the three Pd/CMK-3 catalysts at the as-prepared state and after 6 cycles, the variation of the particle distribution during the catalytic reaction was detected (Fig. 4.7c/d). For Pd_{IW}/CMK-3 after 6 cycles, the fraction of Pd NPs on the external surface is almost independent of the external surface fraction of the support, similar to the as-prepared state. In case of Pd_{PVA}/CMK-3 catalyst, all Pd NPs are still located on the external surface of support material after reaction. However, during the reaction there are noticeable changes for the distribution of particles in Pd_{IMP}/CMK-3 catalyst. A lot more Pd NPs were located on the external support surface after 6 reaction cycles compared to the as-prepared material.

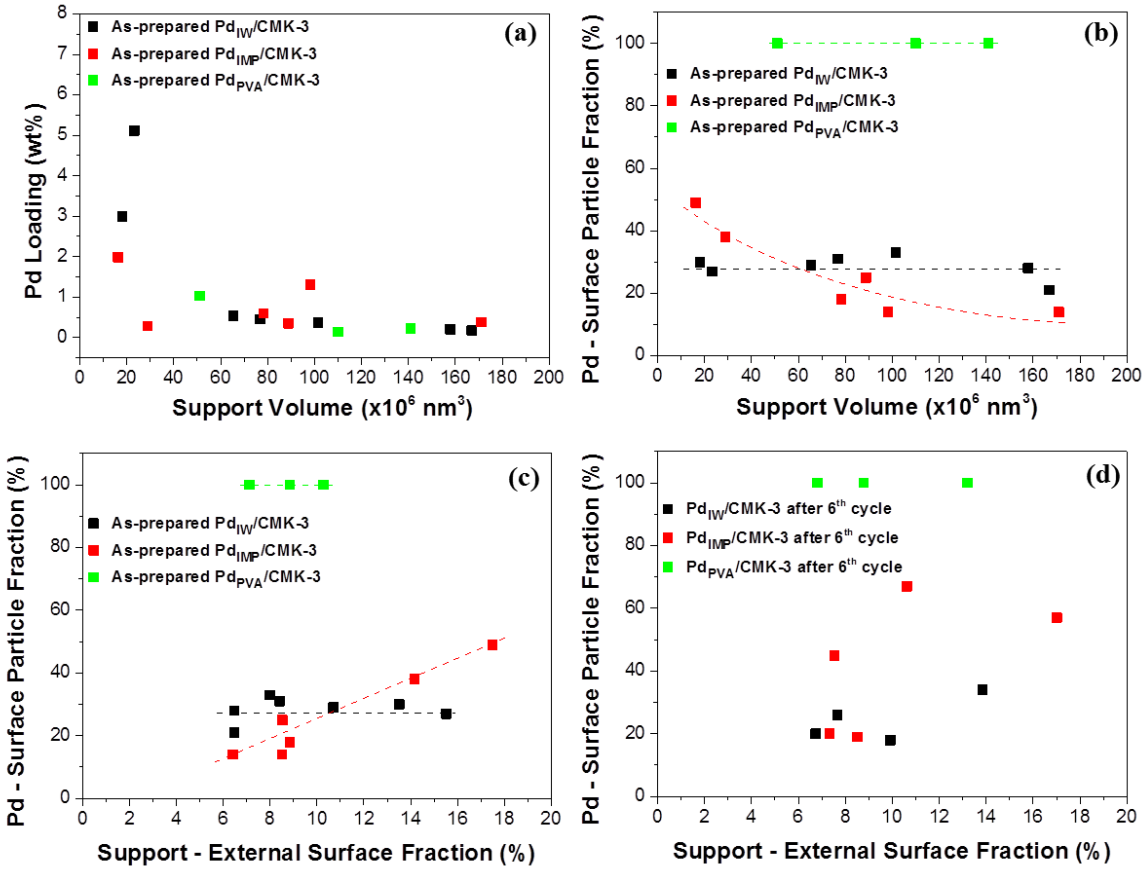

Figure 4.7: (a) The relation between Pd loading and volume of CMK-3 support, (b) fraction of Pd NPs on the surface as a function of the support volume in as-prepared Pd/CMK-3 catalysts, and (c) fraction of Pd NPs on the surface as a function of the external surface fraction of the support in Pd/CMK-3 catalysts in the as-prepared state and (d) after 6 cycles.

It can be estimated from Fig. 4.7b and 4.7c that the overall fraction of Pd particles on the external surface is comparable for as-prepared Pd_{IW}/CMK-3 and Pd_{IMP}/CMK-3 catalysts. This indicates that the high initial activity of Pd_{IMP}/CMK-3 is directly related to the surface particle fraction and the confinement effect of the pores. The metal-support interaction and the reaction pathways should also be taken into account, which will be discussed later. In Pd_{PVA}/CMK-3, residual PVA stabilizing agent on the Pd NPs might block some active sites[215] and resulted in the lower initial activity. A closer look at Fig 4.4b-d as well as Fig. 4.7b-c shows that the selectivity of furfural hydrogenation highly relates to the variation of the particle distribution of the three catalysts, especially for Pd_{IMP}/CMK-3. Previous studies[216–218] have indicated that the binding orientation of furfural on specific types of sites (terrace sites or edges/corners sites) of Pd NPs determines the selectivity in furfural hydrogenation. The formation of furfuryl alcohol is favored when furfural adsorbs with a perpendicular orientation on the Pd surface, whereas a flat-lying adsorption on the Pd surface is prone to the formation of tetrahydrofurfuryl alcohol.[217,219] In the presence of PVA on the Pd surface, a perpendicular adsorption of furfural is favored as a consequence of the interaction of the protecting agent with the NPs resulting in the formation of furfuryl alcohol.[219] On the free Pd NPs, both furfuryl alcohol and tetrahydrofurfuryl alcohol can be formed because perpendicular and flat furfural adsorptions are occurring without preference.[217] However, for the Pd NPs confined inside the small pores (3-4 nm) of the support, this can influence the reactant binding orientation, discouraging flat adsorption of the reactant molecules in favor of a perpendicular adsorption.[220] As a consequence, the formation of furfuryl alcohol but also of 2-methyl furan via hydrodeoxygenation (HDO) of furfuryl alcohol are favored.[218,220] Zhang et al. have shown a higher selectivity for methyl furan when Pd NPs are confined inside porous TiO_2 compared to a catalyst where Pd NPs are mainly present on the external surface.[220] A higher selectively for methyl furan via HDO of furfuryl alcohol for encapsulated Pd catalyst was observed due to the higher concentration of Pd-support interfacial sites. There should be a similar encapsulating effect in for Pd/CMK-3. In the course of the catalytic reaction cycles, the selectivity of Pd_{IW}/CMK-3 and Pd_{PVA}/CMK-3 catalysts remain unchanged (Fig. 4.4b/d), whereas the selectivity for tetrahydrofurfuryl alcohol increased from 24% in the 1st cycle to 36% in the 6th cycle (Fig. 4.4c) in case of Pd_{IMP}/CMK-3, while the selectivity of both furfuryl alcohol and 2-methyl furan decreased correspondingly. This selectivity change can be correlated with the increase of the fraction of Pd NPs on the external surface over the reaction cycles estimated from Fig. 4.7c-d. The cycling experiments agree with the mechanism suggested previously that Pd NPs confined inside fine pores lead to a higher selectivity for furfuryl alcohol and 2-methyl furan.

4.6. Stability of the Pd/CMK-3 catalysts

Stability is of great importance for any real application in catalysis. Metal NP growth causing a loss of active sites is a major reason for the deactivation of catalysts.[221] To evaluate the stability of the three catalysts, the structural changes of the recycled catalysts were investigated by HAADF-STEM. STEM images of the recycled catalysts and their NP size histograms are shown in Figure 4.8. The size

of Pd NPs in the recycled Pd_{IW}/CMK-3 and Pd_{PVA}/CMK-3 catalysts is almost unchanged compared to the as-prepared state, while the Pd NPs in Pd_{IMP}/CMK-3 grew during cycling.

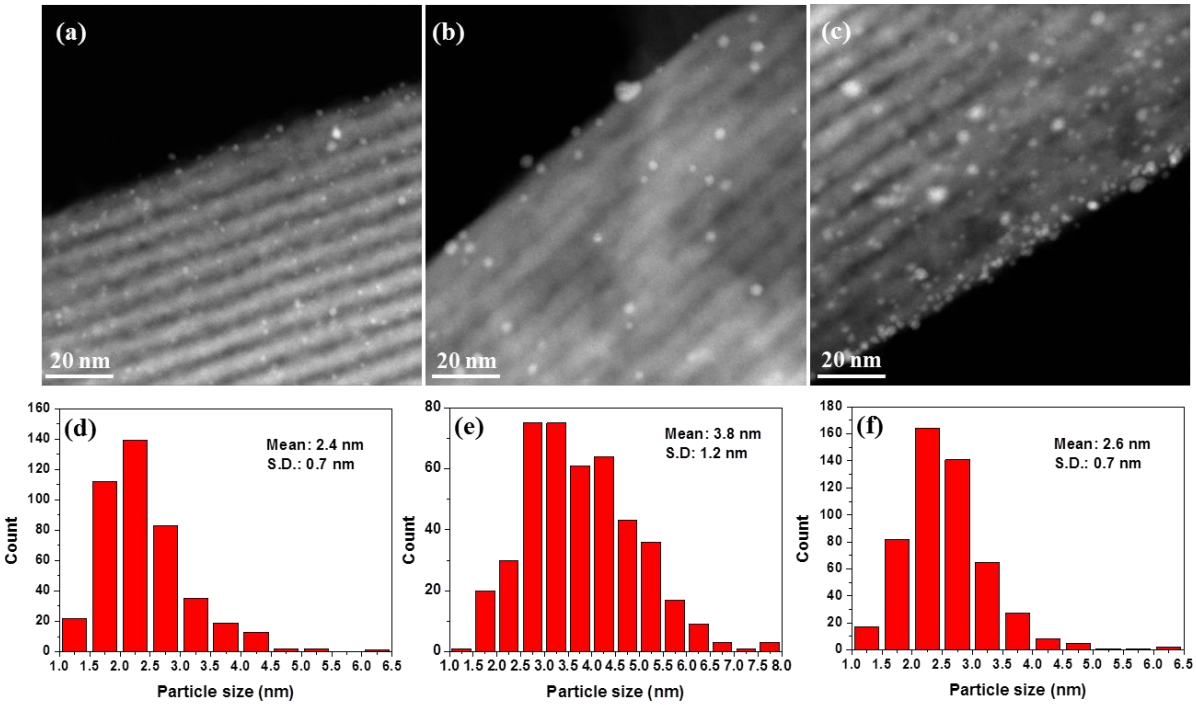

Figure 4.8: Representative STEM images of (a) Pd_{IW}/CMK-3, (b) Pd_{IMP}/CMK-3 and (c) Pd_{PVA}/CMK-3 after the 6th catalytic cycle and the corresponding particle size distribution histograms (d-f).

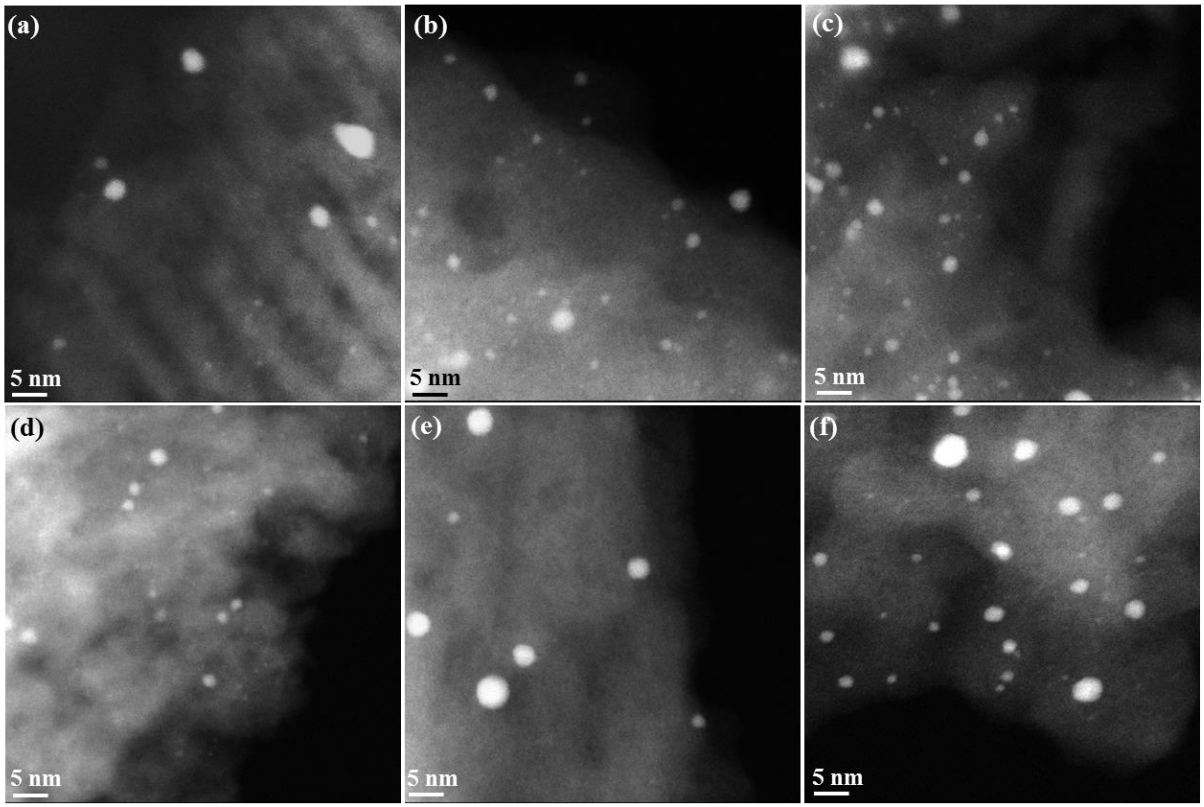

Figure 4.9: High-magnification STEM images of Pd_{IW}/CMK-3, Pd_{IMP}/CMK-3 and Pd_{PVA}/CMK-3 catalysts in the as-prepared state (a-c) and after 6th cycle (d-f).

To better understand the particles size changes, the three Pd/CMK-3 catalysts in the as-prepared state and after 6 cycles were investigated by higher magnification HAADF-STEM. As shown in Figure 4.9, some ultra-small Pd NPs (< 1 nm) were found in all three as-prepared Pd/CMK-3 catalysts (Fig. 4.9a-c). After reaction, those ultra-small Pd NPs almost disappeared in Pd_{IMP}/CMK-3 (Fig. 4.9e) but still remained in Pd_{IW}/CMK-3 and Pd_{PVA}/CMK-3 (Fig. 4.9d/f). Table 4.3 summarizes the average size of the Pd NPs measured from electron tomography (3D) and STEM images (2D) and the corresponding catalytic conversions in the 1st and the 6th run during furfural hydrogenation. The findings from electron tomography (3D) and STEM imaging indicated that the size of the Pd NPs in Pd_{IW}/CMK-3 and Pd_{PVA}/CMK-3 is almost unchanged after the reaction regardless of location, whereas Pd NPs obviously grew in Pd_{IMP}/CMK-3, especially the Pd NPs on the external surface.

Table 4.3: The conversions of Pd/CMK-3 catalysts used in 1st and 6th cycle of furfural hydrogenation reaction and Pd NP sizes in the as-prepared state and after 6th cycle reaction measured from electron tomography (3D) and STEM images (2D).

Catalysts	Conversion after 5h in 1st cycle	Conversion after 5h in 6th cycle	Average Pd NP size (nm)					
			Electron tomography (3D)				STEM (2D)	
			as-prepared		after 6th cycle		as-prepared	after 6th cycle
			Inside	External surface	Inside	External surface		
Pd_{IW}/CMK-3	64%	65%	2.4	2.9	2.3	2.9	2.4	2.4
Pd_{IMP}/CMK-3	88%	53%	2.6	2.9	3.7	4.6	2.6	3.8
Pd_{PVA}/CMK-3	98%	95%	-	2.7	-	2.8	2.5	2.6

Leaching and re-deposition during the reaction should be the main reason for the growth of the Pd NPs in Pd_{IMP}/CMK-3, where the leached Pd redeposited onto neighboring NPs and therefore results in an increasing size of NPs. As indicated in Fig. 4.9b/e, the ultra-small Pd NPs were mostly consumed, resulting in the quick drop of the activity of Pd_{IMP}/CMK-3 as shown in Fig. 4.4a/c. Moreover, both particle size and particle number on the external surface of Pd_{IMP}/CMK-3 catalyst increased considerably during cycling reaction. Both of them can be attributed to leaching of Pd, with redeposition of the leached Pd being more likely on the external surface. In this case, Ostwald ripening likely dominates the growth of NPs. On the outer surface the NPs enable to grow unrestrictedly and thus an increasing driving force for ripening, while growing of the NPs is confined inside the pores. The leaching was confirmed by AAS measurements of a "hot-filtrated" solution, adopted from literature[222,223]. The measurements indicate a significantly higher Pd leaching in case of Pd_{IMP}/CMK-3 as the Pd concentration measured was 3%, about 10 times higher compared to Pd_{IW}/CMK-3 and

Pd_{PVA}/CMK-3. The more prominent leaching of the wet impregnation prepared catalyst may be attributed to a weaker metal-support interaction, which also fits to the more uniform Pd loading and distribution in the as prepared Pd_{IMP}/CMK-3 catalyst as shown in Fig. 4.7. Previous studies[224,225] have indicated that the electrostatic interactions between the carbon surface and the active-phase precursors can be affected by the pH of the solution. During the preparation of the Pd/CMK-3 catalyst, the Pd precursor is dissolved in water and undergoes hydrolysis to form an acid. The amount of water used in wet impregnation is much more compared to incipient wetness impregnation. Therefore, a higher pH of the solution during wet impregnation weakened electrostatic interactions between the support CMK-3 and the Pd precursors, which could explain the evident Pd leaching and the lowest stability of Pd_{IMP}/CMK-3 catalyst.

4.7. Conclusions

Based on the quantitative tomographic analysis, the 3D distribution of Pd NPs in the three catalysts synthesized by incipient wetness impregnation, wet impregnation and sol immobilization was systematically investigated. About 20%-30% of Pd NPs are located on the external support surface for as-prepared Pd_{IW}/CMK-3, almost independent of the size of the CMK-3 support, whereas in case of as-prepared Pd_{PVA}/CMK-3, all Pd NPs are exclusively located on the external CMK-3 surface. For the as-prepared Pd_{IMP}/CMK-3, the Pd NP fraction on the external surface is roughly proportional to the ration of the external vs. internal surface, suggesting adequate time and mobility of the precursor to access the anchoring sites on the internal and external surfaces.

The observed structure and the catalytic tests indicate that the selectivity of these catalysts in furfural hydrogenation are highly correlated with the location of the particles. Pd NPs confined in the pores of the mesoporous carbon favored the formation of 2-methyl furan, probably due to encapsulating effects favoring a perpendicular orientation of furfural adsorbed on Pd and longer contact times. Therefore, when unprotected Pd NPs are on the external surface, the yield of tetrahydrofurfuryl alcohol becomes much higher. However, residual capping agent on Pd_{PVA}/CMK-3 slightly suppresses the formation of tetrahydrofurfuryl alcohol by reducing the probability of parallel adsorption binding to the Pd NPs surface and resulted in a high selectivity to furfuryl alcohol.

In addition, leaching depends on the synthesis and plays an important role with respect to catalytic stability. The low stability of Pd_{IMP}/CMK-3 could be attributed to a higher leaching rate due to weaker metal-support interaction, which was evidenced by the increasing particle size during the catalytic reaction.

Finally, it is worth to point out that the quantitative tomography analysis was key to characterize the structural differences and thus understand the differences in catalytic behavior depending on the synthetic methods used to prepare the catalyst. In turn, this information can be used to precisely design a catalysts for the desired product.

5. Correlation of the surface faceting of CeO_2 nanoparticles with their CO oxidation reactivity

5.1. Introduction

Ceria (CeO_2) NPs are extensively used both as catalyst and as support for noble metals in heterogeneous catalysis,[226–229] e.g. in three-way automotive exhaust catalysts, water gas shift reaction and oxidation of CO, etc.. This is due to its unique redox properties, where oxygen insertion or removal from a reactant can proceed by creation or annihilation of oxygen vacancies in the CeO_2 lattice without changing its face-centered cubic crystal structure.[230] Recently, many studies have aimed at improving the activity of CeO_2 based catalysts through the synthesis of nanostructured CeO_2 with controlled shapes such as rods[231–233], octahedral[234] and cubes[235]. The catalytic performance is highly related to the morphology of CeO_2 both with and without noble metal NPs loading.[236–238] For instance, Pt@CeO_2 rods mainly exhibiting of exposed {110} and {100} surfaces were found to be more active in CO oxidation compared to Pt catalysts supported on octahedral or cube shaped CeO_2 with {111} and {100} exposed facets, respectively.[239] In contrast, Agarwal et al. have demonstrated that CeO_2 cubes with exposed {100} facets were much more active for CO adsorption resulting in water gas shift activity compared to CeO_2 octahedral ({111}+{100}) and rods ({111}+{100}).[240] This illustrates that the catalytic activity of CeO_2 NPs strongly depends on their major exposed surfaces, which can be well controlled by the synthetic procedures. However, determination of the exposed surfaces in CeO_2 NPs was typically done based on 2D observations,[239–242] which is not necessarily sufficient because part of the characteristics of the 3D NPs remains ambiguous and a quantitative analysis is difficult.

In this chapter, the morphology of selected cube and rod shaped CeO_2 NPs is revealed both in 2D and in 3D by HRTEM, HAADF-STEM and electron tomography. The exposed surfaces for both types of CeO_2 NPs are precisely determined. Moreover, supported Pt catalysts based on these two types of CeO_2 NPs are investigated for their performance in CO oxidation. Correlating the exposed surfaces of CeO_2 NPs with the catalytic performance in CO oxidation contributes to understand the CO oxidation mechanism for CeO_2 based catalysts.

5.2. Experimental section

5.2.1. Ceria morphology synthesis

Ceria with different morphologies were prepared by a conventional hydrothermal synthesis as reported in literature[235] by Arik Beck in Jan-Dierk Grundwaldt's group at the Karlsruhe Institute of Technology. The hydrothermal synthesis was performed in pressure proof stainless steel autoclaves with inner Teflon vessels (Berghof). Depending on the desired morphology a certain amount of NaOH (cubes: 24 g, rods: 22 g) was dissolved in 120 mL of deionized H_2O and stirred for approximately 10 min. Cerium(III) nitrate hexa-hydrate $Ce(NO_3)_3 \cdot 6H_2O$ (Aldrich Chemistry) was added to the solution

(cubes: 620 mg, rods: 1,96 g) under continuous stirring. The mixture was transferred to the Teflon inlays of the steel autoclaves and heated to 180 °C (cubes) or 100 °C (rods) for 21 h.

5.2.2. N_2 physisorption

The specific surface area of the samples were evaluated by N_2 physisorption using the BET[189] method by Angela Beilmann in Jan-Dierk Grundwaldt's group at the Karlsruhe Institute of Technology. Prior to the measurements, the samples were pretreated under reduced pressure at 300 °C for 2 h (BELprep II, BEL Inc, Japan). The N_2 physisorption was performed at 77 K using a Belsorp II mini (Bell Inc., Japan). The surface area of the as-prepared CeO_2 rods and cubes are 92 m^2/g and 28 m^2/g, respectively.

5.2.3. Noble metal Pt loading

Platinum was loaded onto the ceria samples by incipient wetness impregnation by Arik Beck in Jan-Dierk Grundwaldt's group at the Karlsruhe Institute of Technology. Tetra ammine platinum(II) nitrate $[Pt(NH_3)_4](NO_3)_2$ (Alfa Aesar) was dissolved in highly purified water (Carl Roth GmbH + Co. KG) and added dropwise to the ceria powder until its pore volume was filled. The powder was then dried at 60 °C for several minutes. Further Pt-solution was added until the desired Pt loading was achieved (cubes: 1.0 wt.%, rods: 2.2 wt.%) to produce catalysts with a comparable particle loading per surface area of the CeO_2 support. The powder was finally calcined at 600 °C for 5 h. After impregnation with Pt and calcination, surface areas of the samples were rods (2.2 wt.%) with 68 m^2/g and cubes (1 wt.%) with 27 m^2/g, respectively.

5.2.4. Catalytic testing for CO oxidation

The activity for CO oxidation was evaluated in a transient manner (50 °C to 500 °C, 10 °C/min) using a plug flow reactor. The catalyst, diluted with 90% SiO_2, was pressed and sieved to a certain particle size of 125 – 250 µm. The weight hourly space velocity was adjusted for all catalysts to be 60,000 $L/g_{Pt}/h$, with the overall mass of catalysts corrected for the amount of Pt loading to achieve the similar amount of active metal for the catalytic tests. The temperature was monitored by two thermocouples at the inlet (T_{in}) and outlet (T_{out}) of the catalyst bed. The reaction gas mixture (1000 ppm CO, 10 % O_2, N_2 as balance) was dosed with mass flow controllers (Bronkhorst). The gas concentrations were analyzed with a Fourier transformed IR spectrometer (FTIR) at the reactor outlet. The reactor was heated in a light-off experiment from 50 to 600 °C in the reaction mixture (heating rate 10 °C/min). After 1 h at 600 °C, the reactor was cooled to 50 °C and the next light-off to 600 °C was performed. In the present work, the third light-off is referred to as "calcined". Subsequently the reactor was cooled to 250 °C and the gas mixture was switched to a reductive mixture (2 % CO balanced N_2) for 2 min, referred to as "reduced", to observe a possible catalytic activation. For this purpose, the gas inlet stream was switched with an electrically actuated valve (Vici) to a second gas line containing the reductive gases. Then, the gas inlet stream was switched to the reaction gases and was cooled to 50 °C. To monitor the activation a forth light-off was performed from 50 to 500 °C. The catalysts testing for

the CO oxidation were performed by Arik Beck and Florian Maurer at the Karlsruhe Institute of Technology.

5.2.5. Transmission electron microscopy and electron tomography

The CeO_2 and Pt/CeO_2 powder was dispersed on copper grids coated with holey carbon film (Quantifoil). The microstructure and morphology were investigated by HRTEM and HAADF-STEM using a FEI Titan 80-300 TEM operated at 300 kV. Analysis of HRTEM and HAADF-STEM images was carried out with Digital Micrograph (Gatan, version 1.71) and TEM Imaging & Analysis (TIA, version 4.7). The size of the supported Pt NPs in Pt/CeO_2 catalysts was estimated from HAADF-STEM images using the ImageJ[192] software approximating the particles with an elliptical shape. For electron tomography analysis, the CeO_2 cubes and rods samples and supported Pt/CeO_2-rod catalyst were dispersed on 100x400 mesh carbon coated copper grids (Quantifoil). For the CeO_2 cubes and rods samples, colloidal Au particles with size of 6.5 nm were deposited on the grid as markers afterwards, while in the case of supported Pt catalyst no gold markers were used, as the Pt particles are used as fiducial markers for tracking. Electron tomography was performed using a Fischione 2020 tomography holder on a Titan 80-300 microscope (FEI Company) operated at an acceleration voltage of 300 kV in STEM mode with a nominal beam diameter of 0.27 nm. HAADF-STEM tilt series with image dimensions of 2048x2048 pixels were collected using the Xplore3D software (FEI Company) over a tilt range of at least ±70°, with tilt increments of 2° or 3°. Alignment of the tilt series was performed with IMOD[191] using either Au colloidal particles or supported Pt NPs as fiducial markers. The aligned tilt-series was binned to 1024x1024 pixels to improve the signal-to-noise ratio and then reconstructed using SIRT implemented in Inspect3D 3.0 (FEI Company). The resulting tomograms had a final voxel size of 0.31 nm for cube-shape sample and of 0.24 nm for rod-shaped samples and the Pt/CeO_2-rod catalyst. Further analysis and visualization were performed in Amira 6.0 (FEI Company). Global thresholds were used to determine the volume of CeO_2 NPs in the median-filtered reconstruction volumes. The segmented NPs volumes were displayed by surface rendering. In case of Pt/CeO_2-rod catalyst, the Pt NPs were further determined by a manual segmentation to investigate their dispersion on the support.

5.3. Catalytic testing for CO oxidation

The catalytic activity of Pt NPs supported on rod and cube shaped ceria was evaluated for CO oxidation. The performance of both catalysts was tested directly after calcination and after a short reduction with CO at 250 °C. Such an activation has been reported in literature to enhance the CO oxidation activity.[243,244] The results of the CO oxidation tests are summarized in Figure 5.1: in the calcined state the cubic sample exhibits a higher CO oxidation activity than the rod shaped catalyst. The temperature for 50 % CO conversion (T_{50}), commonly reported in literature, is used to investigate the behavior of the catalysts. The difference in T_{50} is about 28 °C for the two calcined catalysts. In the reduced state this difference becomes less pronounced, but the cubic Pt/CeO_2 catalyst still reach the 50% CO conversion at lower temperatures compared to the rod-shaped one.

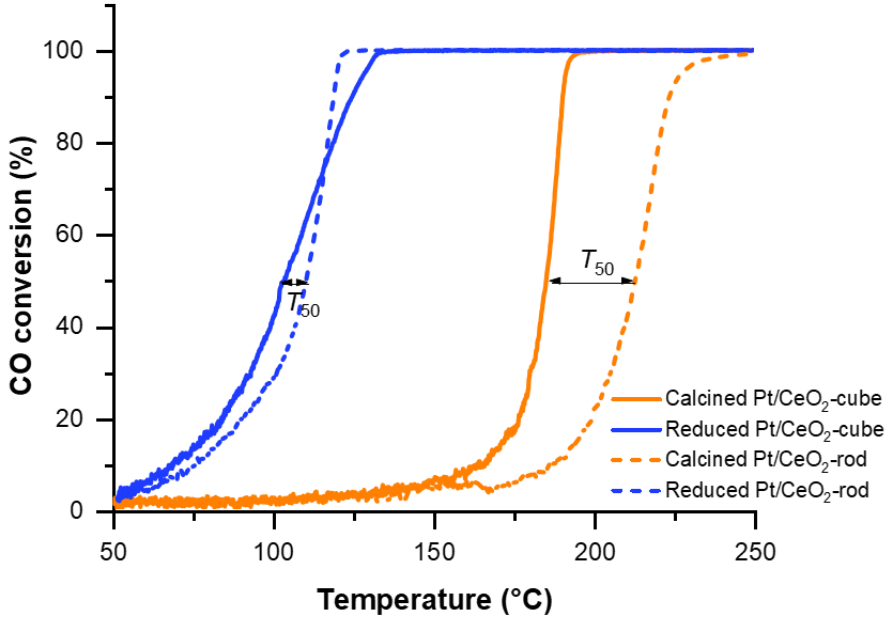

Figure 5.1: CO oxidation conversion with temperature of calcined and reduced Pt/CeO_2 catalysts.

5.4. Structural characterization of CeO_2 NPs and Pt/CeO_2 catalysts

To understand the difference in activity of Pt supported on rod and cube shaped CeO_2 for CO oxidation, the structure of CeO_2 and Pt/ CeO_2 catalysts was investigated in depth by various TEM techniques. First of all, the particle shape and the exposed crystallographic facets of the synthesized CeO_2 cubes and rods were determined by combining STEM, HRTEM and electron tomography. Fig. 5.2a presents a representative HAADF-STEM image of cubic CeO_2 NPs. Due to the single phase of CeO_2, the intensity in HAADF-STEM image is linearly proportional to the thickness along the electron beam propagation direction, given that absorption and scattering outside the HAADF detector can be neglected.[245] An analysis of the intensity across the image provides some first information on the shape of the NP. As illustrated in Fig. 5.2b, the intensity profile (as indicated in Fig. 5.2a) across the NP shows an almost constant thickness, in agreement with a cubic shape with both side facets parallel to the electron beam. The slight sharp drop of intensity at the edge indicates the presence of potential truncations. Exposed crystallographic facets of this cubic NP were further investigated by high-resolution HAADF-STEM and HRTEM images. Considering the line profile shown in Fig. 5.2b, the lattice fringes observed in both the HR-STEM (Fig. 5.2c) and the HRTEM (Fig. 5.2d) images reveal the presence of {100} facets as the main surface of the CeO_2 cubes. In addition, a truncation of the edges is clearly seen in Fig. 5.2a. The HRTEM (Fig. 5.2d/e) and HRSTEM (Fig. 5.2c) analysis reveals {110} facets at the edges of the cube. Moreover, it was observed that the size of cube shaped CeO_2 NPs is not uniform, as illustrated in Fig. 5.3a. Electron tomography was used to further confirm the shape of the cubic CeO_2 NPs within different size. The 3D surface rendering (Fig. 5.3b-d) of reconstructed CeO_2 NPs demonstrates that the NPs with the size range from 20 nm to 120 nm all have a similar cubic shape, indicating a uniform NP shape.

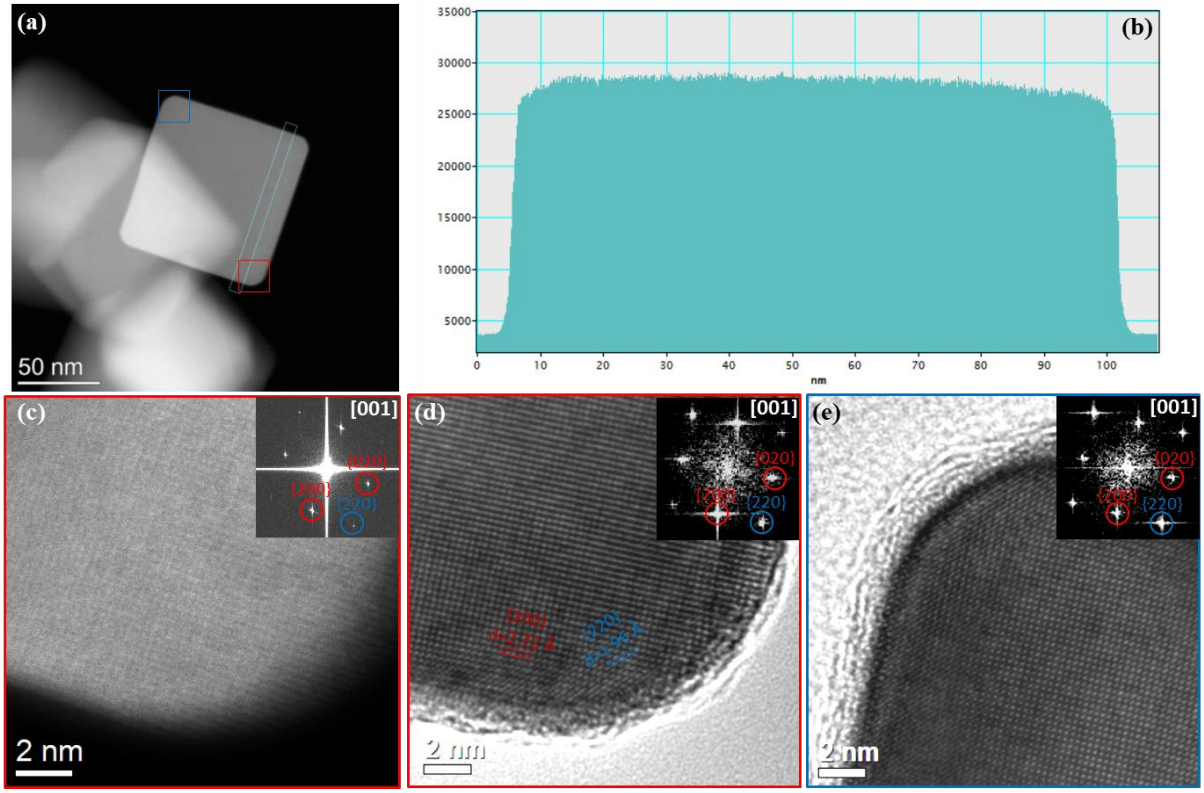

Figure 5.2: (a) STEM image, (b) the corresponding intensity profile of the highlighted areas in the STEM image, (c) HR-STEM image and (d-e) HRTEM images with the corresponding FFT of a cubic CeO_2 NP.

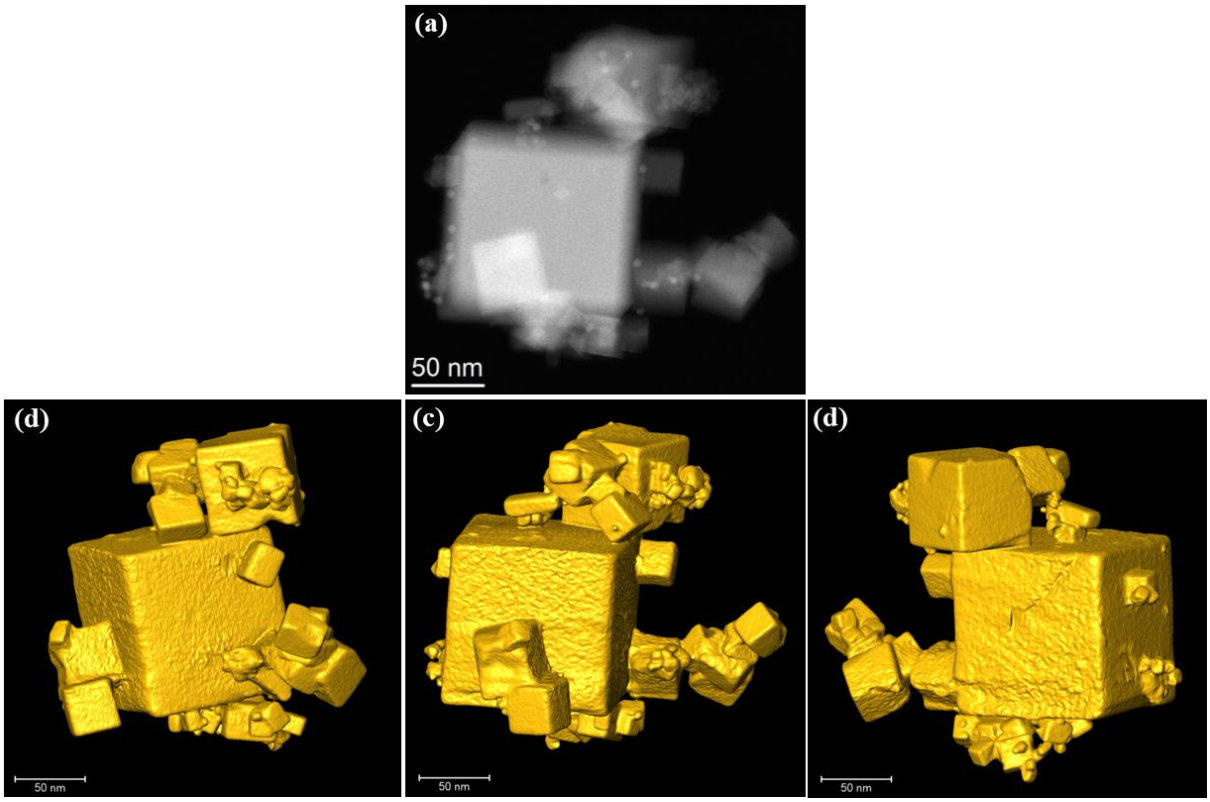

Figure 5.3: (a) a tilt-series STEM image at 0º (the small round shape NPs are the added Au NPs as tracking makers) and (b-d) 3D surface rendering of reconstructed cubic CeO_2 NPs at different views.

The structure of the rod-shaped CeO_2 NPs has been analyzed by classic 2D TEM and STEM, as illustrated in Figure 5.4. Fig. 5.4a presents a HAADF-STEM image acquired for the same CeO_2 rod sample as the one shown in the TEM image (Fig. 5.4d). Considering that the particle is oriented along the [1-10] zone axis, the intensity profile (Fig. 5.4c) along a line perpendicular to the rod axis (as shown in Fig. 5.4a/b) shows that its intensity varies along the profile, which may be attributed to a sloped facet in this orientation or a more complex thickness variation of the nanorod along the profile direction.[246] The corresponding HRTEM image (Fig. 5.4e) shows the presence of {111} crystallographic planes parallel to the long axis of CeO_2 rod. Nevertheless, the observed {111} planes can not be confirmed as the exposed facets from this 2D projection because of the complex thickness of the nanorod, which will be further discussed during the electron tomographic analysis. The {220} lattice observed perpendicular to the long axis in Fig. 5.4f indicates the growth direction of CeO_2 rod is along the [110] direction as also seen in the nanorod in Fig. 5.4e and reported in literature[231,235]. Different models for the exposed surfaces of CeO_2 nanorods have been proposed in previous studies. For examples, Agarwal et al. stated that the only prominent well-defined facets visible are the {111} surface,[240] whereas Mai et al.[235] and Zhou et al.[231] have proposed a rectangular cross section for the rods with exposed {110} and {001} surfaces. Another proposed morphology for CeO_2 rods is a multiply twinned structure with {111} crystallographic planes as the twin boundary.[247] The mechanism for the formation of such structures is likely dependent on the chemistry of cerium and the preparation procedures. However, it should be noted that the determination of exposed surfaces in these works was mainly based on 2D TEM or STEM images, which can be misleading.

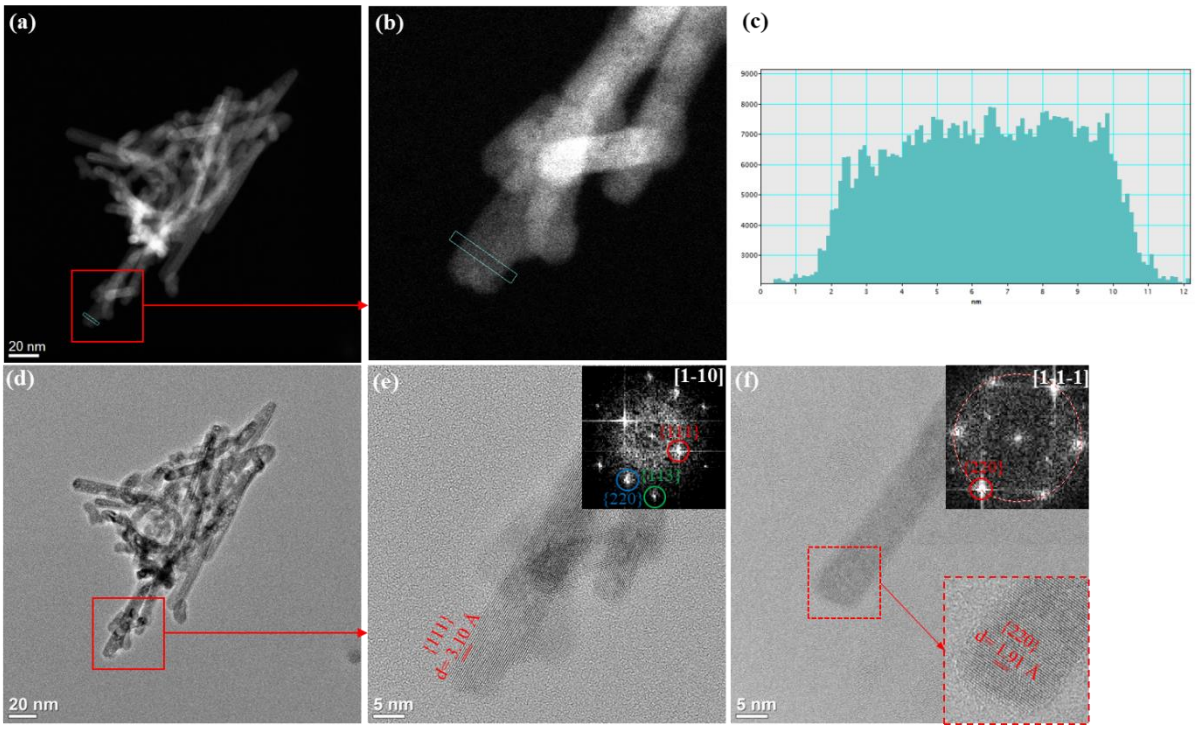

Figure 5.4: (a,b) (High magnification)-STEM images, (c) the corresponding intensity line profile of highlighted areas in STEM image and (d-f) (HR)-TEM images of rods CeO_2 NPs.

To uncover the structure of the rod-shaped CeO_2 NPs in this work, HAADF-STEM based electron tomography was used to determine the particle shape, surface crystallography and internal structure in 3D, as illustrated in Figure 5.5.

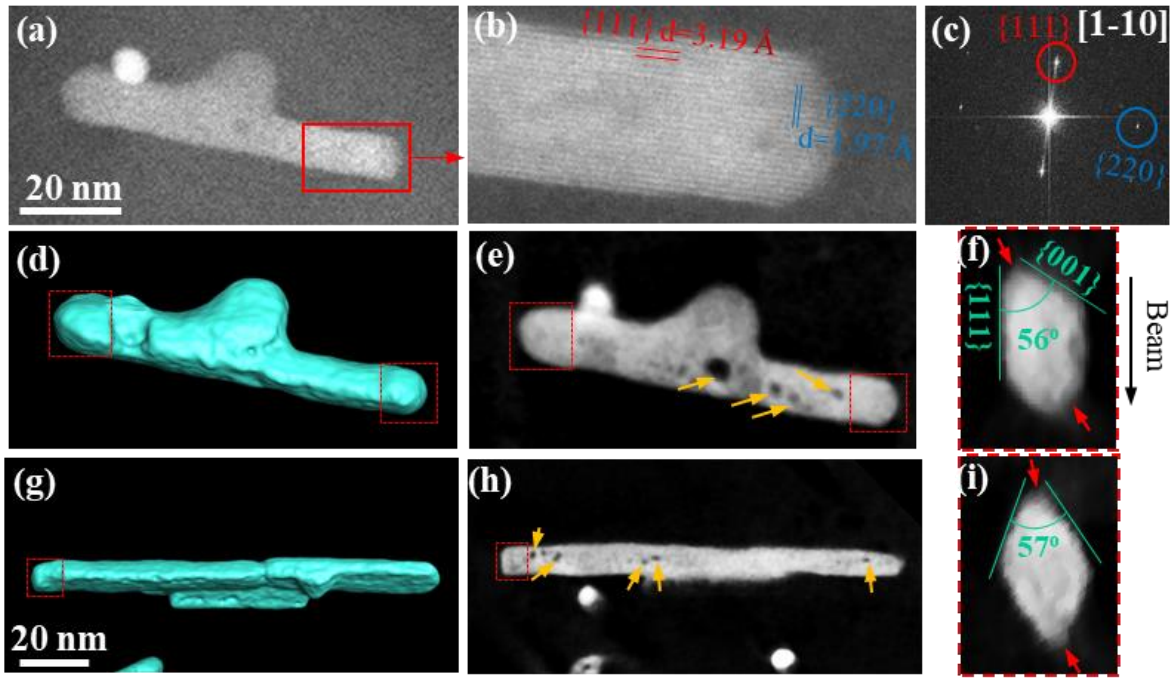

Figure 5.5: Electron tomographic analysis of rod shaped CeO_2 NPs: (a) a tilt-series STEM image at 0º, (b) the corresponding HR-STEM and (c) the corresponding FFT; (d) surface rendering of the 3D reconstruction, (e) the corresponding xy slice and (f) the slice perpendicular to the long axis of the rod; (g) the surface rendering of 3D reconstruction from another rod NP, (h) the corresponding xy slice and (i) the slice perpendicular to the long axis of this rod.

Fig. 5.5a presents a HAADF-STEM image at 0º from a tilt-series and the corresponding high-resolution STEM image (Fig. 5.5b) and the corresponding FFT (Fig. 5.5c) indicate {111} lattice planes paralleled to edge and {220} lattice planes along in long axis of this rod NP. Moreover, the presence of significant mesopores within the rods is revealed by the tomography as dark regions within the rods (indicated by yellow arrows) in the xy slice (Fig. 5.5e). The slice (Fig. 5.5f) perpendicular to the long axis of this NP shows that there are two main exposed facets at an angle of about 56°. Considering that the tilt-range is ±74° and the vertical plane in Fig. 5.5f (corresponding to the {111} facets in Fig. 5.5b) is parallel to electron beam, the missing wedge is not affecting any of the reconstructed facets as they are fully within the covered tilt-range. An electron tomographic analysis (Fig. 5.5g-i) of another rod shows the same cross-section. Based on the cubic crystallography, the three low indexed plans {100}, {110} and {111} have the lowest surface energy and the angle between {111} and {100} planes in a perfect cubic structure is 54.7°. With the currently obtained information in both 2D and 3D views, this confirms that the CeO_2 rods consist of two main exposed surfaces corresponding to the {111} and {100} crystallographic planes. In addition, some minor facets are observed in the slices perpendicular to the long axis of the rods (indicated by red arrows in Fig. 5.5f/i), but they are difficult to properly index

because they are affected by the missing wedge. When looking closely the rod in Fig. 5.5 a/b, one can recognize truncations at the front and back of the rod. However, further observations of other rods in 3D (highlighted parts in Fig. 5.5d/g) as well as the 2D projections in Fig. 5.7 suggest that these truncations are not uniform for all rods. However, quite often an asymmetric shape with a flat {220} facet on one side and a triangular front on the other side is observed.

The calcined and reduced Pt/CeO_2 catalysts were also investigated by STEM. As shown in Figure 5.6a/c, there are no detectable Pt NPs in the calcined Pt/CeO_2 catalysts, probably because the PtO_x species are too small to be detected in STEM. In contrast, the reduced catalysts show small Pt NPs (Fig. 5.6b/d) with an average size 0.8±0.2 nm for Pt/CeO_2-cube and 1.0±0.2 nm for Pt/CeO_2-rods. An electron tomographic analysis of a reduced Pt/CeO_2-rod catalyst is illustrated in Figure 5.7. The xy slice (Fig. 5.7b) and the surface rendering (Fig. 5.7c) from the 3D reconstructed volume show that the Pt NPs are found on both exposed surfaces of the rod, indicating a homogenous dispersion of the Pt NPs on the support.

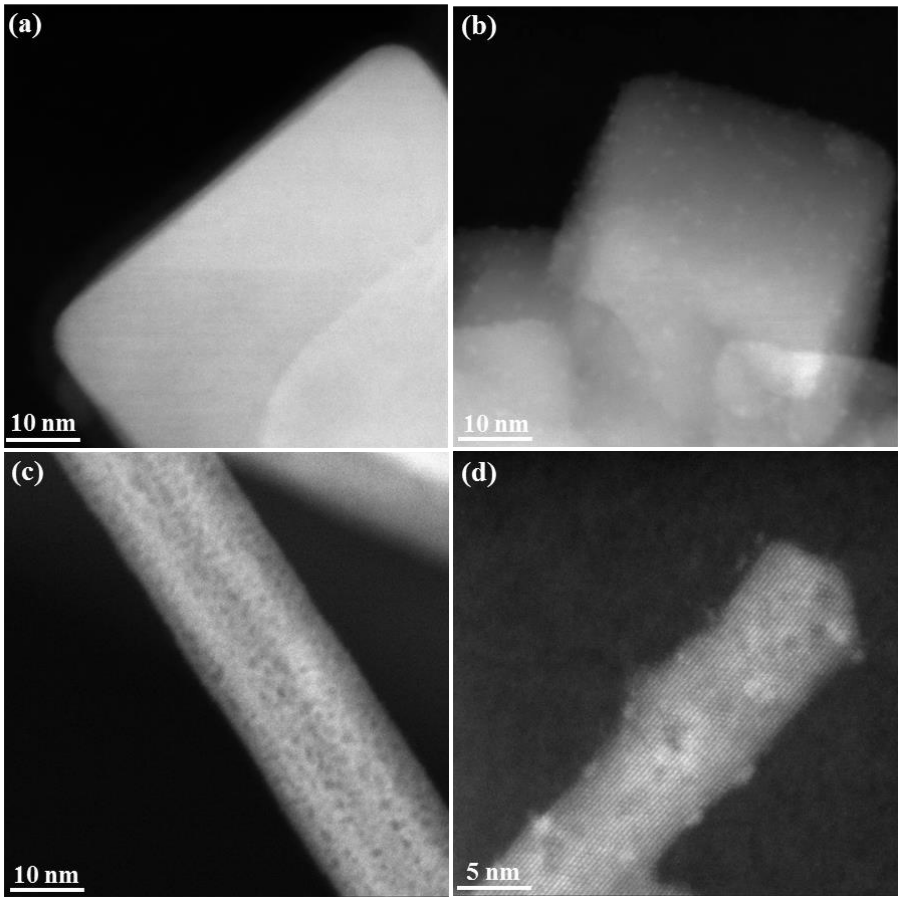

Figure 5.6: STEM images of (a,c) calcined and (b,d) reduced Pt/CeO_2 catalysts with cube/rods supports.

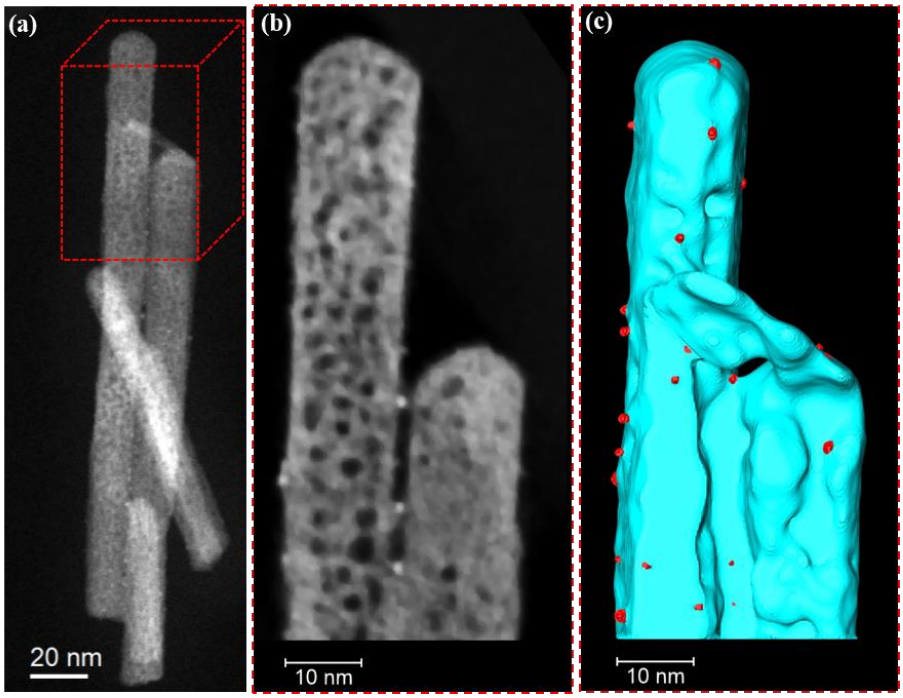

Figure 5.7: Electron tomographic analysis of the reduced Pt/CeO_2-rods catalyst: (a) a tilt-series STEM image at 0º, (b) the xy slice and (c) the surface rendering of 3D reconstruction in the cropped volume of a, indicating a homogenous dispersion of Pt NPs on the support.

5.5. Correlation of the CeO_2 exposed surfaces and the CO oxidation performance

CO oxidation over Pt/ceria is believed to proceed via the Mars van Krevelen mechanism.[248,249] The mechanism is depicted in Figure 5.8: CO is adsorbed on the surface of a Pt NP. By removal of oxygen from a ceria surface lattice and transfer to the Pt particle, CO is oxidized to CO_2.[250] The catalytic cycle is closed by subsequent annihilation of the vacancy by splitting oxygen from the gas phase.[226,231,251] In order to adsorb CO on the Pt NP, the Pt surface needs to be present in the reduced state. After calcination most of the Pt is presumably present as PtO_x and thus only very few adsorption sites are available. Upon reduction metallic Pt NPs are formed as observed in STEM. Therefore, more CO adsorption sites are available, increasing the catalytic activity after reduction. Following the CO adsorption on Pt, the removal of an oxygen atom from the ceria surface, i.e., formation of an oxygen vacancy, is the rate determinating step since the re-oxidation with O_2 is very facile for reduced ceria.[252] Theoretical works[253,254] suggested that the formation energy of the oxygen vacancy depends on the facet, following the sequence {110} < {100} < {111}, in which the formation energy of O vacancy on {110}, {100} and {111} facets are +1.99 eV, +2.27 eV and +2.60 eV, respectively. In this case, main exposed surfaces of cubic CeO_2 are {100} facets, whereas the rod-shaped CeO_2 support has two types of exposed surfaces: {111} and {100} facets. Thus, the Pt/CeO_2-cube catalysts in both calcined and reduced state exhibit higher CO oxidation activity compared to Pt/CeO_2-rod catalyst because of the lower formation energy of O vacancies on {100} surfaces.

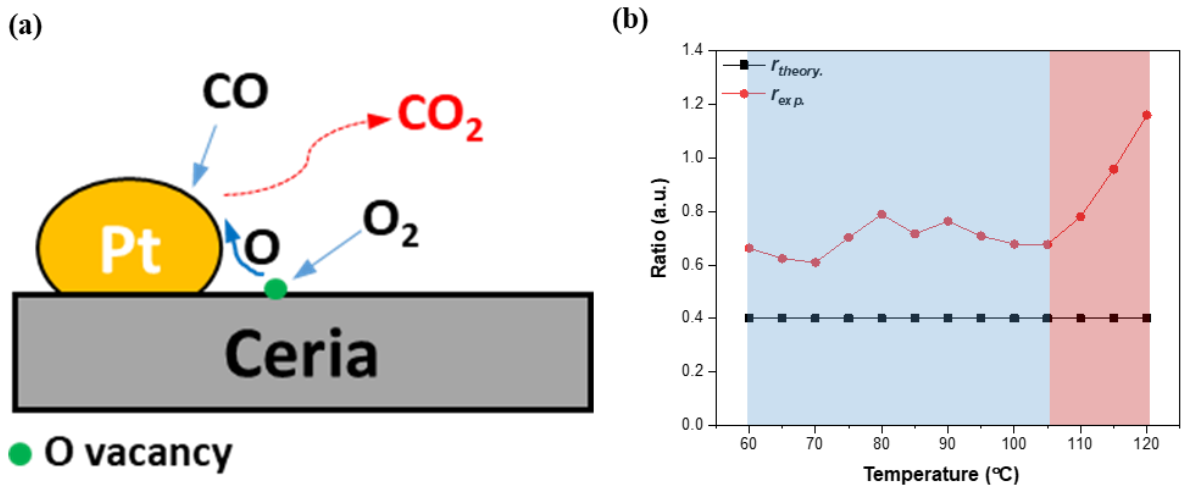

Figure 5.8: (a) Scheme of the CO oxidation on Pt/CeO_2 catalyst and (b) the theoretical ratio (r_{theory}) and the experimental ratio ($r_{exp.}$) of the rate constants between the reduced Pt/CeO_2-rod catalyst and the reduced Pt/CeO_2-cube catalyst with temperatures in CO oxidation.

To further evaluate the proposed mechanism of CO oxidation on Pt/CeO_2 catalyst (Fig. 5.8a), the relative reaction rate of Pt/CeO_2-cube and the Pt/CeO_2-rod are compared with the assumption that the oxygen vacancy formation is the only rate-determining step. The Arrhenius equation describes the temperature dependence of reaction rate,[255] thus the theoretical reaction rate (k) of the CO oxidation on CeO_2-based catalysts can be estimated from:

$$k = Ae^{\frac{-E_a}{k_B T}} \qquad (5\text{-}1)$$

where A is the frequency of collisions in the correct orientation, T is the absolute temperature, K_B is the Boltzmann constant and E_a is the activation energy for the reaction. Assuming that the frequency A is comparable for the different surfaces and using the theoretical values for the different activation energies with the experimentally determined facet contribution (~60% {111}, ~40% {100}) for the nanorods, 100% {100} for nanocubes) the relative rate r = k_{rod}/k_{cube} can be estimated ignoring contributions from minor facets:

$$r = \frac{60\%\, k(111)+40\%\, k(100)}{k(100)} = \frac{0.6\, e^{\frac{-2.60\ eV}{k_B T}} + 0.4\, e^{\frac{-2.27\ e}{k_B T}}}{e^{\frac{-2.27\ eV}{k_B T}}} = 0.6e^{\frac{-0.33\ eV}{k_B T}} + 0.4 \qquad (5\text{-}2)$$

As the exponential term in equation 5-2 is very small at the experimental temperatures, this means that essentially only the {100} facets are contributing at this temperature. The ratio of around 0.4 is reasonably close to the experimental difference at low CO conversion (the light blue region in Fig. 5.8b), which varies between 0.61 and 0.79 in the range of 60 °C to 105 °C (Fig. 5.8b). However, the even lower activation energy of the {110} and the minor {110} facets observed at the edge of the cubes would have to be considered. Even a tiny contribution would significantly alter the reaction ratio between cubes and rods. However, unfortunately, we can not measure the contribution the {110} facets in both types of CeO_2 crystals accurately enough. When the temperature increases, there is a cross-over of the CO

conversion at around 115°C for the reduced catalysts (Fig. 5.1), indicating that the reduced Pt/CeO_2-rod catalyst becomes more active compared to the reduced Pt/CeO_2-cube catalyst. This can also be seen by the increased ratio between the two experimental conversion rates in Fig. 5.8b at higher temperatures. This indicates that other factors become the rate limiting step in the catalytic conversion, potentially indicating a change in the reaction mechanism at higher temperatures.

5.6. Summary

The structure of two types of CeO_2 NPs: cubes and rods was analyzed both in 2D and 3D by HR-TEM and HAADF-STEM imaging and electron tomography. The CeO_2 cubes show a truncated cubic shape with {100} facets as the main surface and {110} facets at the cube edges. It is clearly confirmed that the rod-shaped CeO_2 NPs consist of two main exposed surfaces: {111} and {100} facets. The investigation of CO oxidation by these Pt/CeO_2 catalysts indicates that the activity is highly related to the exposed surfaces of the CeO_2 support. At low temperature CO oxidation, the Pt/CeO_2-cube catalysts exhibits higher activity for CO oxidation compared to the Pt/CeO_2-rod catalysts because of the lower formation energy of O vacancy within the {100} surface. A comparison of the rate constant of the reduced Pt/CeO_2-cube catalyst and the reduced Pt/CeO_2-rod catalyst based on theoretical activation energies and the experimental work confirms that the formation of the oxygen vacancy on the main exposed surfaces of CeO_2 is the rate determination step for CO oxidation. It should be noted that a precise determination of the exposed surfaces of CeO_2 NPs is of crucial importance to establish a correlation between the CO oxidation reactivity and their exposed surfaces. At higher temperatures, the relative reaction rates are changing indicating that the rate limiting step in the catalysis is changing.

6. Summary and outlook

Electron tomography has evolved greatly and became a powerful technique for imaging the 3D structure of materials with nanometer resolution. In this thesis, electron tomography has been pushed to provide quantitative 3D structural information regarding the morphology of the support and the distribution of the active particles for supported catalysts. This provided a deeper understanding for their structure-property relationship.

In chapter 3, it was found that quantifying morphology and diffusion properties of disordered mesoporous carbons depend strongly on the fidelity of the reconstruction and the segmentation approach, which are affected by pore variations and the missing wedge during tomography acquisition. The morphology of the pore structure in terms of geometry and topology is not significantly altered by the reconstruction, but the diffusion properties of mesoporous materials, one of the critical aspects to understand activity and selectivity in catalysis, was noticeably affected by artefacts introduced in the reconstruction and segmentation process. DART performed noticeably better compared to SIRT for reliably quantitative analysis of the pore structure.

Moreover, electron tomography was employed to quantify the 3D distribution of Pd NPs supported on a mesoporous carbon (CMK-3). The quantitative analysis clearly revealed the structural differences of Pd/CMK-3 catalysts synthesized by incipient wetness impregnation, wet impregnation and sol immobilization methods. This structural difference could be correlated to their catalytic behavior in liquid phase furfural hydrogenation. The selectivity of these catalysts were highly affected by the particle locations: more Pd NPs located in internal pores promote the formation of 2-methyl furan, whereas free particles on the external surface push the selectivity towards furfuryl alcohol and tetrahydrofurfuryl alcohol. In addition, differences in the adhesion of Pd desposited by incipient wetness and wet impregnation could be related to the uniformity of the Pd distribution and the stability of the catalyst.

In Chapter 5, electron tomography in combination with HRTEM and HAADF-STEM imaging revealed the exposed surfaces of CeO_2 NPs with cube and rod shapes both in 2D and in 3D. The cube CeO_2 NPs have the main exposed surface of {100} while the rod-shaped CeO_2 NPs consist of two main exposed surfaces with {111} and {100} facets. This contributed to clarify the higher activity of Pt/CeO_2-cube catalyst compared to the Pt/CeO_2-rods catalyst at low temperature CO oxidation. With the precise determination of exposed surfaces of CeO2 NPs the correlation between the CO oxidation reactivity and their exposed surfaces was established, which will contribute to design ceria particles applied into the exhaust gas stream.

In terms of future work, electron tomography can be employed to further investigate the complex structure of the disordered porous materials commonly used as supports because so far the application of electron tomography in heterogeneous catalysis are mainly focused on the ordered porous materials with the well-defined pore structure. Electron tomographic investigations on the disordered porous

materials will focus on two aspects: i) improving the reproducibility and reliability of electron tomography to deliver more fundamental insights into the local 3D structure; ii) building up the relationship between the 3D structural information of porous supports and the performance of supported catalysts. Moreover, the 3D distribution of supported NPs on the disordered porous materials within different synthesis methods will be interesting in combination with the work of Chapter 4. This can further provide fundamental insights into the relationship of supported NP location, porous networks and synthesis methods, which is the basis to control the NPs distribution to tune the catalysis to the desired product. On the other hand, the metal–support interaction in supported catalysts has a significant influence on the shape of supported NPs, which is typically investigated by HR-STEM and HRTEM with a 2D profile imaging. Electron tomography can be used to reveal the shape of supported NPs in 3D. The investigations can focus on the 3D shape of NPs located on the external and internal surfaces of supports, the relationship between the metal–support interactions and the shape of supported NPs as well as the evolution of the shape of supported NPs during catalytic cycling. The Pt/CeO_2 project will carry on to further understand the mechanism of CO oxidation with the collaboration of Prof. Grunwaldt group at Karlsruhe Institute of Technology: i) further investigating the rate limiting step of CO oxidation in higher temperature, e.g. the interface of Pt-ceria or the morphology of Pt NPs; ii) investigation on reduced behaviors of the PtO_x on the different surfaces of CeO_2 by a combination of TEM and X-ray absorption spectroscopy.

In addition, electron tomography in combination of the focused ion beam–scanning electron microscopy and synchrotron X–ray computed tomography could elucidate 3D structure of catalysts on the millimeter, micrometer and nanometer scales. This combination performed on the same sample can bridge 3D information in the different length scales to give a local and global understanding for catalysis.

All of these will give a 3D insight on the structure-property of supported catalysts and contribute to achieve the goal of designing and optimizing catalysts with desired performances.

Curriculum Vitae

Personal Information:

Name: Wu Wang

Date of Birth: September 25, 1988

Place of Birth: Shaodong, Hunan, China

Nationality: P.R. China

Education:

- *Doctoral studies* in Materials Science 09.2014-03.2019
  Joint Research Laboratory for Nanomaterials, Technische Universität Darmstadt and Karlsruhe Institute of Technology, Germany
  Title of Ph.D. thesis: "Quantitative 3D Structure Studies of Supported Catalysts at the Nanoscale" supervised by Prof. Dr.-Ing. Horst Hahn and Dr. Christian Kübel
- *Master of Engineering (M.E.)* in Materials Processing Engineering 09.2011–06.2014
  Department of Materials Science and Engineering, Shanghai University, Shanghai, China
  Title of Master's thesis: "Martensitic Transformation and Magnetic Properties of Ni-Mn-Sn(Co) Magnetocaloric Ribbons" supervised by Associate Prof. Hongxing Zheng
- *Bachelor of Engineering* in Materials Science and Engineering 09.2007–07.2011
  Department of Materials Science and Engineering, Central South University, Changsha, China

Scholarships & Awards:

- China Scholarship Council (CSC) scholarship for PhD research at Germany 09.2014- 09. 2018
- National Scholarship for Outstanding Graduate Students in China 11.2013

List of publications

Submitted

1. **Wang, W.,** Svidrytski, A., Wang, D., Villa, A., Hahn, H., Tallarek, U. and Kübel, C., Quantifying morphology and diffusion properties from high fidelity 3D reconstructions of mesoporous carbon, Microscopy and Microanalysis, **2019**. (**Revised**)

Published

1. Stucchi, M., Cattaneo, S., Cappella, A., **Wang, W.**, Wang, D., Villa, A. and Prati, L., Catalytic oxidation of methoxy substituted benzyl alcohols as model for lignin derivatives valorisation. Catalysis Today, **2019**, https://doi.org/10.1016/j.cattod.2019.03.022.
2. Testolin, A., Cattaneo, S., **Wang, W.,** Wang, D., Pifferi, V., Prati, L., Falciola, L. and Villa, A., Cyclic voltammetry characterization of Au, Pd, and AuPd nanoparticles supported on different carbon nanofibers. Surfaces, **2019**, *2*, 205-215.
3. Reich, S. J., Svidrytski, A., Höltzel, A., **Wang, W.**, Kübel, C., Hlushkou, D. and Tallarek, U., Transport under confinement: hindrance factors for diffusion in core-shell and fully porous particles with different mesopore space morphologies. Microporous and Mesoporous Materials, **2019**, 282:188-196.
4. **Wang, W.**, Villa, A., Kübel, C., Hahn, H. and Wang, D., Tailoring the 3D structure of Pd nanocatalysts supported on mesoporous carbon for furfural hydrogenation. ChemNanoMat, **2018**, 4(11): 1125-1132. (**Highlighted in front cover**)
5. Reich, S. J., Svidrytski, A., Höltzel, A., Florek, J., Kleitz, F., **Wang, W.**, Kübel, C., Hlushkou, D. and Tallarek, U., Hindered diffusion in ordered mesoporous silicas: insights from pore-scale simulations in physical reconstructions of SBA-15 and KIT-6 silica. The Journal of Physical Chemistry C, **2018**, 122(23):12350-12361.
6. Trampert, P., **Wang, W.**, Chen, D., Ravelli, R., Dahmen, T., Peters, P., Kübel, C. and Slusallek, P., Exemplar-based inpainting as a solution to the missing wedge problem in electron tomography. Ultramicroscopy, **2018**, 191:1-10.
7. Fam, Y., Sheppard, T. L., Diaz, A., Scherer, T., Holler, M., **Wang, W.**, Wang, D., Brenner, P., Wittstock, A. and Grunwaldt, J. D., Correlative multiscale 3D imaging of a hierarchical nanoporous gold catalyst by electron, ion and X-ray nanotomography. ChemCatChem, **2018**, 10(13):2858-2867.
8. Tofighi, G., Gaur, A., Doronkin, D. E., Lichtenberg, H., **Wang, W.**, Wang, D., Rinke, G., Ewinger, A., Dittmeyer, R. and Grunwaldt, J. D., Microfluidic synthesis of ultrasmall AuPd nanoparticles with a homogeneously mixed alloy structure in fast continuous flow for catalytic applications. The Journal of Physical Chemistry C, **2018**, 122(3):1721-1731.
9. Mutz, B., Sprenger, P., **Wang, W.**, Wang, D., Kleist, W. and Grunwaldt, J. D., Operando raman spectroscopy on CO_2 methanation over alumina-Supported Ni, Ni_3Fe and $NiRh_{0.1}$ catalysts: role of carbon formation as possible deactivation pathway. Applied Catalysis A: General, **2018**, 556:160-

171.

10. Tofighi, G., Lichtenberg, H., Pesek, J., Sheppard, T. L., **Wang, W.**, Schöttner, L., Rinke, G., Dittmeyer, R. and Grunwaldt, J. D., Continuous microfluidic synthesis of colloidal ultrasmall gold nanoparticles: in situ study of the early reaction stages and application for catalysis. Reaction Chemistry & Engineering, **2017**, 2(6):876-884.
11. Mutz, B., Belimov, M., **Wang, W.**, Sprenger, P., Serrer, M. A., Wang, D., Pfeifer P., Kleist W. and Grunwaldt, J. D., Potential of an alumina-supported Ni_3Fe catalyst in the methanation of CO_2: impact of alloy formation on activity and stability. ACS Catalysis, **2017**, 7(10):6802-6814.
12. Boscagli, C., Yang, C., Welle, A., **Wang, W.**, Behrens, S., Raffelt, K. and Grunwaldt, J.D., Effect of pyrolysis oil components on the activity and selectivity of nickel-based catalysts during hydrotreatment. Applied Catalysis A: General, **2017**, 544:161-172.
13. Dietrich, C., Schild, D., **Wang, W.**, Kübel, C. and Behrens, S., Bimetallic Pt/Sn-based nanoparticles in ionic liquids as nanocatalysts for the selective hydrogenation of cinnamaldehyde. Zeitschrift für anorganische und allgemeine Chemie, **2017**, 643(1):120-129.
14. Campisi, S., Ferri, D., Villa, A., **Wang, W.**, Wang, D., Kröcher, O. and Prati, L., Selectivity control in palladium-catalyzed alcohol oxidation through selective blocking of active sites. The Journal of Physical Chemistry C, **2016**, 120(26):14027-14033.
15. Villa, A., Freakley, S. J., Schiavoni, M., Edwards, J. K., Hammond, C., Veith, G. M., **Wang, W.**, Wang, D. and Hutchings, G. J., Depressing the hydrogenation and decomposition reaction in H_2O_2 synthesis by supporting AuPd on oxygen functionalized carbon nanofibers. Catalysis Science & Technology, **2016**, 6(3):694-697.
16. Rossetti, I., Villa, A., Compagnoni, M., Prati, L., Ramis, G., Pirola, C., Bianchi C. L., **Wang, W.** and Wang, D., CO_2 photoconversion to fuels under high pressure: effect of TiO_2 phase and of unconventional reaction conditions. Catalysis Science & Technology, **2015**, 5(9), 4481-4487.

References

[1] M. Sankar, N. Dimitratos, P. J. Miedziak, P. P. Wells, C. J. Kiely, G. J. Hutchings, *Chem. Soc. Rev.* **2012**, *41*, 8099.

[2] R. Schlögl, *Angew. Chemie - Int. Ed.* **2015**, *54*, 3465–3520.

[3] K. P. De Jong, J. W. Geus, *Catal. Rev. - Sci. Eng.* **2000**, *42*, 481–510.

[4] K.P. de Jong., *Wiley –VCH* **2009**, 401.

[5] V. Subramanian, **2015**.

[6] H. Schulz, *Appl. Catal. A Gen.* **1999**, *186*, 3–12.

[7] H. Mahmoudi, M. Mahmoudi, O. Doustdar, H. Jahangiri, A. Tsolakis, S. Gu, M. LechWyszynski, *Biofuels Eng.* **2017**, *2*, 11–31.

[8] G. Mamba, A. Mishra, *Catalysts* **2016**, *6*, 79.

[9] M. Shrimali, K. P. Singh, *Environ. Pollut.* **2001**, *112*, 351–359.

[10] J. Mo, Y. Zhang, Q. Xu, J. J. Lamson, R. Zhao, *Atmos. Environ.* **2009**, *43*, 2229–2246.

[11] P. Munnik, P. E. De Jongh, K. P. De Jong, *Chem. Rev.* **2015**, *115*, 6687–6718.

[12] A. T. Bell, *Science* **2003**, *299*, 1688–91.

[13] H. Cramr, H. Wold, *J. London Math. Soc.* **1936**, *s1-11*, 290–294.

[14] D. J. De Rosier, A. Klug, *Nature* **1968**, *217*, 130–134.

[15] R. G. Hart, *Science (80-.).* **1968**, *159*, 1464–1467.

[16] A. Cho, *Science (80-.).* **2003**, *299*, 1684.

[17] B. R. Cuenya, *Thin Solid Films* **2010**, *518*, 3127–3150.

[18] U. Heiz, E. L. Bullock, *J. Mater. Chem.* **2004**, *14*, 564–577.

[19] T. V. Choudhary, D. W. Goodman, *Appl. Catal. A Gen.* **2005**, *291*, 32–36.

[20] N. Lopez, T. V. W. Janssens, B. S. Clausen, Y. Xu, M. Mavrikakis, T. Bligaard, J. K. Nørskov, *J. Catal.* **2004**, *223*, 232–235.

[21] S. Back, M. S. Yeom, Y. Jung, *ACS Catal.* **2015**, *5*, 5089–5096.

[22] M. Haruta, *J. NEW Mater. Electrochem. Syst.* **2004**, *7*, 163–172.

[23] J. Liu, *Microsc. Microanal.* **2004**, *10*, 55–76.

[24] M. Chen, D. Kumar, C. W. Yi, D. W. Goodman, *Science (80-.).* **2006**, *311*, 291–293.

[25] D. M. Alonso, S. G. Wettstein, J. a. Dumesic, *Chem. Soc. Rev.* **2012**, *41*, 8075–8098.

[26] D. Wang, A. Villa, D. Su, L. Prati, R. Schlögl, *ChemCatChem* **2013**, *5*, 2717–2723.

[27] D. I. Enache, J. K. Edwards, P. Landon, B. Solsona-Espriu, A. F. Carley, A. A. Herzing, M. Watanabe, C. J. Kiely, D. W. Knight, G. J. Hutchings, *Science (80-.).* **2006**, *311*, 362–365.

[28] H. F. Rase, *Handbook of Commercial Catalysts: Heterogeneous Catalysts*, **2000**.

[29] S. Nishimura, *Handbook of Heterogeneous Catalytic Hydrogenation for Organic Synthesis*, **2001**.

[30] Y. Yürüm, A. Taralp, T. N. Veziroglu, *Int. J. Hydrogen Energy* **2009**, *34*, 3784–3798.

[31] Y. Yang, K. Chiang, N. Burke, *Catal. Today* **2011**, *178*, 197–205.

[32] G. Prieto, M. Shakeri, K. P. De-Jong, P. E. De-Jong, *ACS Nano* **2014**, *2522–2531*.

[33] A. Villa, D. Wang, C. E. Chan-Thaw, S. Campisi, G. M. Veith, L. Prati, *Catal. Sci. Technol.* **2016**, *6*, 598–601.

[34] J. P. Tessonnier, L. Pesant, G. Ehret, M. J. Ledoux, C. Pham-Huu, *Appl. Catal. A Gen.* **2005**, *288*, 203–210.

[35] H. Ma, L. Wang, L. Chen, C. Dong, W. Yu, T. Huang, Y. Qian, *Catal. Commun.* **2007**, *8*, 452–456.

[36] X. Pan, X. Bao, *Acc. Chem. Res.* **2011**, *44*, 553–562.

[37] C. Wu, L. Dong, J. Onwudili, P. T. Williams, J. Huang, *ACS Sustain. Chem. Eng.* **2013**, *1*, 1083–1091.

[38] G. Öhlmann, *Zeitschrift für Phys. Chemie* **1999**, *208*, 274–278.

[39] J. D. Grunwaldt, J. B. Wagner, R. E. Dunin-Borkowski, *ChemCatChem* **2013**, *5*, 62–80.

[40] M. Kruk, M. Jaroniec, A. Sayari, *Langmuir* **1997**, *13*, 6267–6273.

[41] R. Schlögl, *Adv. Catal.* **2009**, *52*, 273–338.

[42] M. Kruk, M. Jaroniec, A. Sayari, *Langmuir* **1997**, *13*, 6267–6273.

[43] I. E. Wachs, in *Catal. Today*, Elsevier, **2005**, pp. 79–94.

[44] J. F. Haw, *In-Situ Spectroscopy in Heterogeneous Catalysis*, Wiley-VCH Verlag GmbH & Co. KGaA, Weinheim, FRG, **2002**.

[45] J. V. Lauritsen, R. T. Vang, F. Besenbacher, *Catal. Today* **2006**, *111*, 34–43.

[46] F. Besenbacher, M. Brorson, B. S. Clausen, S. Helveg, B. Hinnemann, J. Kibsgaard, J. V. Lauritsen, P. G. Moses, J. K. Nørskov, H. Topsøe, *Catal. Today* **2008**, *130*, 86–96.

[47] J. C. Yang, M. W. Small, R. V. Grieshaber, R. G. Nuzzo, *Chem. Soc. Rev.* **2012**, *41*, 8179.

[48] W. Zhou, I. E. Wachs, C. J. Kiely, *Curr. Opin. Solid State Mater. Sci.* **2012**, *16*, 10–22.

[49] D. S. Su, B. Zhang, R. Schlögl, *Chem. Rev.* **2015**, *115*, 2818–2882.

[50] B. Zhang, D. S. Su, *ChemCatChem* **2015**, *7*, 3598–3600.

[51] M. Haider, S. Uhlemann, E. Schwan, H. Rose, B. Kabius, K. Urban, *Nature* **1998**, *392*, 768–769.

[52] K. Sohlberg, T. J. Pennycook, W. Zhou, S. J. Pennycook, *Phys. Chem. Chem. Phys.* **2015**, *17*, 3982–4006.

[53] A. K. Datye, D. J. Smith, *Catal. Rev.* **1992**, *34*, 129–178.

[54] A. A. Herzing, C. J. Kiely, A. F. Carley, P. Landon, G. J. Hutchings, *Science (80-.).* **2008**, *321*, 1331–1336.

[55] J. A. Lopez-Sanchez, N. Dimitratos, C. Hammond, G. L. Brett, L. Kesavan, S. White, P. Miedziak, R. Tiruvalam, R. L. Jenkins, A. F. Carley, et al., *Nat. Chem.* **2011**, *3*, 551–556.

[56] W. Zhou, J. M. Thomas, *Curr. Opin. Solid State Mater. Sci.* **2001**, *5*, 75–83.

[57] T. Akita, K. Tanaka, M. Kohyama, M. Haruta, *Surf. Interface Anal.* **2008**, *40*, 1760–1763.

[58] N. Shibata, A. Goto, K. Matsunaga, T. Mizoguchi, S. D. Findlay, T. Yamamoto, Y. Ikuhara, *Phys. Rev. Lett.* **2009**, *102*, 136105.

[59] L. Shao, B. Zhang, W. Zhang, S. Y. Hong, R. Schlögl, D. S. Su, *Angew. Chemie - Int. Ed.* **2013**, *52*, 2114–2117.

[60] M. Cargnello, M. Cargnello, V. V. T. Doan-nguyen, T. R. Gordon, R. E. Diaz, E. A. Stach, R. J. Gorte, P. Fornasiero, C. B. Murray, *Science (80-.).* **2013**, *341*, 771–774.

[61] S. Hannemann, J. D. Grunwaldt, P. Lienemann, D. Günther, F. Krumeich, S. E. Pratsinis, A. Baiker, *Appl. Catal. A Gen.* **2007**, *316*, 226–239.

[62] D. Wang, A. Villa, P. Spontoni, D. S. Su, L. Prati, *Chem. - A Eur. J.* **2010**, *16*, 10007–10013.

[63] T. R. Johns, J. R. Gaudet, E. J. Peterson, J. T. Miller, E. A. Stach, C. H. Kim, M. P. Balogh, A. K. Datye, *ChemCatChem* **2013**, *5*, 2636–2645.

[64] C. Jeyabharathi, N. Hodnik, C. Baldizzone, J. C. Meier, M. Heggen, K. L. N. Phani, M. Bele, M. Zorko, S. Hocevar, K. J. J. Mayrhofer, *ChemCatChem* **2013**, *5*, 2627–2635.

[65] C. Cui, L. Gan, M. Heggen, S. Rudi, P. Strasser, *Nat. Mater.* **2013**, *12*, 765–771.

[66] W. Hoppe, R. Langer, G. Knesch, C. Poppe, *Naturwissenschaften* **1968**, *55*, 333–336.

[67] C. Kübel, D. Niemeyer, R. Cieslinski, S. Rozeveld, *Mater. Sci. Forum* **2010**, *638–642*, 2517–2522.

[68] H. Friedrich, P. E. De Jongh, A. J. Verkleij, K. P. De Jong, *Chem. Rev.* **2009**, *109*, 1613–1629.

[69] G. Möbus, B. J. Inkson, *Mater. Today* **2007**, *10*, 18–25.

[70] C. Kübel, A. Voigt, R. Schoenmakers, M. Otten, D. Su, T. C. Lee, A. Carlsson, J. Bradley, in *Microsc. Microanal.*, Cambridge University Press, **2005**, pp. 378–400.

[71] P. A. Midgley, M. Weyland, J. M. Thomas, B. F. G. Johnson, *Chem. Commun.* **2001**, *0*, 907–908.

[72] A. J. Koster, U. Ziese, A. J. Verkleij, A. H. Janssen, K. P. De Jong, *J. Phys. Chem. B* **2000**, *104*, 9368–9370.

[73] G. Prieto, J. Zečević, H. Friedrich, K. P. De Jong, P. E. De Jongh, *Nat. Mater.* **2013**, *12*, 34–39.

[74] P. A. Midgley, R. E. Dunin-Borkowski, *Nat. Mater.* **2009**, *8*, 271–280.

[75] J. Zečević, C. J. Gommes, H. Friedrich, P. E. Dejongh, K. P. Dejong, *Angew. Chemie - Int. Ed.* **2012**, *51*, 4213–4217.

[76] C. J. Gommes, H. Friedrich, M. Wolters, P. E. De Jongh, K. P. De Jong, *Chem. Mater.* **2009**, *21*, 1311–1317.

[77] A. TROVARELLI, *Catal. Rev.* **1996**, *38*, 439–520.

[78] A. Trovarelli, J. Llorca, *ACS Catal.* **2017**, *7*, 4716–4735.

[79] I. Florea, D. Ihiawakrim, C. Hirlimann, O. Ersen, **2013**.

[80] T. J. V. Yates, J. M. Thomas, J. J. Fernandez, O. Terasaki, R. Ryoo, P. a. Midgley, *Chem. Phys. Lett.* **2006**, *418*, 540–543.

[81] C. Pham-huu, J. Werckmann, P. Schultz, **2008**, 16800–16806.

[82] C. J. Gommes, *Langmuir* **2012**, *28*, 5101–5115.

[83] C. J. Gommes, H. Friedrich, M. Wolters, P. E. de Jongh, K. P. de Jong, *Chem. Mater.* **2009**, *21*, 1311–1317.

[84] P. Yuan, L. Tan, D. Pan, Y. Guo, L. Zhou, J. Yang, J. Zou, C. Yu, *New J. Chem.* **2011**, *35*, 2456.

[85] F. Gao, Q. Lu, X. Liu, Y. Yan, D. Zhao, *Nano Lett.* **2001**, *1*, 743–748.

[86] V.-T. Hoang, Q. Huang, M. Eić, A. Trong-On Do, S. Kaliaguine, **2005**, DOI 10.1021/LA048349D.

[87] N. Salman, C. H. Rüscher, J.-C. Buhl, W. Lutz, H. Toufar, M. Stöcker, *Microporous Mesoporous Mater.* **2006**, *90*, 339–346.

[88] R. A. Beyerlein, C. Choi-Feng, J. B. Hall, B. J. Huggins, G. J. Ray, *Top. Catal.* **1997**, *4*, 27–42.

[89] S. van Donk, A. Broersma, O. L. . Gijzeman, J. . van Bokhoven, J. . Bitter, K. . de Jong, *J. Catal.* **2001**, *204*, 272–280.

[90] A. H. Janssen, A. J. Koster, K. P. De Jong, *J. Phys. Chem. B* **2002**, *106*, 11905–11909.

[91] D. Z. Y, A. H. Janssen, A. J. Koster, K. P. De Jong, *Angew. Chem. Int. Ed. Engl.* **2001**, *113*, 1136–1138.

[92] X. Pan, X. Bao, *Acc. Chem. Res.* **2011**, *44*, 553–562.

[93] J. P. Tessonnier, O. Ersen, G. Weinberg, C. Pham-Huu, D. S. Su, R. Schlögl, *ACS Nano* **2009**, *3*, 2081–2089.

[94] L. D. Gelb, K. E. Gubbins, R. Radhakrishnan, M. Sliwinska-Bartkowiak, *Reports Prog. Phys.* **2000**, *63*, 727–727.

[95] R. Valiullin, S. Naumov, P. Galvosas, J. Kärger, H.-J. Woo, F. Porcheron, P. A. Monson, *Nature* **2006**, *443*, 965–968.

[96] S. Stapf, *Nat. Phys.* **2006**, *2*, 731–732.

[97] E. Castillejos, P. J. Debouttière, L. Roiban, A. Solhy, V. Martinez, Y. Kihn, O. Ersen, K. Philippot, B. Chaudret, P. Serp, *Angew. Chemie - Int. Ed.* **2009**, *48*, 2529–2533.

[98] J. C. Hernández-Garrido, K. Yoshida, P. L. Gai, E. D. Boyes, C. H. Christensen, P. a. Midgley, *Catal. Today* **2011**, *160*, 165–169.

[99] E. P. W. Ward, T. J. V. Yates, J. J. Fernández, D. E. W. Vaughan, P. a. Midgley, *J. Phys. Chem. C* **2007**, *111*, 11501–11505.

[100] P. Wynblatt, N. A. Gjostein, *Prog. Solid State Chem.* **1975**, *9*, 21–58.

[101] A. Cao, G. Veser, *Nat. Mater.* **2010**, *9*, 75–81.

[102] J. A. Farmer, C. T. Campbell, *Science (80-.).* **2010**, *329*, 933–936.

[103] S. H. Joo, J. Y. Park, C. K. Tsung, Y. Yamada, P. Yang, G. A. Somorjai, *Nat. Mater.* **2009**, *8*, 126–131.

[104] P. M. Arnal, M. Comotti, F. Schüth, *Angew. Chemie - Int. Ed.* **2006**, *45*, 8224–8227.

[105] J. Zečević, K. P. De Jong, P. E. De Jongh, *Curr. Opin. Solid State Mater. Sci.* **2013**, *17*, 115–125.

[106] O. Ersen, I. Florea, C. Hirlimann, C. Pham-Huu, *Mater. Today* **2015**, *18*, 395–408.

[107] P. A. Midgley, M. Weyland, *Ultramicroscopy* **2003**, *96*, 413–431.

[108] R. K. Leary, P. a. Midgley, *MRS Bull.* **2016**, *41*, 531–536.

[109] I. Florea, O. Ersen, R. Arenal, D. Ihiawakrim, C. Messaoudi, K. Chizari, I. Janowska, C. Pham-Huu, *J. Am. Chem. Soc.* **2012**, *134*, 9672–9680.

[110] B. Zhang, D. S. Su, *Comptes Rendus Phys.* **2014**, *15*, 258–268.

[111] R. Leary, P. a. Midgley, J. J. M. Thomas, *Accounts Chem. …* **2012**, *45*, 1782–91.

[112] B. Zhang, D. S. Su, *Small* **2014**, *10*, 222–229.

[113] G. Van Tendeloo, S. Bals, S. Van Aert, J. Verbeeck, D. Van Dyck, *Adv. Mater.* **2012**, *24*, 5655–5675.

[114] "Wikipedia-Transmission electron microscopy," can be found under https://en.wikipedia.org/wiki/Transmission_electron_microscopy#/media/File:Scheme_TEM_en.svg, **n.d.**

[115] D. B. Williams, C. B. Carter, *The Transmission Electron Microscope*, Springer US, Boston, MA, **2009**.

[116] R. F. Egerton, *Electron Energy-Loss Spectroscopy in the Electron Microscope*, Springer, **2011**.

[117] "Conventional TEM," can be found under https://physik.uni-paderborn.de/en/lindner/research/temstem/, **n.d.**

[118] Y. Liao, "Practical Electron Microscopy and Database - An Online Book," can be found under http://www.globalsino.com/EM/, **n.d.**

[119] B. Freitag, S. Kujawa, P. M. Mul, J. Ringnalda, P. C. Tiemeijer, *Ultramicroscopy* **2005**, *102*, 209–214.

[120] C. Kübel, A. Thust, *Nato Sci. Ser. E* **2005**, 373–391.

[121] R. Erni, *Aberration-Corrected Imaging in Transmission Electron Microscopy*, IMPERIAL COLLEGE PRESS, **2010**.

[122] Kai Song, *FEI TECNAI G2 F20 S-TWIN TEM*, **n.d.**

[123] C. T. Koch, *Transmission Electron Microscopy*, **2013**.

[124] W. Zhou, Z. L. Wang, *Scanning Microscopy for Nanotechnology*, Springer, **2007**.

[125] S. J. Pennycook, *Ultramicroscopy* **1989**, *30*, 58–69.

[126] M. H. M. Fawey, In Situ and Ex Situ TEM Studies of Fluoride Ion Batteries, **2017**.

[127] J. I. Goldstein, D. E. Newbury, P. Echlin, D. C. Joy, C. E. Lyman, E. Lifshin, L. Sawyer, J. R. Michael, *Scanning Electron Microscopy and X-Ray Microanalysis : Third Edition*, Springer US, **2003**.

[128] P. J. Goodhew J. Humphreys, and R. Beanland, *Electron Microscopy and Analysis*, Taylor & Francis, **2001**.

[129] A. N. Bright, P. J. Thomas, M. Weyland, D. M. Tricker, C. J. Humphreys, R. Davies, *J. Appl. Phys.* **2001**, *89*, 3143–3150.

[130] R. F. Egerton, *Electron Energy-Loss Spectroscopy in the Electron Microscope*, Springer, **2011**.

[131] J. Radon, in *Berichte Sachs. Akad. Der Wissenschaften*, **1983**, pp. 71–86.

[132] R. Bracewell, *Aust. J. Phys.* **1956**, *9*, 198.

[133] A. J. Koster, U. Ziese, A. J. Verkleij, A. H. Janssen, K. P. De Jong, *J. Phys. Chem. B* **2000**, *104*, 9368–9370.

[134] M. Weyland, Two and Three Dimensional Nanoscale Analysis: New Techniques and Applications, University of Cambridge, **2001**.

[135] M. Weyland, P. A. Midgley, J. M. Thomas, *J. Phys. Chem. B* **2001**, *105*, 7882–7886.

[136] E. P. W. Ward, Three-Dimensional Analysis of Nanoscale Structures Using Electron Tomography, University of Cambridge, **2007**.

[137] M. H. Gass, K. K. K. Koziol, A. H. Windle, P. A. Midgley, *Nano Lett.* **2006**, *6*, 376–379.

[138] S. Bals, V. Radmilovic, Q. Yang, C. Kisielowski, *Microsc. Microanal.* **2004**, *10*, 52–53.

[139] J. S. Barnard, J. Sharp, J. R. Tong, P. A. Midgley, *Philos. Mag.* **2006**, *86*, 4901–4922.

[140] J. S. Barnard, J. Sharp, J. R. Tong, P. A. Midgley, *Science (80-.).* **2006**, *313*, 319.

[141] A. H. Janssen, C. M. Yang, Y. Wang, F. Schüth, A. J. Koster, K. P. de Jong, *J. Phys. Chem. B* **2003**, *107*, 10552–10556.

[142] C. J. Gommes, K. De Jong, J. P. Pirard, S. Blacher, *Langmuir* **2005**, *21*, 12378–12385.

[143] H. Friedrich, J. R. A. Sietsma, P. E. De Jongh, A. J. Verkleij, K. P. De Jong, *J. Am. Chem. Soc.* **2007**, *129*, 10249–10254.

[144] G. Prieto, J. Zečević, H. Friedrich, K. P. de Jong, P. E. de Jongh, *Nat. Mater.* **2013**, *12*, 34–39.

[145] M. Weyland, P. Midgley, in *Transm. Electron Microsc.*, Springer International Publishing, Cham, **2016**, pp. 343–376.

[146] G. N. Ramachandran, A. V Lakshminarayanan, *Proc. Natl. Acad. Sci. U. S. A.* **1971**, *68*, 2236–40.

[147] P. F. C. Gilbert, *Proc. R. Soc. B Biol. Sci.* **1972**, *182*, 89–102.

[148] R. A. Crowther, D. J. DeRosier, A. Klug, *Proc. R. Soc. A Math. Phys. Eng. Sci.* **1970**, *317*, 319–340.

[149] S. R. Deans, *The Radon Transform and Some of Its Applications*, Dover Publications, **2007**.

[150] A. C. Kak, M. Slaney, *Principles of Computerized Tomographic Imaging*, Society For Industrial And Applied Mathematics, **2001**.

[151] M. Radermacher, in *Electron Tomogr. Methods Three-Dimensional Vis. Struct. Cell*, Springer New York, New York, NY, **2006**, pp. 245–273.

[152] P. A. Midgley, M. Weyland, T. J. V Yates, I. Arslan, R. E. Dunin-Borkowski, J. M. Thomas, *J. Microsc.* **2006**, *223*, 185–190.

[153] M. Weyland, Two and Three Dimensional Nanoscale Analysis: New Techniques and Applications, University of Cambridge, **2001**.

[154] M. Radermacher, W. Hoppe, in *7th Eur. Congr. El. Micr.*, **1980**, pp. 132–133.

[155] N. Kawase, M. Kato, H. Nishioka, H. Jinnai, *Ultramicroscopy* **2007**, *107*, 8–15.

[156] R. Gordon, R. Bender, G. T. Herman, *J. Theor. Biol.* **1970**, *29*, 471–481.

[157] P. Gilbert, *J. Theor. Biol.* **1972**, *36*, 105–117.

[158] B. Goris, W. Van den Broek, K. J. Batenburg, H. Heidari Mezerji, S. Bals, *Ultramicroscopy* **2012**, *113*, 120–130.

[159] Z. Saghi, D. J. Holland, R. Leary, A. Falqui, G. Bertoni, A. J. Sederman, L. F. Gladden, P. A. Midgley, *Nano Lett.* **2011**, *11*, 4666–4673.

[160] K. J. Batenburg, S. Bals, J. Sijbers, C. Kübel, P. A. Midgley, J. C. Hernandez, U. Kaiser, E. R. Encina, E. A. Coronado, G. Van Tendeloo, *Ultramicroscopy* **2009**, *109*, 730–740.

[161] E. Biermans, L. Molina, K. J. Batenburg, S. Bals, G. Van Tendeloo, *Nano Lett.* **2010**, *10*, 5014–5019.

[162] S. Bals, K. J. Batenburg, D. Liang, O. Lebedev, G. Van Tendeloo, A. Aerts, J. A. Martens, C. E. A. Kirschhock, *J. Am. Chem. Soc.* **2009**, *131*, 4769–4773.

[163] S. Bals, K. J. Batenburg, J. Verbeeck, J. Sijbers, G. Van Tendeloo, *Nano Lett.* **2007**, *7*, 3669–3674.

[164] E. Castillejos, P.-J. Debouttière, L. Roiban, A. Solhy, V. Martinez, Y. Kihn, O. Ersen, K. Philippot, B. Chaudret, P. Serp, *Angew. Chem. Int. Ed. Engl.* **2009**, *48*, 2529.

[165] R. Leary, Z. Saghi, P. a. Midgley, D. J. Holland, *Ultramicroscopy* **2013**, *131*, 70–91.

[166] B. Goris, W. Van den Broek, K. J. Batenburg, H. Heidari Mezerji, S. Bals, *Ultramicroscopy* **2012**, *113*, 120–130.

[167] M. W. Marcellin, M. J. Gormish, A. Bilgin, M. P. Boliek, *Proc. DCC 2000. Data Compression Conf.* **2000**, 523–541.

[168] J. Frank, *Electron Tomography : Three-Dimensional Imaging with the Transmission Electron Microscope*, Springer US, **1992**.

[169] I. Arslan, J. R. Tong, P. A. Midgley, *Ultramicroscopy* **2006**, *106*, 994–1000.

[170] M. Koguchi, H. Kakibayashi, R. Tsuneta, M. Yamaoka, T. Niino, N. Tanaka, K. Kase, M. Iwaki, *J. Electron Microsc. (Tokyo)*. **2001**, *50*, 235–241.

[171] J. Frank, B. F. McEwen, in *Electron Tomogr.*, Springer US, Boston, MA, **1992**, pp. 205–213.

[172] E. Bladt, Two- and Three-Dimensional Transmission Electron Microscopy of Colloidal Nanoparticles: From Structure to Composition, **2017**.

[173] J. R. Kremer, D. N. Mastronarde, J. R. McIntosh, *J. Struct. Biol.* **1996**, *116*, 71–6.

[174] H.-C. Hege, M. Seebass, D. Stalling, M. Zockler, *ZIB Prepr.* **1997**, *sc-97-05*.

[175] A. S. Frangakis, R. Hegerl, *J. Struct. Biol.* **2002**, *138*, 105–113.

[176] N. Volkmann, *J. Struct. Biol.* **2002**, *138*, 123–129.

[177] C. Bajaj, Z. Yu, M. Auer, *J. Struct. Biol.* **2003**, *144*, 132–143.

[178] C. Fouard, G. Malandain, S. Prohaska, M. Westerhoff, *IEEE Trans. Med. Imaging* **2006**, *25*, 1319–1328.

[179] T. Aste, T. Di Matteo, *Phys. Rev. E* **2008**, *77*, 21309.

[180] K. Hormann, U. Tallarek, *J. Chromatogr. A* **2013**, *1312*, 26–36.

[181] W. Gille, D. Enke, F. Janowski, *J. Porous Mater.* **2002**, *9*, 221–230.

[182] F. Delay, P. Ackerer, C. Danquigny, *Vadose Zo. J.* **2005**, *4*, 360–379.

[183] H. Brenner, *Phil. Trans. R. Soc. Lond. A* **1980**, *297*, 81–133.

[184] A. Taguchi, F. Schüth, *Ordered Mesoporous Materials in Catalysis*, **2005**.

[185] H. Friedrich, P. E. De Jongh, A. J. Verkleij, K. P. De Jong, *Chem. Rev.* **2009**, *109*, 1613–1629.

[186] P. A. Midgley, R. E. Dunin-Borkowski, *Nat. Mater.* **2009**, *8*, 271–280.

[187] C. Kübel, A. Voigt, R. Schoenmakers, M. Otten, D. Su, T. C. Lee, A. Carlsson, J. Bradley, *Microsc. Microanal.* **2005**, *11*, 378–400.

[188] S. Bals, K. J. Batenburg, J. Verbeeck, J. Sijbers, G. Van Tendeloo, *Nano Lett.* **2007**, *7*, 3669–3674.

[189] S. Brunauer, P. H. Emmett, E. Teller, *J. Am. Chem. Soc.* **1938**, *60*, 309–319.

[190] A. Villa, M. Schiavoni, C. E. Chan-Thaw, P. F. Fulvio, R. T. Mayes, S. Dai, K. L. More, G. M. Veith, L. Prati, *ChemSusChem* **2015**, *8*, 2520–2528.

[191] J. R. Kremer, D. N. Mastronarde, J. R. McIntosh, *J. Struct. Biol.* **1996**, *116*, 71–76.

[192] J. Schindelin, I. Arganda-Carreras, E. Frise, V. Kaynig, M. Longair, T. Pietzsch, S. Preibisch, C. Rueden, S. Saalfeld, B. Schmid, et al., *Nat. Methods* **2012**, *9*, 676–682.

[193] F. Luisier, C. Vonesch, T. Blu, M. Unser, *Signal Processing* **2010**, *90*, 415–427.

[194] D. Tschumperlé, R. Deriche, *IEEE Trans. Pattern Anal. Mach. Intell.* **2005**, *27*, 506–517.

[195] K. Zuiderveld, in *Graph. Gems IV*, Academic Press, Massachusetts, **1994**, pp. 474–485.

[196] C. MessaoudiI, T. Boudier, C. O. S. Sorzano, S. Marco, *BMC Bioinformatics* **2007**, *8*, 288.

[197] D. Sage, M. Unser, *IEEE Signal Process. Mag.* **2003**, *20*, 43–52.

[198] G. S. Armatas, C. E. Salmas, M. Louloudi, G. P. Androutsopoulos, P. J. Pomonis, *Langmuir* **2003**, *19*, 3128–3136.

[199] D. M. Ruthven, M. F. M. Post, *Stud. Surf. Sci. Catal.* **2001**, *137*, 525–577.

[200] C. J. Gommes, A. J. Bons, S. Blacher, J. H. Dunsmuir, A. H. Tsou, *AIChE J.* **2009**, *55*, 2000–2012.

[201] S. J. Norton, *J. Opt. Soc. Am. A* **1985**, *2*, 6–13.

[202] C. Kübel, D. Niemeyer, R. Cieslinski, S. Rozeveld, *Mater. Sci. Forum* **2010**, *638–642*, 2517–2522.

[203] K. J. Batenburg, S. Bals, J. Sijbers, C. Kübel, P. a. Midgley, J. C. Hernandez, U. Kaiser, E. R. Encina, E. a. Coronado, G. Van Tendeloo, *Ultramicroscopy* **2009**, *109*, 730–740.

[204] T. W. Ridler, S. Calvard, *IEEE Trans. Syst. Man. Cybern.* **1978**, *8*, 630–632.

[205] W.-H. Tsai, *Comput. Vision, Graph. Image Process.* **1985**, *29*, 377–393.

[206] N. Otsu, *IEEE Trans. Syst. Man. Cybern.* **1979**, *9*, 62–66.

[207] H. R. S. and E. P. S. Z. Wang, A. C. Bovik, *IEEE Trans. Image Process.* **2004**, *13*, 600–612.

[208] S. J. Reich, A. Svidrytski, A. Höltzel, J. Florek, F. Kleitz, W. Wang, C. Kübel, D. Hlushkou, U. Tallarek, *J. Phys. Chem. C* **2018**, *122*, 12350–12361.

[209] K. Yan, G. Wu, T. Lafleur, C. Jarvis, *Renew. Sustain. Energy Rev.* **2014**, *38*, 663–676.

[210] G. W. Huber, S. Iborra, A. Corma, *Chem. Rev.* **2006**, *106*, 4044–4098.

[211] J. P. Lange, E. Van Der Heide, J. Van Buijtenen, R. Price, *ChemSusChem* **2012**, *5*, 150–166.

[212] J. J. Bozell, G. R. Petersen, *Green Chem.* **2010**, *12*, 539.

[213] E. P. W. Ward, T. J. V Yates, J. J. Fernández, D. E. W. Vaughan, P. A. Midgley, *J. Phys. Chem. C* **2007**, *111*, 11501–11505.

[214] P. A. Midgley, J. M. Thomas, L. Laffont, M. Weyland, R. Raja, B. F. G. Johnson, T. Khimyak, *J. Phys. Chem. B* **2004**, *108*, 4590–4592.

[215] A. Villa, D. Wang, G. M. Veith, F. Vindigni, L. Prati, *Catal. Sci. Technol.* **2013**, *3*, 3036.

[216] S. H. Pang, C. A. Schoenbaum, D. K. Schwartz, J. W. Medlin, *ACS Catal.* **2014**, *4*, 3123–3131.

[217] S. H. Pang, C. A. Schoenbaum, D. K. Schwartz, J. W. Medlin, *Nat. Commun.* **2013**, *4*, 2448.

[218] V. Vorotnikov, G. Mpourmpakis, D. G. Vlachos, *ACS Catal.* **2012**, *2*, 2496–2504.

[219] S. M. Rogers, C. R. A. Catlow, C. E. Chan-Thaw, A. Chutia, N. Jian, R. E. Palmer, M. Perdjon, A. Thetford, N. Dimitratos, A. Villa, et al., *ACS Catal.* **2017**, *7*, 2266–2274.

[220] J. Zhang, B. Wang, E. Nikolla, J. W. Medlin, *Angew. Chemie - Int. Ed.* **2017**, *56*, 6594–6598.

[221] P. Wynblatt, N. A. Gjostein, *Prog. Solid State Chem.* **1975**, *9*, 21–58.

[222] R. Liu, Y. Shi, Y. Wan, Y. Meng, F. Zhang, D. Gu, Z. Chen, B. Tu, D. Zhao, *J. Am. Chem. Soc.* **2006**, *128*, 11652–11662.

[223] C. E. Chan-Thaw, A. Villa, L. Prati, A. Thomas, *Chem. - A Eur. J.* **2011**, *17*, 1052–1057.

[224] F. Coloma, a. Sepúlveda-Escribano, J. L. G. Fierro, F. Rodríguez-Reinoso, *Langmuir* **1994**, *10*, 750–755.

[225] P. Serp, J. L. Figueiredo, *Carbon Materials for Catalysis*, **2009**.

[226] X. Liu, K. Zhou, L. Wang, B. Wang, Y. Li, *J. Am. Chem. Soc.* **2009**, *131*, 3140–3141.

[227] G. Jacobs, P. M. Patterson, L. Williams, D. Sparks, B. H. Davis, *Catal. Letters* **2004**, *96*, 97–105.

[228] R. J. Gorte, *AIChE J.* **2010**, *56*, 1126–1135.

[229] A. F. Diwell, R. R. Rajaram, H. A. Shaw, T. J. Truex, *Stud. Surf. Sci. Catal.* **1991**, *71*, 139–152.

[230] Tana, M. Zhang, J. Li, H. Li, Y. Li, W. Shen, *Catal. Today* **2010**, *148*, 179–183.

[231] K. Zhou, X. Wang, X. Sun, Q. Peng, Y. Li, *J. Catal.* **2005**, *229*, 206–212.

[232] D. Zhang, X. Du, L. Shi, R. Gao, *Dalt. Trans.* **2012**, *41*, 14455–14475.

[233] K. Zhou, Y. Li, *Angew. Chemie - Int. Ed.* **2012**, *51*, 602–613.

[234] Z. L. Wang, X. Feng, *J. Phys. Chem. B* **2003**, *107*, 13563–13566.

[235] H. X. Mai, L. D. Sun, Y. W. Zhang, R. Si, W. Feng, H. P. Zhang, H. C. Liu, C. H. Yan, *J. Phys. Chem. B* **2005**, *109*, 24380–24385.

[236] L. S. Zhong, J. S. Hu, A. M. Cao, Q. Liu, W. G. Song, L. J. Wan, *Chem. Mater.* **2007**, *19*, 1648–1655.

[237] H. Li, G. Lu, Q. Dai, Y. Wang, Y. Guo, Y. Guo, *ACS Appl. Mater. Interfaces* **2010**, *2*, 838–846.

[238] W.-Q. Han, L. Wu, Y. Zhu, *J. Am. Chem. Soc.* **2005**, *127*, 12814–12815.

[239] N. Singhania, E. A. Anumol, N. Ravishankar, G. Madras, *Dalt. Trans.* **2013**, *42*, 15343–15354.

[240] S. Agarwal, L. Lefferts, B. L. Mojet, D. A. J. M. Ligthart, E. J. M. Hensen, D. R. G. Mitchell, W. J. Erasmus, B. G. Anderson, E. J. Olivier, J. H. Neethling, et al., *ChemSusChem* **2013**, *6*, 1898–1906.

[241] C. Li, Y. Sun, I. Djerdj, P. Voepel, C. C. Sack, T. Weller, R. Ellinghaus, J. Sann, Y. Guo, B. M. Smarsly, et al., *ACS Catal.* **2017**, *7*, 6453–6463.

[242] Z. Wu, M. Li, S. H. Overbury, *J. Catal.* **2012**, *285*, 61–73.

[243] A. M. Gänzler, M. Casapu, P. Vernoux, S. Loridant, F. J. Cadete Santos Aires, T. Epicier, B. Betz, R. Hoyer, J. D. Grunwaldt, *Angew. Chemie - Int. Ed.* **2017**, *56*, 13078–13082.

[244] N. Takahashi, H. Shinjoh, T. Iijima, T. Suzuki, K. Yamazaki, K. Yokota, H. Suzuki, N. Miyoshi, S. Matsumoto, T. Tanizawa, et al., *Catal. Today* **1996**, *27*, 63–69.

[245] D. B. Williams, C. B. Carter, in *Transm. Electron Microsc.*, Springer US, Boston, MA, **2009**.

[246] I. Florea, C. Feral-Martin, J. Majimel, D. Ihiawakrim, C. Hirlimann, O. Ersen, *Cryst. Growth Des.* **2013**, *13*, 1110–1121.

[247] N. Bugayeva, *MRS Proc.* **2005**, *876*.

[248] G. S. Zafiris, R. J. Gorte, *J. Catal.* **1993**, *143*, 86–91.

[249] A. Trovarelli, *Catal. Rev. - Sci. Eng.* **1996**, *38*, 439–520.

[250] R. Kopelent, J. A. Van Bokhoven, J. Szlachetko, J. Edebeli, C. Paun, M. Nachtegaal, O. V. Safonova, *Angew. Chemie - Int. Ed.* **2015**, *54*, 8728–8731.

[251] E. Aneggi, J. Llorca, M. Boaro, A. Trovarelli, *J. Catal.* **2005**, *234*, 88–95.

[252] A. Gänzler, M. Casapu, F. Maurer, H. Störmer, D. Gerthsen, G. Ferré, P. Vernoux, B. Bornmann, R. Frahm, V. Murzin, et al., *ACS Catal.* **2018**, *8*, 4800–4811.

[253] M. Nolan, S. C. Parker, G. W. Watson, *Surf. Sci.* **2005**, *595*, 223–232.

[254] M. Nolan, J. E. Fearon, G. W. Watson, *Solid State Ionics* **2006**, *177*, 3069–3074.

[255] S. Arrhenius, *Zeitschrift für Phys. Chemie* **1889**, *4*, 96–116.